Universita degli studi di Ferrara

DOTTORTO DI RICERCA

FISICA

CICLO XXIX

Coordinatore Prof. Vincenzo Guidi

Study of internal Jugular vein valve mechanism function: post analysis of M- mode imaging and an experimental model under cardiac monitoring

---

SETTORE SCIENTIFICO DISCIPLINARE FIS/07

DOTTORANDO

Dott. Nadiya Y. Mohammed

TUTORE

Prof. Mauro Gambaccini

Cotutore

Prof. Tamie Poepping

Anni 2017/2018

Contents

Table of Contents

Study of internal jugular vein valve mechanism function: post analysis of M- mode imaging and an experimental model under cardiac monitoring

Abstract:

Background:

Traditionally, the internal jugular vein (IJV) has served as an indicator of right side cardiac function via measurement of central venous pressure and changes in the velocity of jugular venous flow. Since the internal jugular vein valve is the only protective vessel between the brain and heart, recent studies have focused on the dynamic behavior of the valve and its importance in regulating the cerebral blood out flow pathway. It is found that the function of the IJV valve is crucial in maintaining the transcranial blood pressure gradient during cardiopulmonary resuscitation with closed-chest while the morphological incompetence (or absence) of the valve may lead to venous reflux through the IJV. However, nothing is known about the mechanism of the valve opening and closure, as well as the normal opening time. Furthermore, there is insufficient knowledge whether the venous reflux is a normal finding and it is not associated with valve incompetence or valve absence.

Aim of the study:

The project aims to add new indicators of internal Jugular valve function through: 1) post imaging analysis using ultrasound M mode image and 2) an experimental model of mimicking fluid loop to study the modality of flow and pressure wave, upstream and downstream in internal jugular vein with or without valve build up.

Methods:

Normal young subjects underwent an ultrasound scan of the neck in supine position. The internal jugular vein valve was evaluated using B-mode and M-mode images. Two methods have been demonstrated to deduce the normal open time of the valve. The first method based on calculating the area under the curve of valve leaflet separation distance ratio per cardiac cycle. The second method is based on logical tests of three thresholds to examine the valve leaflet separation distance ratio. A hydraulic mimicking fluid loop is created using a programmable pump (Compu Flow 1000, Shelley Medical Imaging/London/Canada). The flow-loop model represents the cerebral out flow pathway through internal Jugular phantoms with and without valve build up. The measurements of flow and pressure were taking at two positions upstream and downstream of the phantom.

Results:

The first method concerning the normal open time reveals a strong positive correlation with second method at the threshold 0.5. The open time of IJV valve constitutes 70% of the cardiac cycle. The experimental model yields a different modality of flow and pressure upstream and downstream of phantoms. A back flow occurs in the beginning of the pulsatile flow wave at a downstream position. The difference in pressure between the two positions increases with the mean flow rate and decreases with higher flow rate in the phantom with no valve while in phantom with valve, the pressure difference has mostly linear proportion with the flow rate.

Conclusions:

The normal open time of the internal jugular vein valve is a new physiologic metric and it gives premise for further studies in the field of neurodegeneration. The experimental finding is adding a new concept to the venous reflux in the internal jugular vein and the necessity of the valve presence in maintain an adequate pressure difference through IJV.

Chapter 1:

Physics and physiologic basic concepts

1.1. Basic physics in Ultrasound imaging:

Ultrasound (US) imaging (sonography) is a diagnostic medical procedure that uses high-frequency sound waves to produce dynamic visual images of organs, tissues or blood flow inside the body. US is not an ionizing radiation, and US imaging does not need the injection of nephrotoxic contrast agents. The core of echo machine is a piezoelectric crystal transducer, when a high frequency signal is applied to the crystal, it vibrates and produces ultrasound wave. If the crystal is in the receiving mode, as it is struck by ultrasound waves, it vibrates. This in turn generates an electrical signal which is analyzed by the echo machine. The axial resolution of an ultrasound image is affected mainly by the wavelength, where a smaller wavelength (and therefore the higher frequency), gives higher resolution, but less penetration. Therefore, higher frequency probes (5 to 10 MHz) provide better resolution but can be applied only for superficial structures and in children. Lower frequency probes (2 to 5 MHz) provide better penetration but lower resolution and can be used to image deeper structures. The propagation velocity of US through a particular medium depends on the compressibility and density of the medium. Usually, the harder tissue, the faster propagation velocity. The average velocity of sound in soft tissues such as the chest wall and heart is 1540 meters/second.

In Fig. 1-1A, it is shown when US beam travelling into a material of two mediums, one of US beam is continue in transmitting and the second one is reflected.

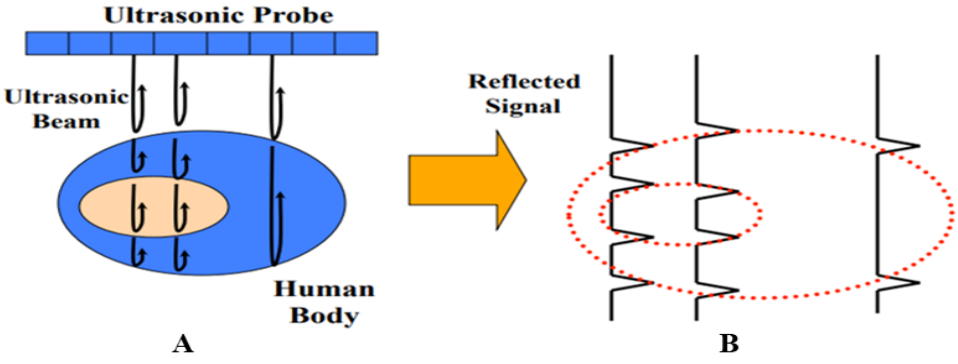

Fig. 1-1: Production of an echo depending on relative acoustic impedances of the two media. A) Ultrasound transducer emits US waves to the tissue inside the body and receives reflected echo from different boundary of two adjacent tissues. B) The amplitude reflected echoes received from different boundaries between tissues G.Saddik, 2015).

The US beam reflection basically occurs at the boundary of two mediums of different property, Fig. 1-1B. This property is known as the acoustic impedance Z of the medium, and it is the product of the density and propagation speed. In the body, the greater difference in acoustic impedance Z between the tissues forming the interface is the greater amount of the energy that is reflected back. The coefficient reflected factor R is the ratio of the intensity of the reflected wave I_r, to the incident wave I_i (BestanJacob, 2012), it is expressed as follows:

$$R = \frac{I_r}{I_i} = \frac{(Z_2 - Z_1)^2}{(Z_2 + Z_1)^2}$$

where Z_1 and Z_2 are the acoustic impedance of two mediums. This is the basis of ultrasound as different organs in the body have different densities and acoustic impedance and this creates different reflectors. Typically, in soft tissues, the amplitude of an echo produced at a boundary is only a small percentage of the incident amplitudes, whereas areas containing bone or air can produce such large echoes that not enough ultrasound remains to image beyond the tissue interface.

1.1.1. Linear pulsed transducer:

This probe has higher frequencies (5–13 MHz), which provides better resolution and less penetration. Therefore, this probe is ideal for imaging superficial structures. In this probe, the piezoelectric crystals are aligned in linear fashion elements within a flat head and each element produces a scan line. Scan line is stepped across the face of the array between each pulse-echo acquisition. Stepping of scan line achieved by:

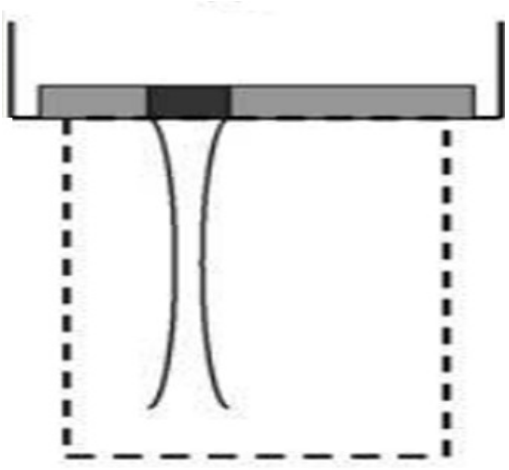

Fig. 1-2: Linear probe, active sub aperture: dark grey, Inactive portion of array: light grey (J.C. Lacefield, 2014).

• deactivating an element at one end of the sub aperture, • activating a new element at the opposite end of the sub aperture (J.C. Lacefield, 2014), Fig. 1-2. The elements combine to produce an US beam emitted perpendicular to the skin body surface producing a rectangular image in shape. An acoustic pulse is emitted from the transducer scattered by the point reflector in the body and received after a time interval which is equal to the round trip travel time, 2d/v, where d is the distance between the reflector and transducer, and v is the ultrasound velocity within the body tissues. After transmission of the short pulse, the transducer operates in receive mode, effectively listening for echoes to return immediately from targets close to the transducer, followed by echoes from greater and greater depths, in a continuous series, to the maximum depth of interest. This is known as the **pulse–echo sequence**. The sending and receiving echoes resulting in short bursts of US waves forms the basis for image acquisition. The **Pulsed US duration time** is the time take for one pulse to occur (in msec.). (Maria Helguera, 2008; Aleksandr Rovner, 2015) . It is expressed as the number of wave cycles in the pulse multiplying by the wave period which equals to:

$$t = \frac{\lambda}{v}$$

$$Pulse\ \ duration\ time = \frac{number\ of cycles\ .\ \lambda}{v}$$

where λ is wave length of US**.** The **Pulse repetition period,** PRP, is the time between the onset of one pulse till the onset of the next pulse. This parameter includes the time when pulse is "on" and the listening or receiving time when the ultrasound transducer is "off". It

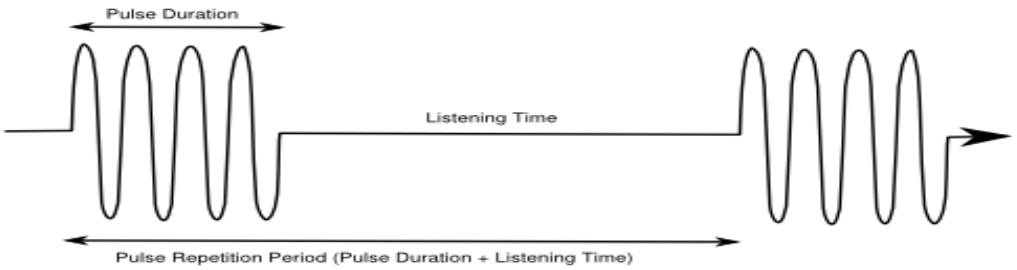

Fig. 1-3: Schematic of sequence between the transmitted pulse duration time and the listening time of echo to the next second, pulse – echo sequence. The listening time must be smaller than the difference between the Pulse repetition period and the length of transmitted pulse (Aleksandr Rovner, 2015).

can be changed by the sonographer by varying the depth to which the signal is send. The typical values of PRP in clinical echo range from 100 microseconds to 1 millisecond, Fig. 1-3.

The **Pulse Repetition Frequency,** PRF, of the transducer is the number of pulses transmit in 1 second, Fig. 1-4 (Narouze, 2011).

The PRF is usually associated with pulse spacing, which is the distance that the pulse travels

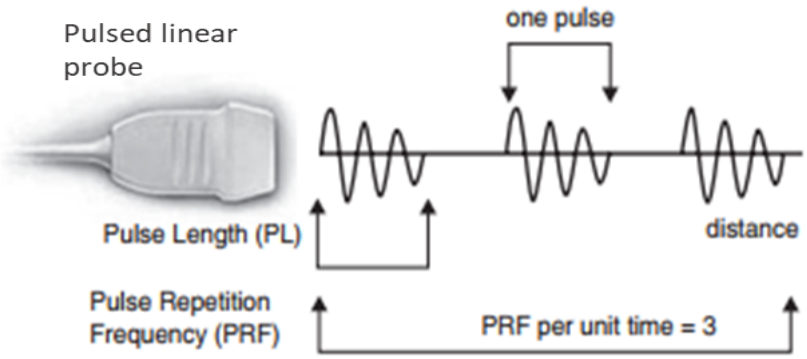

Fig. 1-4: Schematic representation of ultrasound pulse generation (Narouze, 2011).

before the next pulse occurs (Christian Wolff, 2008; G. Saddik, 2015) , as it expressed below:

$$PRF = \frac{1}{PFP}$$

where the PRF is inversely proportion with PFP.

$$P_{space} = \frac{v}{PRF}$$

where pulsed space is inversely proportion with PRF.

1.1.2. Ultrasound A mode imaging:

Wave spikes are presented when a single US beam passes through tissues of different acoustic impendences. The amplitude of the spikes depends on the difference in acoustic impedance between the tissue on each side of each boundary.

If many point reflectors are located in front of the transducer, the total echo can be found

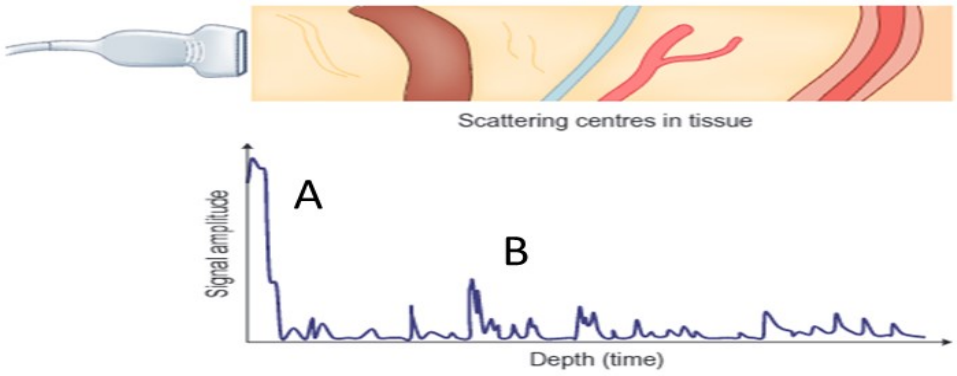

Fig.1-5: A mode ultrasound represented as amplitude of echoes as displayed along the vertical axis and time of rebound (depth) along the horizontal axis (W.McDicken, T. Anderson, 2011).

by simple superposition of each individual echo, in the Fig. 1-5, the distance between these spikes (for example A and B) can be measured accurately by multiplying the speed of sound in tissue by half the sound travel time (Kishore Pichamuthu, 2009).

1.1.3. Ultrasound B mode imaging:

During the first pulse–echo sequence, an image line is formed, such as on the left of the display shown in Fig. 1-6., the active area of the transducer, and hence the beam moves along

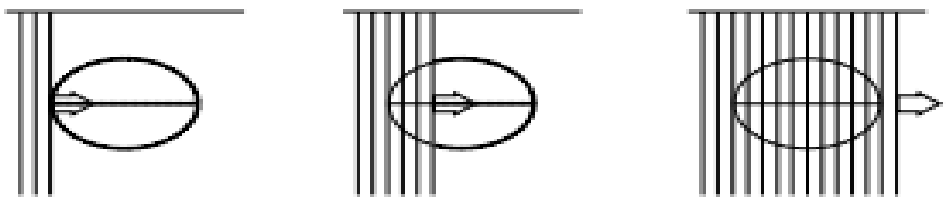

Fig. 1-6: Formation of 2D B-mode image. The image is built up line by line as the beam is stepped along the transducer array (Hoskins, Martin and Thrush, 2010).

the array to the adjacent beam position. For new pulse–echo sequence produces a new image line of echoes with a position on the display corresponding to that of the new beam. The beam is progressively stepped along the array with a new pulse–echo sequence generating a new image line at each position. One complete sweep may take 1/30th of a second, 30 complete images could be formed in 1 sec., allowing real-time display of the B-mode image, Fig. 1-7 (Hoskins, Martin and Thrush, 2010).

1.1.4. Ultrasound M mode imaging:

The further introduction of a time scale in the B mode representation led to develop M-mode (motion mode).

The echo data from a single ultrasound beam passing through moving anatomy on B mode are acquired and displayed as a function of time, represented by reflector depth on the vertical axis (beam path direction) and time on the horizontal axis (Carerj *et al.*, 2003).

M-mode can provide an excellent temporal resolution of motion patterns, data is acquired at a rate up to 1000 frames per second, compared with 15 to 100 frames per second for 2D echocardiography, allowing the evaluation of the heart valves and other cardiac anatomy. M-mode remains a fundamental part of the routine echocardiographic exam and provides an important supplement to the newer echocardiographic modalities (Feigenbaum, 2010), Fig. 1-7.

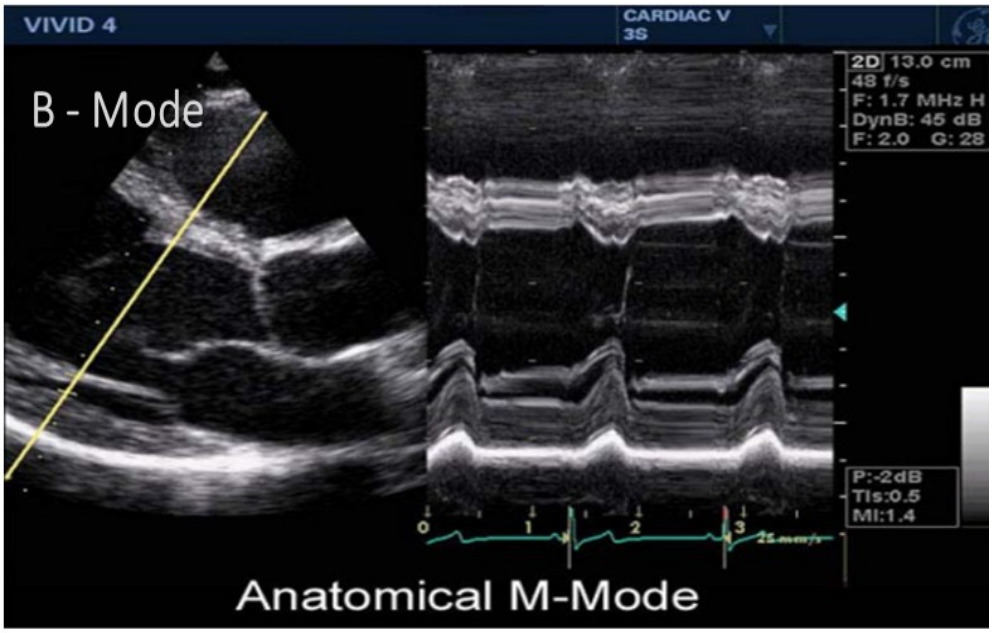

Fig. 1-7: Ultrasound B mode image of left ventricle. The operator chooses a region on B mode to display the structure underlying the cursor line. The reflected echoes under the line displayed in combination with M mode.

1.1.5. Ultrasound Pulsed Doppler mode:

The frequency of US beam changes when it is reflected from the red blood cells that are moving relative to US beam. The reflected beam frequency increases when the red cells are moving towards the transducer of US beam source and decreases when the red cells are moving away from the transducer. The **Doppler shift** is the difference between the transmitted US frequency and reflected beam frequency. This shift is proportional with the velocity aligned to the axis of US beam. In pulse Doppler, a discrete burst of US is emitted. After a specified delay, the Doppler shift is sampled for a brief interval of time. Because the velocity of sound is relatively constant in human body, the Doppler shift location can be determined from the delay between production of the US and its detection. B mode is usually used to specify the location of Doppler interrogation (Mitchell, 1990), as it presents in Fig. 1-8.

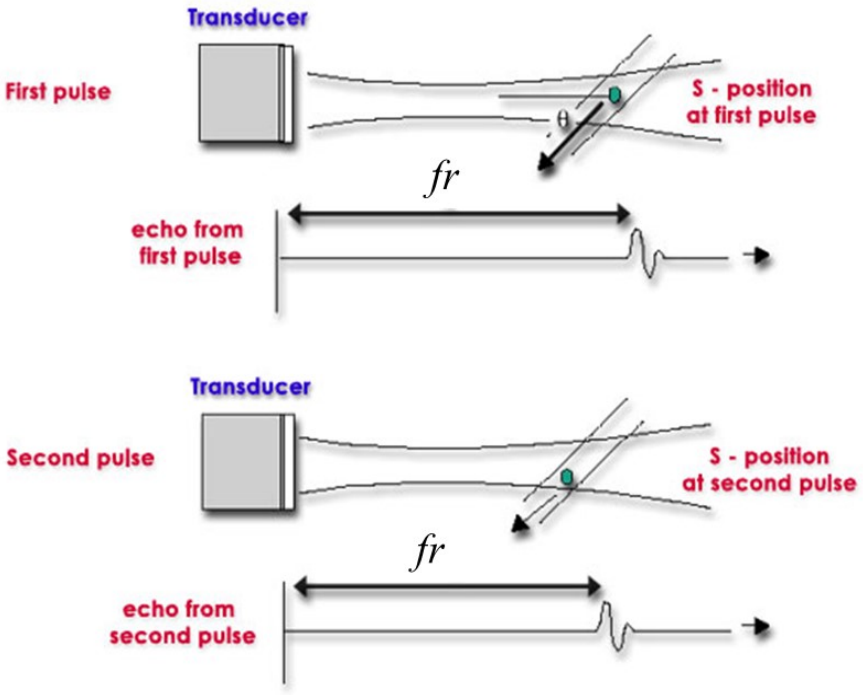

Fig. 1-8: Ultrasound velocity measurement. The diagram shows a scatter center S moving at velocity V with a beam/flow angle θ The velocity can be calculated by the difference in transmit-to receive time from the first pulse to the second *(*t2), as the scattered moves through the beam.

Doppler shift can be expressed in the following equation:

$$f_d = f_r - f_t = \frac{2 f_t v \cos\theta}{c}$$

Where f_d is the Doppler shift between the reflected beam f_r and transmitted beam f_t., the US velocity c, the blood velocity v, the angle between blood flow and beam θ. The Doppler shift frequency increases as the Doppler ultrasound beam becomes more aligned to the flow direction (the angle θ between the beam and the direction of flow becomes smaller, Fig. 1-9. The Doppler shift frequency displayed in Doppler system as a vertical distance from the baseline while the grayscale indicates the amplitude of the detected US with that particular frequency, Fig. 1-10. The Doppler shift frequency can be used to estimate the velocity detected from single location within the blood vessel. The rate or a sample, at which the Doppler shift is determined, is known as the **pulse repetition frequency** or PRF. It depends on the velocity of sound and on the depth of tissue being interrogated. The deeper the tissue being examined, the longer the transducer has to wait for echoes to come back, hence a lower PRF. The sample Doppler shift should be at least twice as frequently as the highest frequency shift that wants to measure, ($PRF=2 \Delta F_{shift}$), according to that the PRF in relation to detected velocity is expressed as follows (Colin Deane, Kypros Nicolaides, Giuseppe Rizzo, 2002; Mark Hammer, 2014):

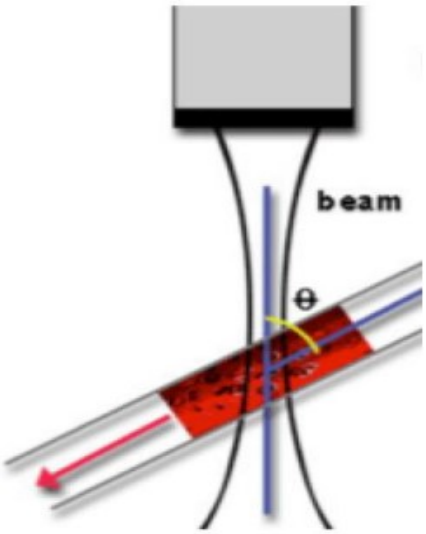

Fig. 1-9: The insonation angle between ultrasound orientation and blood flow can be changed as a result of variation in probe or vessel.

$$V_{max} = \frac{PRF}{4cf_t}$$

Where c is US velocity and f_t the transmitted US beam, the maximum velocity V_{max}

1.1.6. Ultrasound Colored Doppler mode:

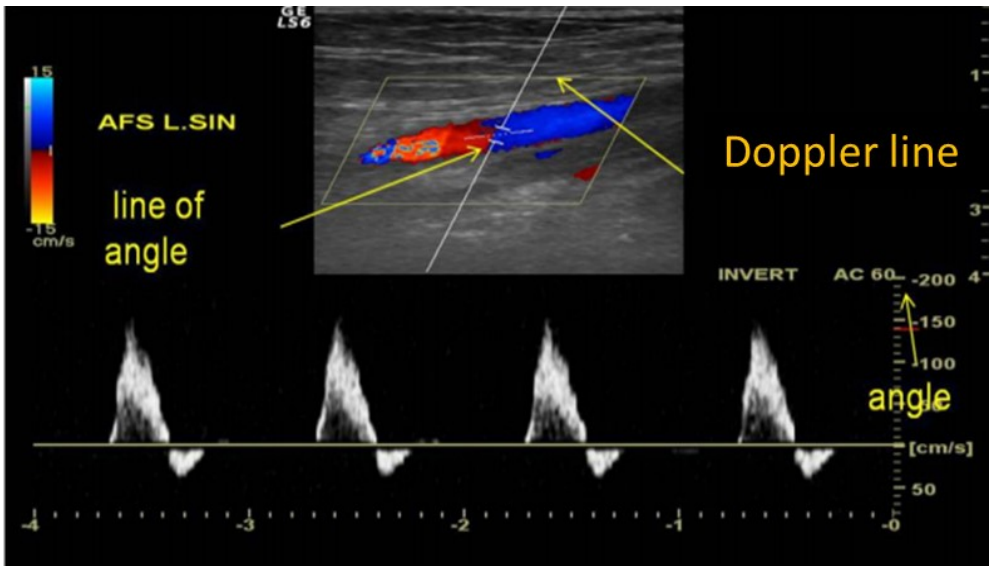

Fig. 1-10: Doppler blood velocity within a sample volume in blood vessel, the orientation of line angle is parallel to blood flow.

Color flow imaging tells us about intra-cardiac blood flows in relation to the anatomy(Kishore Pichamuthu, 2009). The echo signals received along a series of locations in an ultrasound beam width by applied transmit-receive pulse signals are called pulse packets. With most instruments, ten or more pulse packets are used to produce an estimate of mean velocity of all reflectors along multiple beam lines in the beam width. This data is assigned color by the machine and is superimposed on B mode data from stationary structures within the beam width.

In the image, Fig. 1-10, the column bar serves as a legend which shows the velocity and direction of blood flow. The red color indicated flow toward the transducer and blue color indicated flow away from the transducer. If handled properly, when the transducer is aimed at an artery, the color should be red and if it is aimed at a vein, the color should therefore be blue. (Moorthy, 2002; Boote, 2003).

1.2. Electromagnetic flowmeter probe:

Electromagnetic flow measurement is based on Faraday's Law of Induction. The law states that; a voltage is induced across a conductor moving through a magnetic field.

The electromagnetic flowmeter EMF probe consists of a non-ferromagnetic measuring tube with an electrically insulating inner surface. A magnetic coil is located diametrically on the measuring tube, while a pair of electrodes placed at right angles to the direction of magnetic field, in contact with the process liquid through the tube wall. The coils through which current flows generates a magnetic field with induction B perpendicular to the longitudinal axis of the tube, Fig. 1-11.

This magnetic field penetrates the measuring tube and the process liquid flowing through it, which must be electrically conductive. In accordance with Faraday's Law of Induction, a voltage Ui is induced in the process liquid that is proportional to: the flow liquid velocity v, induction magnetic field B and the internal diameter D of the tube. In simplified form, the following expression is applicable (Hofmann, 2003):

$$U_i = K.B.D.v$$

Where K is inductance constant. This signal voltage Ui is picked up by electrodes that are in conductive contact with the process liquid and insulated from the tube wall. By using the following formula:

$$Q = A.v = \frac{\pi D^2 v}{4}$$

where Q is the flow volume, A is the cross section area of the EMF tube, the signal voltage Ui is converted by a signal converter into a flow Q (Hofmann, 2011), as it expressed below:

$$Q = U_i . \frac{\pi D}{4.K.B_i}$$

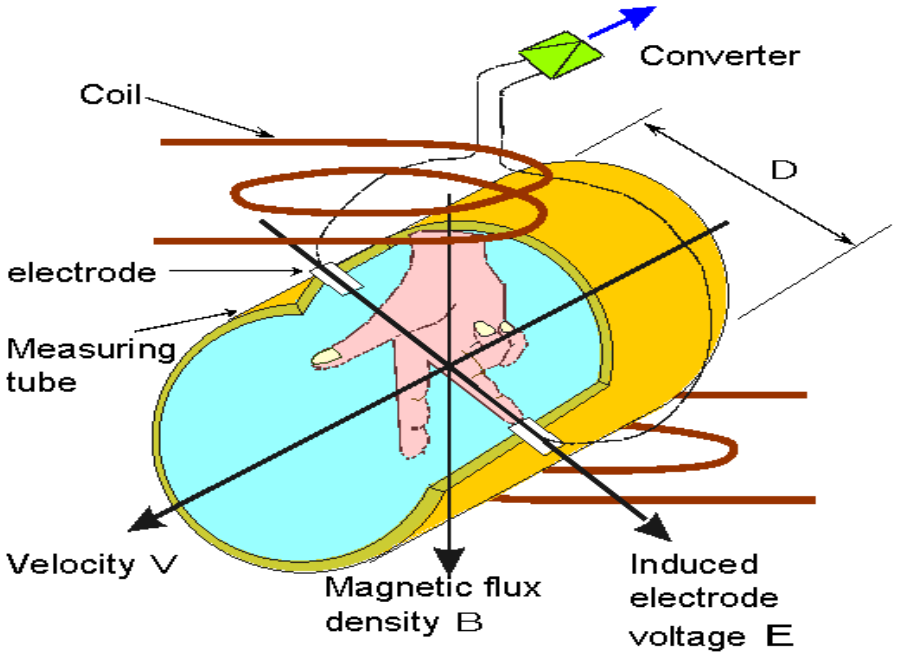

Fig.1-11: Faraday law principle applied on electromagnetic flow measurement. The generated voltage U is proportion perpendicularly to magnetic flux B, and flow velocity.

1.3. Electric digital pressure probe.

For electronic pressure measurement a sensor is required to detect the pressure and/or its change, and to convert it accurately and repeatedly into an electrical signal utilizing a **resistive pressure principle** which is based on measuring the change in electric conductor resistance R, caused by a pressure-dependent deflection. It can be expressed as follows:

$$R = \rho \frac{l}{A}$$

Where ρ is the resistivity, R is the electric resistance, l is the length and A is the cross section area. If a tensile force is applied to the conductor, its length increases and its cross-sectional area decreases.

The resistive pressure measurement based on using a main body exhibiting a controlled deflection under pressure. This main body frequently has a thin area representing as a weak diaphragm. The degree of deflection caused by the pressure is measured using metallic strain gauge, sensor whose resistance varies with applied force and converts force, pressure, tension, weight, etc., into a change in electrical resistance. The strain gauges located on the diaphragm. Some of them are located on elongated and others on compressed areas of the diaphragm. If the diaphragm deflects under the action of a pressure, the strain gauges are deflected correspondingly (Fig. 1-12). The electrical resistance increases or decreases proportionally to the deflection (elongation or compression). To accurately measure the resistance change, the strain gauges are wired to a Wheatstone measuring bridge (John, 2011).

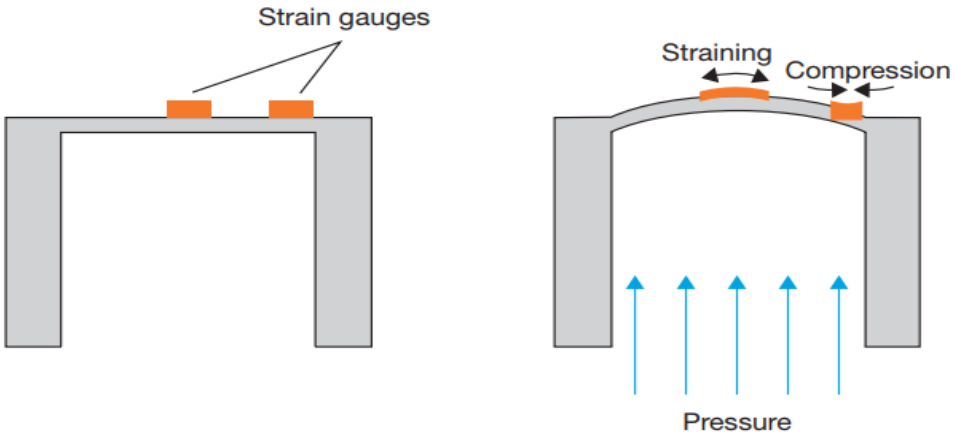

Fig. 1-12: Deflection of the sensor diaphragm under pressure applied.

1.4. Cardiovascular physiological concepts

1.4.1. Cardiac output:

The cardiac output (CO) is the stork blood volume ejected from heart in beats per minute, it constitutes of two circulations, pulmonary and systemic that link in series between left ventricle (LV) and right ventricle (RV). The CO should be equivalent to the change in venous return (VR), the blood flowing from periphery back to the right atrium, this normal physiological condition can be adjusted by Frank – Starling mechanism of the heart which states that the ventricle contraction increases in respond to increased venous return. Hence, increased preload of myocardial muscle, as a result to myocardial cells elasticity (Kemp and Conte, 2012; Oyama, 2015).

In which, the preload is the end diastolic pressure that stretches the walls of ventricles to their greatest dimensions. In prior to chamber contraction, the much stretch in myocardial cell length, in a physiologic boundary, has much force of their contraction (Moss and Fitzsimons, 2002).

1.4.2. Venous return and Central venous pressure:

VR controls the end diastolic volume of ventricle, stroke volume and thus controls CO. VR is proportional to the pressure difference between right atrium pressure P_{RA} and venous pressure P_V, the driving force to filling the heart, divided by venous systemic resistance R_V as in Fig.1-13. The pressure gradient driving blood back to the heart is lower than 10 mmHg, this lead to alter VR in respond to a small percentage change in either P_{RA} or P_V.

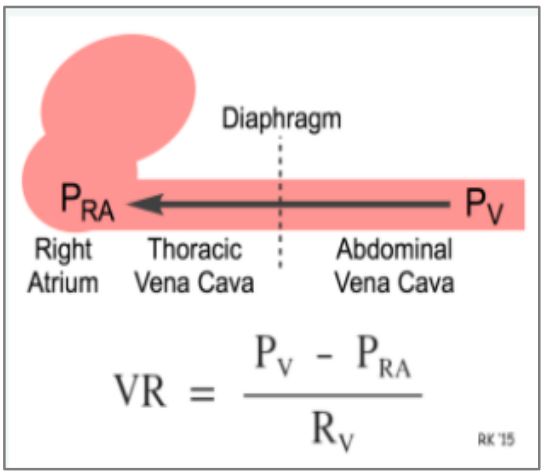

Fig.1-13: Venous return VR proportional to the difference between venous pressure P_V and right atrial pressure P_{RA} divided by venous resistance R_V.

The filling pressure of the right heart is called the central venous pressure CVP. It represents the pressure in thoracic vena cava in close to RA.

Thus, the CVP is considered the same in both vena cava and RA. In normal circumstances the CVP is ranged from 2-6 mmHg. Hence, CVP determines both filling pressure and preload of the right ventricle, which regulates stroke volume through Frank starling mechanism.

The change of blood volume in thoracic vena cava divided by the vein compliance is equal to CVP (Aayeesha Ali, 2012; Richard E. Klabunde, 2013).

VR and CVP are both affected by several factors (Richard E. Klabunde, 2012; Jeff McLaughlin, 2016):

1. Decreased venous compliance, leading to increase central venous pressure and promotes venous return by increasing cardiac output through the Frank-Starling mechanism .
2. Blood Volume: Increased blood volume increased CVP.

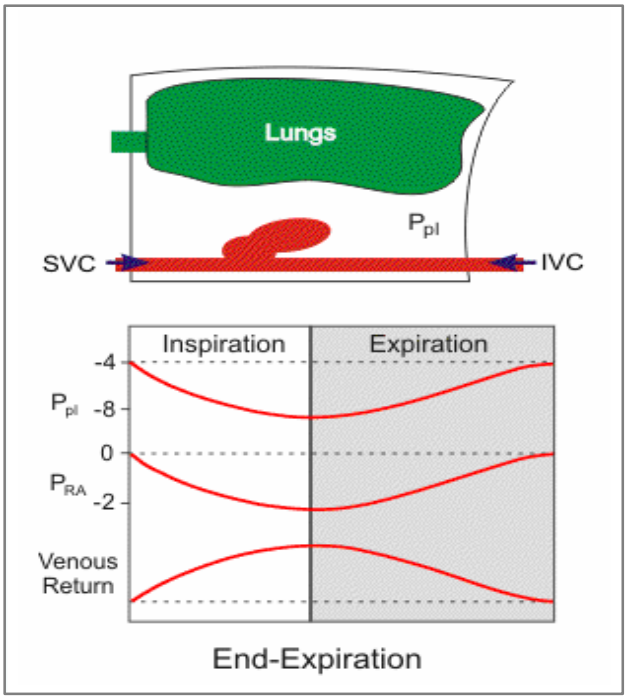

Fig. 1-14: The inspiration and expiration effect on right atrial pressure P_{RA} and intrapleural pressure P_{PL} and the impact on venous return.

3. Respiratory function: The intra pleural pressure P_{PL} is the pressure in the space between the chest wall and thorax organs (heart, vena cava vein, lung) and is highly effects on P_{RA} and vena cava pressure. While the transmural pressure P_L is the difference between intra cardiac or intravascular pressures and P_{PL} pressure. During inspiration, the chest wall expands and the diaphragm descends downward leading P_{PL} to become much negative. Meanwhile, P_{RA} and vena cava pressures falls down and increase the P_L that makes the thorax organs expand and promote the cardiac preload. Hence, the drop P_{RA} pressure results increase in the venous return to RA and increase filling pressure during inspiration while the opposite will occur during expiration, the mechanism is represented in Fig. 1-14.

4. Skeletal Muscle Pump: During walking, the muscle exerts pressure on veins provided with numerous one pathway valves. The venous valves open, superior to muscle construction, to pass the blood flow upward, then leading to increase venous return.
5. Gravitational effects are essential during postural change from sitting to standing through the effecting on CVP (Holmlund *et al.*, 2017) an hence effects on venous return. In the human body, gravity pulls the blood towards the feet. Luckily, the veins in the legs and arms have valves structures that help to pump the blood back up as the nearby muscles contract and relax (Frank Padberg, Carman, 2016).

1.4.3. Vascular compliance:

Vascular compliance C is the ability of the vessel to distend and expand its volume V related to the transmural pressure P_L affecting in that volume. As the veins are much thinner wall than the arteries, they have higher compliance than the arteries and therefor the veins accommodate much blood volume with small change in pressure. Subsequently, the greater compliance of veins is larger result in vein collapse, that occurs at pressures less than 10 mmHg. Physically, compliance (C) is defined as the change in volume (ΔV) divided by the change in transmural pressure (ΔP_L).

1. $$C = \frac{\Delta V}{\Delta P_L}$$

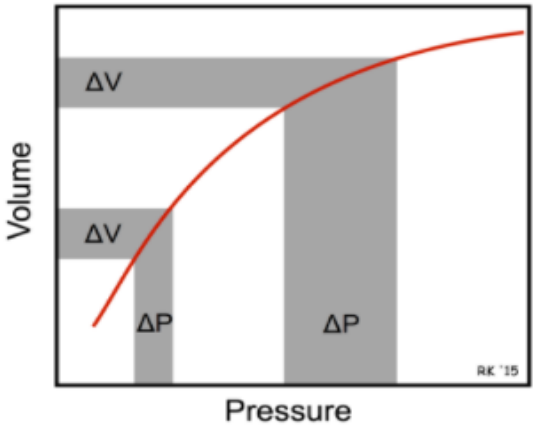

Fig.1-15: Non-linearity relationship between volume and pressure is in biological tissues.

Where *C* is the compliance in ml/mmHg. A curve plot of the relation between change in volume and related PL can be generated. The slope of the curve ($\frac{\Delta V}{\Delta P_L}$) at any given point reflects the compliance of the vessel at that given pressure and volume. Fig. 1-15, shows the compliance is decreases at higher volumes and pressures, a larger change in pressure for a given change in volume.

1.4.4. Vascular Tone

The compliance relationship curve could be shifted downward by the vascular smooth muscle contraction effect in respond to increase pressure, which increases vascular tone and reduces vascular compliance. The opposite effect occurred with the smooth muscle relaxation in respond to reduced pressure, which increases compliance and shifts the compliance curve upward. This adaptive is necessary particularly in the venous vasculature for the regulation of venous pressure and cardiac preload, but it trends relatively lower in cerebral and renal circulations (low vascular tone) (Cipolla, 2009).

1.4.5 Viscoelasticity

Elasticity is the property of solid materials to return to their original shape and size after the forces deforming them have been removed. Which is the applicable of Hooke's law for spring, a simple object that's essentially one-dimensional (Giuliodori *et al.*, 2009).

2. $$F = -K\Delta L$$

Where F is force to cause spring extension (change in length ΔL), K is a proportional constant, Hook' law can be generalized to strain and stress, Fig. 1-16.

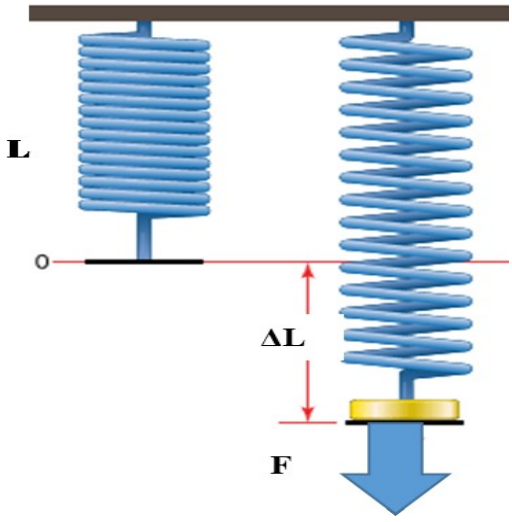

Fig. 1-16: Application of Hook's law; an applied force F equals to constant K times the change or extension in length

In physics, stress is the internal distribution of forces within a body that balance and react to the external loads applied to it, it indicates the force per unit area A (Pa or N/cm^2). Strain is defined as the mechanical deformation of a physical body, change in length over original length. An equation analogous to Hooke's law describes the relationship between stress and strain:

3. $$\frac{F}{A} = \mathrm{Y}\frac{\Delta L}{L}$$

4. $$\sigma = Y \frac{\Delta L}{L}$$

Where σ is the stress, and it is equal to Young elastic modulus, Y, multiplying by strain. The unit of Y is Dyne/cm^2.

If blood vessel filled with a known blood volume with its corresponding pressure increases filling pressure (increasing stress **σ**) and then increases in volume (increasing strain).

However, the pressure drops down over time even at a constant strain. The dropping pressure over time is termed stress pressure. This phenomenon can be explained by Laplace law.

1.4.6. Laplace Law:

The larger vessel radius, the larger wall tension T required to withstand a given internal blood filling pressure, T is proportional to P and radius r (Tα P r), Fig. 1-17, the derived Laplace law for thin wall vein is expressed as:

5. $$T = \sigma h = r_0 \Delta P$$

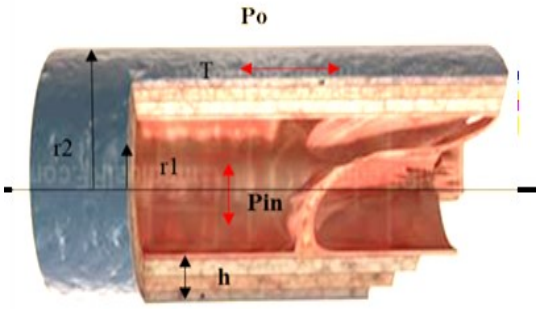

Fig. 1-17: Laplace law applicable on thin vein wall with the internal and external radiuses r1 and r2, thickness wall h and pressure in Pin and pressure out Po.

Where ΔP is the transmural pressure of difference between pressure in P_{in} and pressure out P_o. While r_1 and r_2 is the internal and external diameters of the vein. The thickness h is more less as compared to r, ($h << r_1 = r_2 = r_0$). Equation (5) is an expression of Laplace's law for a thin walled vessel. Note that for a given transmural pressure, the wall tension (T = σh) per unit length, increases as the radius increases and vice versa. According to equation 5, pressure can be declined when the T declines over time even with a constant volume (r constant). This depression in pressure indicates a stress relaxation (Roger and Mark, 2004).

1.5. Cerebral venous out flow and neck veins drainage:

There are three Jugular veins at each side of the neck, external jugular vein (EJV), anterior jugular vein (AJV) and internal jugular vein (IJV) that drain blood from brain, face, and neck into the heart passing from vena cava. However, the main cerebral venous outflow tract in the neck consists of the internal jugular vein (IJV), vertebral venous system, and the deep cervical veins (cervical soft tissue veins). These three venous pathways show multiple anastomoses between them in the neck, especially in the region of the cranial cervical junction. Among them, IJV and the vertebral vein can be detected easily by color Duplex ultrasound (Doepp *et al.*, 2004; Ciuti *et al.*, 2013).

1.5.1. Internal jugular vein morphology:

Internal jugular vein being the principle vein supplying to the head and neck area (Hollinshead, 1982; Deepak, Sarvadnya and Sabitha, 2015).

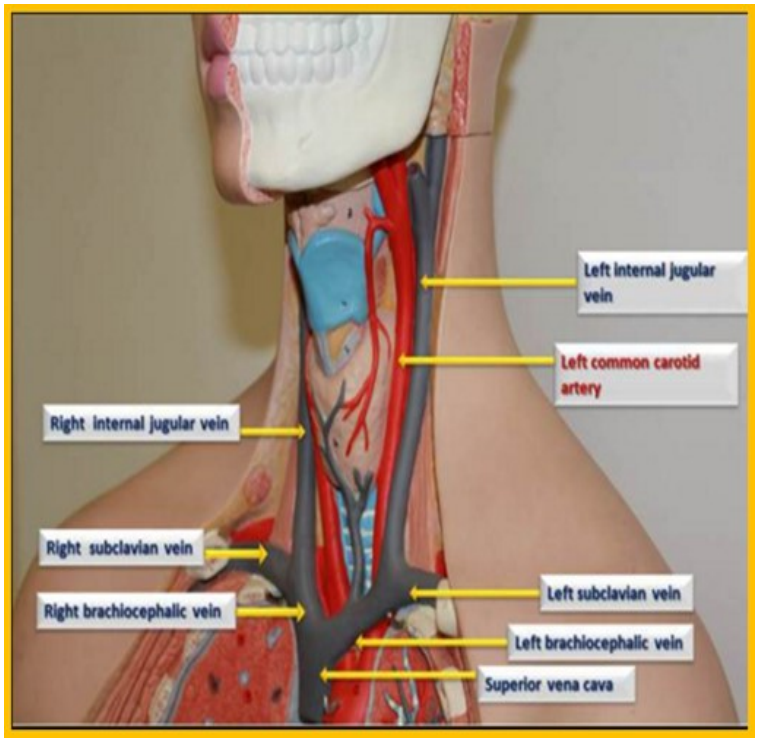

Fig.1-18: Anatomy of neck vessels including right and left jugular veins with their termination at brachiocephalic vein and vena cava.

The cerebral venous flow goes mainly from the superficial and deep venous system to the transverse sinus which in its turn continues in the sigmoid sinus to drain at the level of IJV foramen, the initial start of IJV. The IJV is asymmetric with two slight bulbs at the terminations, the inferior bulb and superior bulb. It leaves the skull at jugular foramen to descend down the neck, beings at one end lateral to the interior carotid artery and then lateral to the common carotid artery(Gray, 2015). At the base of the neck it joins the subclavian vein to form the brachiocephalic vein, Fig.1-18.

The confluence of the two brachiocephalic veins gives rise to the superior vena cava, which

drains the cerebral venous blood into the right atrium.(Oliver Jones, 2017).

1.5.2. JVP pulse wave:

The jugular vein pulse (JVP) is the oscillating top of the vertical blood column in the distended proximal portion of IJV that reflects phasic pressure changes in right atrium and right ventricle (during systole) (Ankur Gupta, 2015). The right IJV is preferred to the left one in evaluating the JVP because firstly, the right IJV has a straight course line from superior vena cava to right atrium and secondly, it is less likely to compress from surrounding structures.

Unlike the left IJV, it drains into innominate vein which is not in straight line from vena cava and right atrium and also it might be compressed by dilated aorta or aneurysm. The normal mean jugular venous pressure is 6 to 8 cm H_2O which is determined as the vertical distance above the midpoint of the right atrium. The normal jugular venous pulse wave consists of three positive waves, a, c, and v, and two negative waves, x and y (Reems , Dvm , Dacvecc, 2012). The (a) wave is caused by right atrial systole, when the pressure transmitted back to

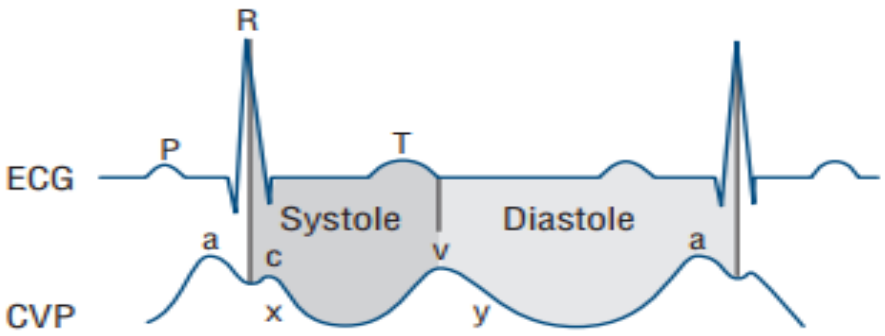

Fig. 1-19: Normal JVP waveform corresponding to electrocardiography tracing ECG.

the jugular veins by the contraction of the right atrium followed by (x) descent which results from right atrial relaxation during atrial diastole and right ventricle systole, (c) wave occurs in (x) descent due to the carotid artefact and Tricuspid valve pushing back caused by ventricular contraction. The (v) wave reflects the passive filling of right atrium on time with tricuspid valve closing. It starts late in right ventricular systolic and ends at early diastole (Applefeld, 1990; Garg and Garg, 2000), Fig. 1-19.

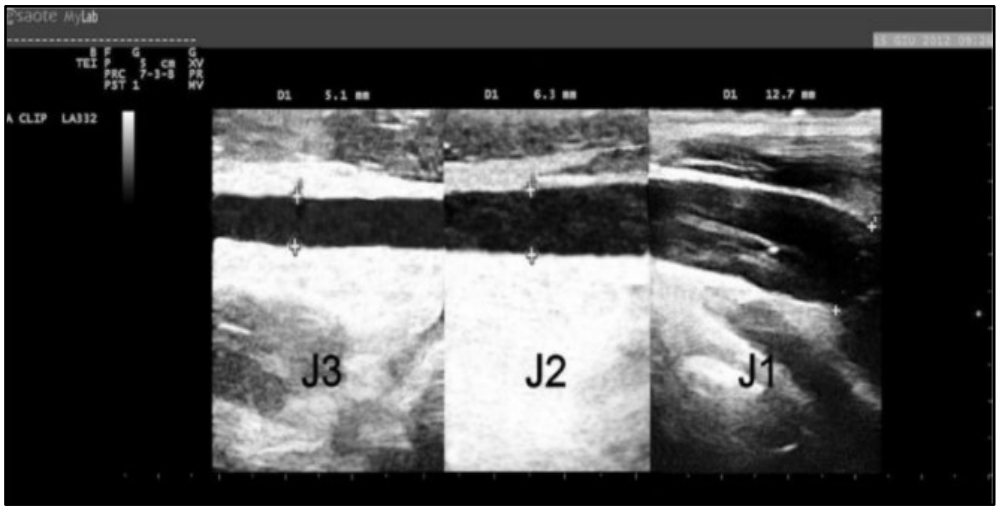

Fig. 1-20: Normal IJV, long axis view showing progressive reduction of vessel diameter proceeding from J_1 point (12.7 mm) passing through J_2 (6.3 mm) to J_3 (5.1 mm). (6.3 mm).

1.5.3. Ultrasound evaluation of IJV:

The internal jugular veins (IJVs), together with the vertebral veins constitute the predominant extra cranial pathways for the cerebral venous drainage (Zamboni *et al.*, 2011). IJV is moderately superficial, thus high frequency ultrasound linear probe is appropriate to obtain an anatomical image. B-mode can display the IJV as a short axis view, a perpendicular visualization of the vein, showing the IJV and carotid artery as rounded structures. The alternately, long axis view cannot show carotid artery (Craig Sisson, MD and Arun Nagdev, 2007; Mahan, McEvoy and Gravenstein, 2016). Since, the IJV size and course are highly variable, nevertheless it is easily compressible due to its thin wall and low blood pressure (Tain, Ertl-Wagner and Alperin, 2009; Miki *et al.*, 2014). Therefore, cross-sectional area (CSA) varies with subject posture position, head rotation, breathing, and cardiac function. Consequently the color Doppler ultrasonography generally used for IJV screening, it is an operator dependent and limited in its field of view (Zavoreo *et al.*, 2013; Laganà *et al.*, 2016). A normal jugular vein gradually reduces its longitudinal diameter, as described in anatomy text, it is possible to segment IJV into three different segments J_3 to J_1, as it proposed in ultrasound US studies and CT scan (Lorchirachoonkul *et al.*, 2012), Fig. 1-20.

1.5.4. Doppler blood velocity of IJV:

The ultrasound examination began with transverse scans to identify the jugular veins and carotid arteries. Subsequently, the IJVs were scanned in the longitudinal view to assess the magnitude and morphology of intraluminal echoes. The IJV Doppler spectrum include the following waves: *s*: systolic wave, determined by the negative intra-atrial pressure with the movement of the atrioventricular septum toward the cardiac apex, *v*: is the result of the intra-atrial positive pressure created by over distension of the right atrium during the filling phase.

d: diastolic wave determined by the negative intra-atrial pressure, consequence of the opening of the tricuspid valve, a: reflects the intra-atrial positive pressure during the atrial contraction (Gramiak, St Louis and Mosby, 1978; Malferrari, Prati and Zedde, 2014), Fig.1-21.

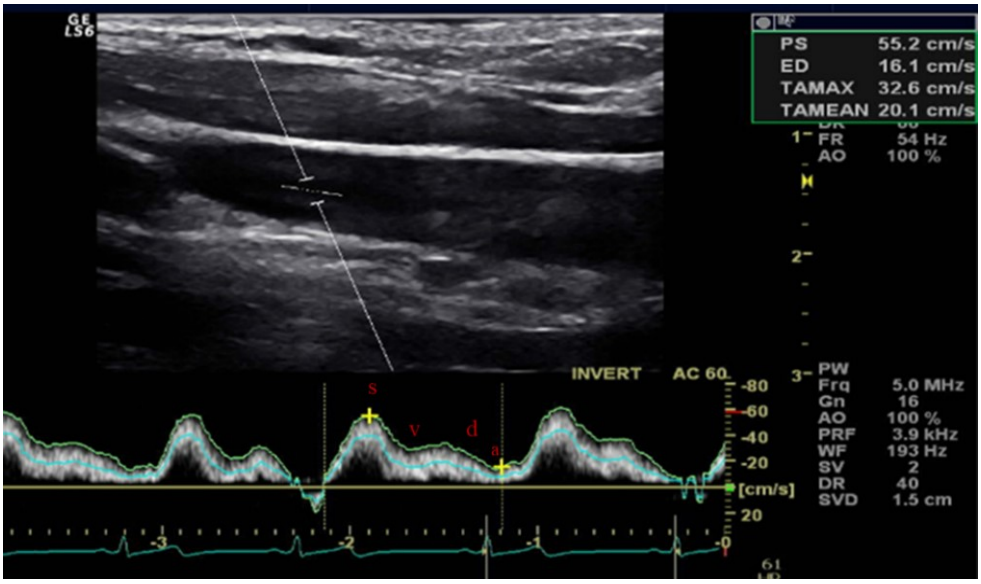

Fig.1-21: Doppler spectrum waves of IJV in J3. Systolic s, mid diastole depressed v, late diastole waves d and end diastolic slowing a.

1.5.5. Internal Jugular vein valve morphology:

The valve cusps are macroscopically described in anatomical studies as thin translucent structures; the majority of valves are composed of two cusps (66–90 %). Mono cusp valves are the second most common form, while tricuspid valves account for 6–7 %. The valves are located on the distal portion of the IJV (J1, in the ultrasound) 0.5 cm above the union of the subclavian and internal jugular veins at the lower limit of the jugular bulb as it presents in

Fig. 1-22. Using ultrasound imaging, the IJV valve were found in one IJV in about 90% of the cases, more frequently on the right side, Fig. 1-23, (Brownlow and cKinney,1985; Harmon and Edwards, 1987; D. Lepori1 *et al.*, 1999; Malferrari, Prati and Zedde, 2014).

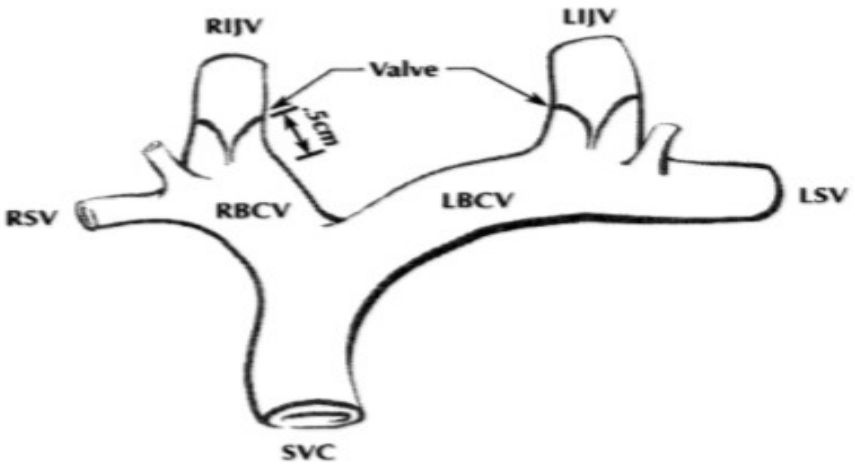

Fig. 1-22: Anatomical diagram of internal jugular valves. RIJV, right internal jugular vein; LIJV, left internal jugular vein; RSV, right subclavian vein; LSV, left subclavian vein; SVC superior vena cava; RBCV, right brachiocephalic vein; LBCV, left brachial-cephalic vein.

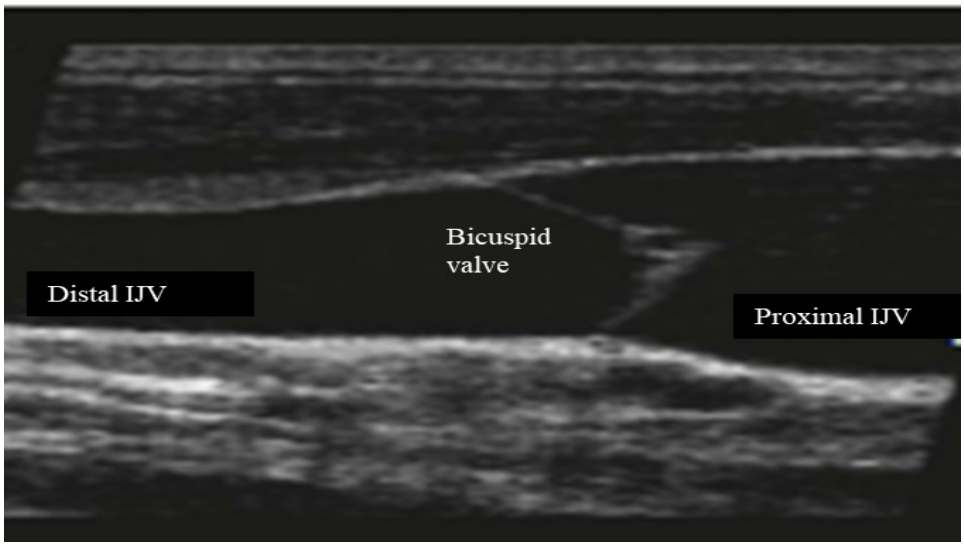

Fig. 1-23: Longitudinal Ultrasound view of internal jugular vein, (IJV) valve is located about 0.5 cm above the union of the subclavian vein and the IJV at the lower limit of the jugular bulb.

1.6. Windkessel Model mechanism:

Windkessel model mechanism is widely used to operationalize vascular characteristics (Kokalari, Karaja and Guerrisi, 2013). It describes the heart and systemic arterial system as a hydraulic closed circuit. In this analogy the circuit contained a water pump connected to a chamber, filled with water except for a pocket of air. As it's pumped, the water compresses the air, which in turn pushes the water out of the chamber. This analogy resembles the

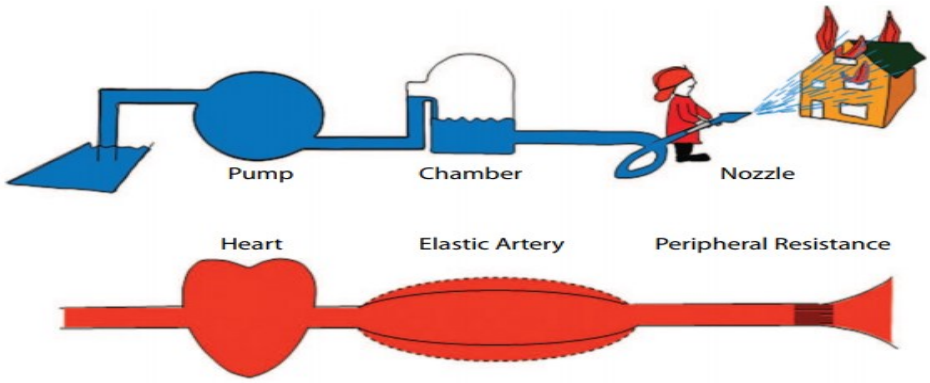

Fig. 1-24: The concept of Windkessel mechanism. The air reservoir (chamber) is the actual Windkessel, and the large arteries act as the Windkessel. The combination of compliance, together with aortic valves and peripheral resistance, results in a rather constant peripheral flow, the figure adapted from (Westerhof, 2009).

mechanics of the heart, Fig. 1-24. The Windkessel Model is analogous to the Poiseuille's Law for a hydraulic system. It describes the flow of blood through the arteries as the flow of fluid through pipes (Westerhof, Lankhaar and Westerhof, 2009). Thus, the mechanism based on mass conservation as in systole, the vessels extend due to the rise in blood pressure, increasing the blood volume stored in the vessels Q_{store}. While in diastole, the blood pressure drops and the vessels contract again, releasing the stored blood volume Q_{out}.

6. $$Q_{in} = Q_{store} + Q_{out}$$

where Q_{in} is the flow in artery equals to stored flow and output flow. Since the compliance indicates the change in volume store V per change in input pressure P_{in}, Q_{store}, it can be expressed as follows:

7. $$Q_{store} = \frac{dV}{dt} = C\frac{dP_{in}}{dt}$$

The blood flowing from wider arteries into smaller arterioles encounters a certain resistance. In laminar flow, it could be accurate to consider a linear relation between the pressure difference P_{in} and flow Q_{out}. The proportional constant refers to the resistance R.

8. $$R = \frac{P_{in}}{Q_{out}}$$

By substituting equations 8 and 9, the Qin (Quick, Berger and Noordergraaf, 1998) will be equal to:

9. $$Q_{in} = C\frac{dP_{in}}{dt} + \frac{P_{in}}{R}$$

In the electrical analog, the compliance C, (cm^3/mmHg), of the vessels can be modeled with a capacitor of electric charge storage properties and peripheral resistance of the systemic arterial system R, mmHg. sec/cm^3, representing as an energy dissipating resistor.

When a potential difference is applied to the two plates of capacitor C_e, electrical charges of equal magnitude but opposite polarity build up on each plate yielding an electrical field to develop in between. Hence, a potential difference develops across the plates. This potential difference V is directly proportional to the amount of separated charge q, $q = C_e V$.

Since the current I through the capacitor C_e is the rate at which the charge q is forced onto the capacitor (Creigen, V., Ferracina, L. and Hlod A., 2007), it can mathematically express as:

10. $$I = C_e\frac{dV}{dt}$$

Thus, 2- element Windkessel model can be identified by electrical circuit with a capacitor *C* corresponding to the arterial compliance and a resistor R corresponding to the resistance to blood as it passes from the artery to the narrower arterioles, Fig 1-25.

The second type is 3-element Windkessel model, Fig. 1-25, implemented by adding a resistance to 2- element Windkessel as a proximal resistance Ra, accounting for the viscous (Catanho *et al.*, 2012).

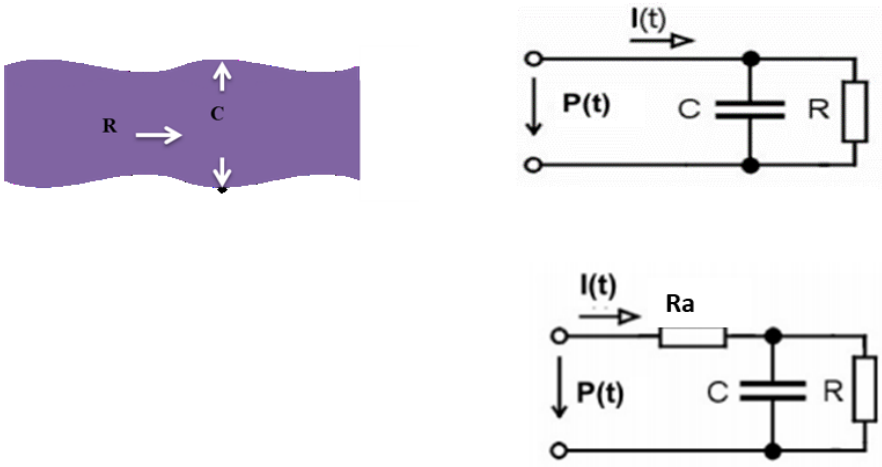

Fig. 1-25: 2-element and 3- element of Windkessel circuit as an analogue to vascular vessel.

Chapter 2:

Mechanical function of internal Jugular vein valve: post analysis of M- mode imaging under cardiac monitoring.

2.1. Background:

The presence of internal jugular vein IJV valve in the distal portion of the internal jugular vein had been widely described by anatomy and pathology studies (Sanchez-Hanke, Püschel and Leuwer, 2000; Fukazawa, Aguina and Pretto, 2010). Arguments and reports concerning the clinical significance of competent jugular venous valve had been included in medical literature. It had been demonstrated that the leaflets of normal valve are movable and should be oriented in the direction of the blood flow and they should move freely with respect to the respiration phases (Zamboni *et al.*, 2011). Since, IJV valve is the only protective vessel valve between the heart and the brain, the competence of this valve is crucial in maintaining the transcranial blood pressure gradient during cardiopulmonary resuscitation with closed chest compression (Ratanakorn, Tesh and Tegeler, 1999; Simka, 2014).

This valve also prevents a sudden increase in the IJV pressure during coughing or during positive pressure ventilation and may thus protect the brain from acute increases in intrathoracic pressure (Dresser and McKinney, 1987; Imai, Hanaoka and Kemmotsu, 1994; Furukawa, 2012). It was demonstrated in ultrasound sound colored Doppler studies that retrograde blood flow into IJV with or without Valsalva maneuver were considered as incompetence valve (Doepp,Valdueza and Schreiber, 2008; Shinn-Kuang Lin1, 2009).

The movement of Jugular valve was interrupted and considered the valve leaflets is heart circle dependent, the valve closes during diastole when the right atrium transmits pressure to the superior vena cava vein. During closure the valve bulges cranially into the lumen of the IJV causing a short transient spontaneous retrograde flow in the Doppler spectrum (Stolz, 2012). It is also the cerebral out flow is strongly impact by the competent and incompetent jugular vein valve.

2.2. Aim of study:

In this study, our hypothesis was to include the normal open time of jugular vein as a new indicator to evaluate the competent jugular vein valve. We implemented a post analysis on Jugular valve motion using M-mode image to estimate the open and closing time of internal jugular vein valve in normal young subjects.

2.3. Materials and methods:

2.3.1 Subjects:

The investigation was performed in the Vascular Diseases Center of the University of Ferrara, Italy. Twenty four volunteers of normal young students were undergone an ultrasound scan of the neck veins in supine position. The study included both gender, femals and males, their demograghic and characteristic is shown in Table 2-1.

Clinically they had no history of cardiovascular, hepatic, gastrointestinal, renal or cerebral diseases.

24 samples 16 male 8 female	Mean ± SD	Confidence intervals CI of confidece level 95%
Age (year)	21.79 ± 0.79	21.79 ± 0.32
Weight (kg)	60.39 ± 9.76	60.39 ± 3.9
Height (cm)	168.26 ± 8.54	168.26 ± 3.4
Body mass index BMI (kg/m^2)	21.22 ± 1.96	21.22 ± 0.78

Table 2-1: Subjects demographic and characteristic.

The subjects had been scanned in supin position with a fairly striaght head and during normal respirotary cycle. The US examinations were included both sides of the neck and were done by one experenice operator, using a Vivid-q ultrasound system (GE Medical Systems ultrasound, Horten, Norway) equipped with a linear probe (L11-8.12 MHz). The scanning was started with B mode of short axis view, the probe was placed in a transverse position on subject neck to identify IJV and carotid artery. The probe marker should face the subject's left side, corresponding to the marker on the ultrasound screen. Then, the probe was rotated by 90^o to obtain longitudinal axis veiw of IJV, Fig.2-1. We were looking particulary for the following creteria: Valve leaflets presence, in segment J_1 of IJV where the valve is usually situated, the presence of these intraluminal, curvilinear, mobile and echogenic structures was interpreted as valve projection. The cursor line was fixed on valve leafets on B mode to display the leaflets motion in accompination with real time motin mode, M mode. In this study, the valve was assessed for both sides of the neck including bicuspid leaflets and and

mono leaflet. The Doppler blood velocity wave was recorded immediately after M mode, which was frozen producing a screen shot. These techniques were applied to at least three cardiac cycles.

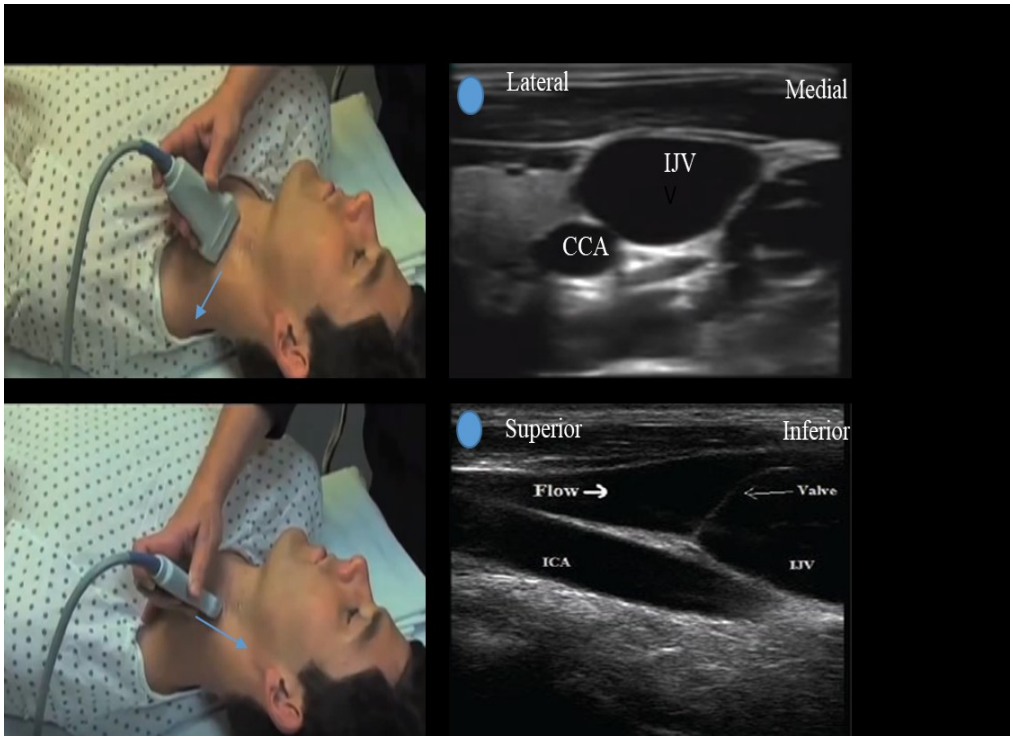

Fig. 2-1: B mode US examination of IJV valve. In short axis view, the prob marker oriented to the left shoulder while in long axis view, the prob marker oeiented to the head. The prob marker lines up to the orientation with the screen indicator spot.

The Doppler blood velocity wave was automatically overlapped by a line highlighting the mean blood velocity recorded in the sample volume. The sample volume was opened widely in order to cover almost the entire vessel lumen and was located at a short distance before the valve to avoid the echo interference between leaflet motion and blood velocity.

This study was conducted in accordance with the Ethical Standards of the Committee on Human Experimentation of the Azienda Ospedaliera Universitaria di Ferrara.

2.3.2. Image acquisition of M mode:

The IJV valve leaflet motion o f M mode image was sampled by extracting N pixels, (N≥25). Each pixel is of x and y coordinates indicating piexl position. The sampling interval was

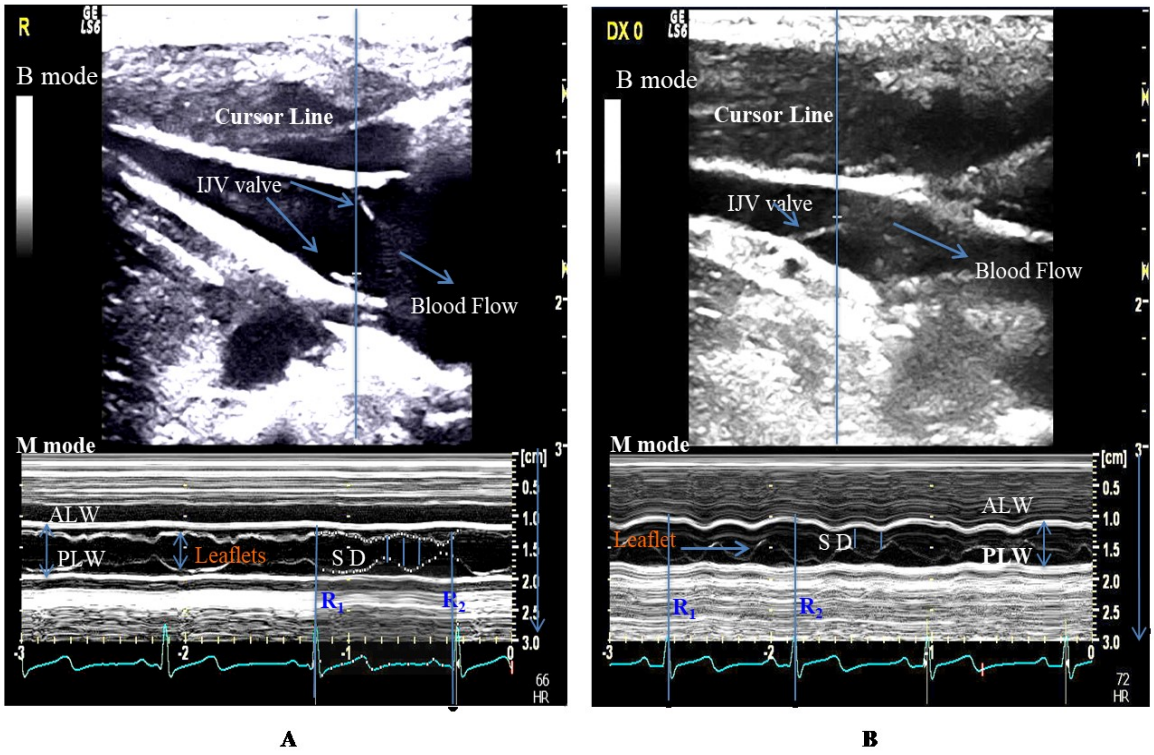

Fig. 2-2: A) IJV valve with two leaflets. (B) IJV valve with mono leaflet. SD is separation distances between two leaflets or between leaflet and lumen wall. Anterior lumen wall, ALW and Posterior lumen wall, PLW. The systolic component of ECG, R_1 and R_2.

equal to 10 pixels. We used multiple point tool measurement of ImageJ software to extract the pixels for IJV valve motion. The data in pixels saved in ImageJ software , as data of two axis, (x and y) axise. In which x axis indicates the pixel in direction of time and y axis indicates the pixel in direction of displacement. Then the data exported to Excle file to analyze. We extracted the data in pixels for two cardiac cycles in sequence, which each cardiac cycle starts and ends with the (x) axis equal to systolic components,R_1 and R_2 of ECG, respectively as it shown in Fig. 2-2.

2.3.3. Image acquisition of Doppler velocity mode:

Following the same techniqe used in M mode, we sampled the Doppler blood velocity trace by extracting data in pixels (N≥25). As it shown in Fig. 2-3, each pixel represented by x and y axis, where the x axis indicates the pixel in time direction while y axis indicates pixel in direction of velocity.

The extracted pixels were for two cardiac cycles, the Doppler velocity wave in one cardiac cycle started in equivalent to systolic compnente R_1 and ended in equivalent to next systolic

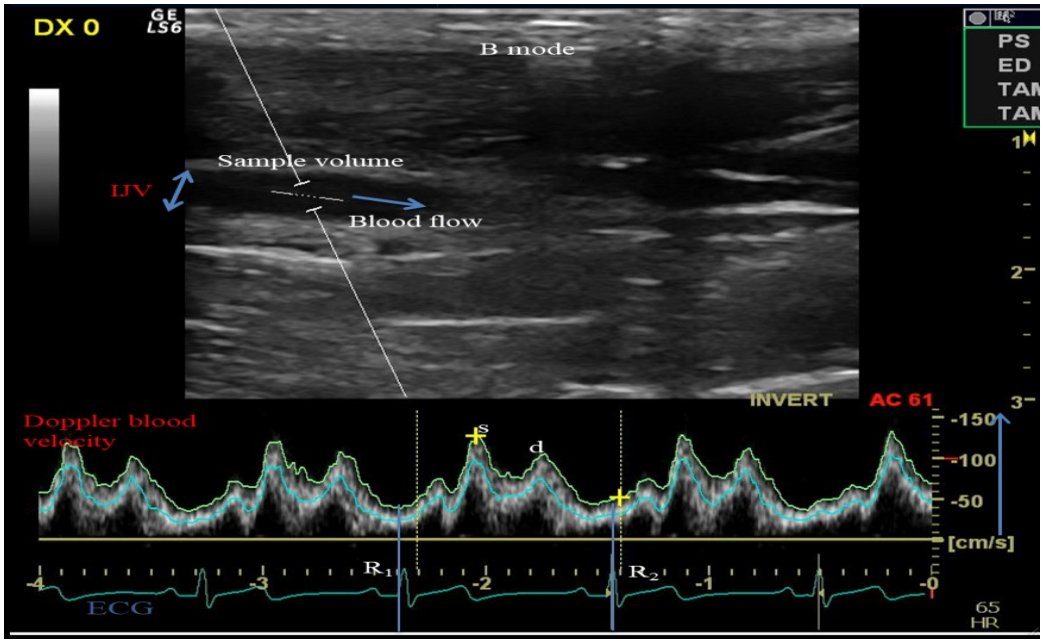

Fig. 2-3: IJV Doppler velocity wave of two peaks; s and d with a depressed velocity v. A normalized cardiac cycle between R_1 and R_2 of the ECG.

component R_2 of ECG.

2.3.4. Data aquisition of leaflet motion:

Since M-mode image is a real time motion for moving structure, we adjusted the M mode image to a depth of 3 cm, as a vertical distace, through the all scanning. According to that, we converted data in pixels into positions data, time intervals in seconds in direction of x-axis and distance in centimeters in direction of y-axis. Hence, we should calculate the time converted factor (**TF**) and distance converted factor (**DF**) of the M-mode image by following the concept of (sisini, 2015) method.

2.3.5. Calculation of TF and DF:

Data in pixels could be represented as two vectors, one through x axis presenting time in pixels and second vector through y axis presenting distance in pixels and it could be indicated by the following expressions:

1. $$\{(x_i)\}_{i=1}^{N}$$

2. $$\{y_i^A\}_{i=1}^{N} = \{y^A(x_i)\}_{i=1}^{N}$$

3. $$\{y_i^P\}_{i=1}^{N} = \{y^P(x_i)\}_{i=1}^{N}$$

4. $$\{y_i^{LW}\}_{i=1}^{N} = \{y^{LW}(x_i)\}_{i=1}^{N}$$

Where y^A, y^P are the distance vector in pixels for the anterior leaflet AL and posterior leaflet PL, as a function of x_i. Where (x_i) is time vector in pixels for the interval (i=1, 2, …... N). In case of mono leaflet valve, we include the lumen wall as a distance vector y^{LW} in regarding to AL or PL, equation 4. In this study, TF of M mode image is calculated for a normalized cardiac cycle under interval time, T=1 sec. Hence the TF is equal to one second divided by the total number of pixels within a cardiac cycle:

5. $$\{t_i\}_{i=1}^{N} = \left\{\frac{X_{i-}X_1}{X_N - X_1} \times T\right\}_{i=1}^{N}$$

In this way we convert data in pixels (equation 1) to data in time, seconds, (equation 5). In such way, we calculated DF by assuming that the whole pixels range in the vertical direction is in correspond to the depth image, L=3 cm. The DF is obtained by dividing L to the hieght in pixels M. The data distance in pixels were converted into data distance in cm following the next expressions including; AL, PL and LW):

6. $$\{AL_i\}_{i=1}^{N} = \left\{\frac{y_i^N}{M} \times L\right\}_{i=1}^{N}$$

7. $$\{PL_i\}_{i=1}^{N} = \left\{ \frac{y_i^{P}}{M} \times L \right\}_{i=1}^{N}$$

8. $$\{WL_i\}_{i=1}^{N} = \left\{ \frac{y_i^{LW}}{M} \times L \right\}_{i=1}^{N}$$

2.3.6. Separation distance of valve motion data acquisition:

In case of bicuspid valve, the separation distance SD of the two leaflets is the vertical distances between AL and PL through entire cardiac cycle. It is obtained by the following equations:

9. $$\{SD_i\}_{i=1}^{N} = \{|PL_i - AL_i|\}_{i=1}^{N}$$

Where the AL_i and PL_i are identified as vectors in direction of time parallel to x axis through equal time intervals (i.....N), as it shown in Fig. 2-4. In case of mono leaflet valve, the SD of mono leaflet are the vertical distances between AL (or PL) and lumen wall WL at the opposite side, The SD is obtained as the same manner:

10. $$\{SD_i\}_{i=1}^{N} = \{|WL_i - AL_i|\}_{i=1}^{N}$$

According to that, the coordinates of each pixel is expressed as:

11. $$\{t_i, SD_i\}_{i=1}^{N}$$

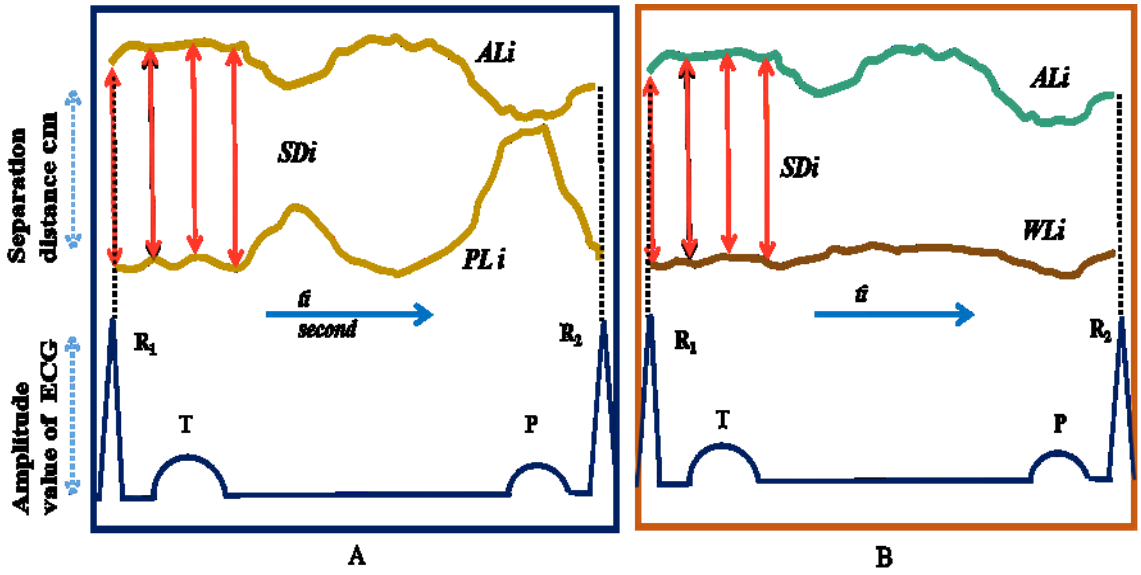

Fig. 2-4: Shematic of normilized cardiac cycle. The sampled leaflets motion syncronised with ECG components, started at R_1 and ended at next R_2. (A)the separation distance SD in IJV valve with two leaflets. (B) the separation distance SD in IJV valve with mono leaflet.

2.3.7. Data acquisition of Doppler blood velocity:

Doppler velocity image represents with two axis, velocity as a vertical axis and time as a horizantal axis. We converted the aquisition data in pixels into velocity - time data by calculating the velocity converted factor VF and time converted factor TF. The VF is obtained by dividing H, a selected velocity on image scale, to the hieght in pixels M. The data acqusition was equivalent to M mode data acqusition and the velocity vector in cm/sec. was expressed as follows:

12. $$\{v_i\}_{i=1}^{N} = \left\{ \frac{y_i^S}{M} \times H \right\}_{i=1}^{N}$$

where y_i^S is the velcity vector in pixels through the interval i=1,2,.....N.

2.3.8 ECG data equisition:

Data in pixels are extracted from ECG recording and mainly through the three main components of ECG recording, (Q RS wave, T wave and P wave).

The cardiac cycle is represented from R_1, (QRS-wave) to next R_2 of the second cycle. The acquired data in pixels was converted into time vector in second using the equivalent method of M mode but we kept the pixels in vertical direction without any change.

2.3.9 Leaflet position and Doppler velocity in pahse:

In order to put in phase, the leaflet position and Doppler velocity syncronised with ECG, We hypothized three steps followed in this study:

1-Since each cardiac cycle mostly has different interval as compared to the next cardiac cycle, we scaled the two cycles to the longest one.

2-The time instant corresponding to the first R_1 wave of the cardiac cycle was assumed as zero time for both the position and velocity data set. In this way we normalised each cycle under interval (T = 1.0 second).

3-In order to put in phase the Doppler blood velocity wave with M mode of IJV valve motion, we interpolated Doppler velocity data set with time data set of leaflet motion. The interpolation of data points was made by using IGOR sofware, in which a new data points was constructed within the range of discret set of original velocity data set. The new data was processed in line with time data set of leaflet motion.

2.3.10 The open separation distance ratio SDR:

The separation distance ratio $SDR_{(ti)}$ of the IJV valve is the SD (as a function of time) divided by the maximum SD_{max} of the valve through a cardiac cycle. It was calculated in the two scaled normalized cardiac cycles as it showed below:

7. $$\{SDR_{ti}\}_{ti=1}^{N} = \frac{\sum_{ti=1}^{N} SDti}{SD_{\max}}$$

The intervals ti are ($t_1, t_2, t_3 \ldots t_N$), where i value means of change in leaflet position to (N) intervals.

The open time of IJV valve was calculated in two methods, the first method named **OSDT** and the second method named the **logic test.** The both methods were described as follows:

2.4. Method $_1$ (OSDT):

The area under the curve $SDR_{(ti)}$ represents the opening time (OSDT) for the IJV valve through normalized cardiac cycle, started from (0 and ends at 1 second). The area (OSDT) was calculated between each two intervals by using trapezoids of equal width as presents in Fig. 2-5. The summation of area under the curve is equal to sum of areas of all trapezoids that can be drawn beneath the curve with the smallest width possible. The smaller the width, is the more accurate estimation of overall area, as presents in Fig. 2 -5. Following that the (OSDT) was calculated as:

8. $$OSDT = \frac{1}{2} \sum_{i=2}^{N} (t_i - t_{i-1}) \times (SDR_i + SDR_{i-1})$$

The calculations were made using Excel software.

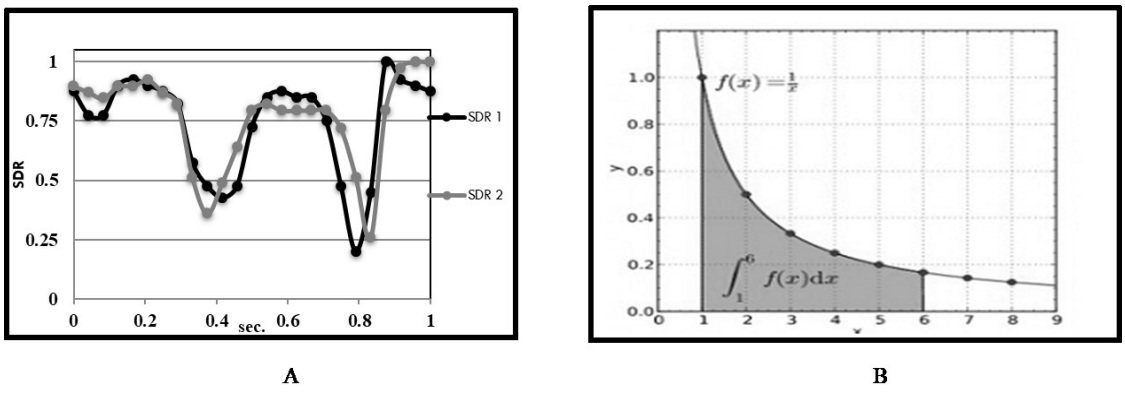

A B

Fig.2-5: Calculation of area under the curve by the sum of trapezoids areas. (A) The application of trapezoid area under a curve of function f(x). (B) SDR curve of two scaled normalized cardiac cycles.

2.5. Method $_2$ (Logical test):

1- Logical test of 0.5 threshold:

All SDR points locating in (>=0.5) is considered an open valve leaflet otherwise all SDR points locating in (<0.5) is considered closed valve leaflet. The open separation distance fraction ($OSDF_{\geq 0.5}$) and closed separation distance fraction ($CSDF_{< 0.5}$) are calculated as follows:

9. $$OSDF_{(\geq 0.5)} = \sum_{t=i}^{N} \frac{((SDR)i)_{\geq 0.5}}{((SDR)i)_{\geq 0.5} + ((SDR)i)_{<0.5}}$$

10. $$CSDF_{(<0.5)} = \sum_{t=i}^{N} \frac{((SDR)i)_{<0.5}}{((SDR)i)_{\geq 0.5} + ((SDR)i)_{<0.5}}$$

2-Logical test of 0.75 and 0.25 thresholds:

All SDR points locating in (>=0.75) is considered an open valve leaflet and all SDR points locating in (<0.25) is considered a closed valve leaflet. The SDR between these two thresholds is considered either a partial open valve or partial closed valve.

The open separation distance fraction ($OSDF_{\geq 0.75}$), closed separation distance fraction ($CSDF_{< 0.25}$), and partial open or partial closure ($PSDF_{0.25\text{-}0.75}$) are calculated in sequence as it follows:

11. $$\mathbf{O}SDF_{(\geq 0.75)} = \sum_{t=i}^{N} \frac{((SDR)i)_{\geq 0.75}}{((SDR)i)_{\geq 0.75} + ((SDR)i)_{<0.75}}$$

12. $$\mathbf{C}SDF_{(<0.25)} = \sum_{t=i}^{N} \frac{((SDR)i)_{<0.25}}{((SDR)i)_{\geq 0.25} + ((SDR)i)_{<0.25}}$$

13. $$\text{PSDF}_{(0.25\text{-}0.75)} = \sum_{i=i}^{N} \frac{((SDR)i)_{0.25\text{-}0.75}}{((SDR)i)_{\geq 0.25} + ((SDR)i)_{<0.25}}$$

Chapter 3:

Results and analysis

3.1. Leaflets motion and Doppler blood velocity in phasing:

Fig. 3-1, and Fig. 3-3, represent two samples survey with bicuspid valve of two cardiac cycle. The leaflets motion appears in phase with Doppler blood velocity synchronized to ECG recording. During entire cycle the leaflets are movable; It opens early when the leaflets diverge closing to venous wall. Followed by a short partial closure when the leaflets converge towards the middle of venous center, then diverge to reopen. The valve closes late completely at the end of the cycle. For the sample survey of mono leaflet, the leaflet moves in consequence of a rhythmical opening and closure, as it yields in Fig.3-2. This finding survey is majority of all samples (two leaflets and mono leaflet) exception at the late valve closure, the valve is not frequently complete closed, as we observe in each sample of mono leaflet.

A closer look to the leaflets motion shows that, the opening and closing cycles are linked to ECG recording and it consist of four phases contribute the dynamic leaflets:

1-Majority of the early valve opening occurs at mid systole (T wave). The second late open time occurs at mid diastole.

2-The partial closure (or partial opening) occurs at the beginning of diastole next to T wave while the late closure occurs at end diastole, the majority after P wave.

Regarding to Doppler velocity wave; the Doppler velocity wave was typically shows two positive waves and depressed velocity in between, the first peak velocity (s) occurs at end of T wave, a second late peak velocity (d) occurs at end of diastole, P wave. This finding is majority in 83% of the total samples (mono leaflet and two leaflets), Figs. 3-1, and 3-2. While 17% of total samples shows no phasic peaks, Fig. 3-3. The interpolating Doppler velocity wave to leaflet position reveals an information about how the Doppler blood velocity changes over time in parallel to leaflet motion. Accordingly, the illustrations show shift between the two waves, Doppler velocity and leaflet motion. For instance, the early positive wave (s) exhibits lately short after early leaflet opening. This evidence is the majority in all samples. Furthermore, the Doppler velocities show a reverse short velocity most frequently after P wave; as it is visible in Fig. 3-2. These observations include 70% of total samples. A small revers blood velocity could be seen at depressed velocity in 16% of total samples.

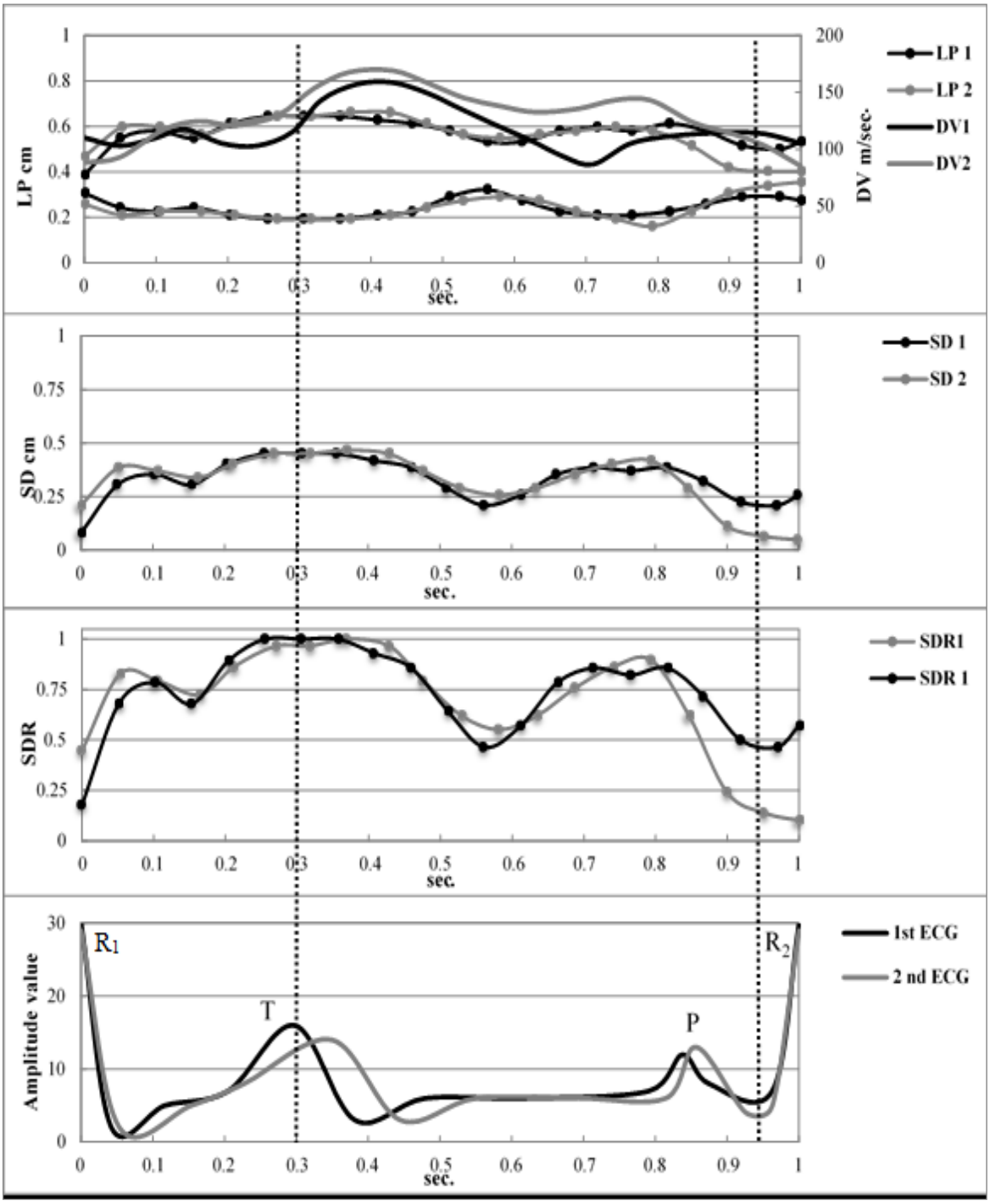

Fig.3-1: Sample survey of internal jugular vein valve with two leaflets. Figures from top to bottom A) The leaflets position LP is in phase with Doppler velocity DV synchronized with ECG recording. The leaflets open early at end T wave and closed at end diastole after P wave. Doppler velocity has two phasic peaks; (s) peak at end of T wave and (d) peak at end diastole with depressed velocity (v) at mid diastole. B) The separation distance (SD) between two leaflets. C) The separation distance ratio (SDR) between the standards (1 and 0). D) ECG recording in first cardiac cycle, black colored trend, and second cardiac cycle of gray colored trend.

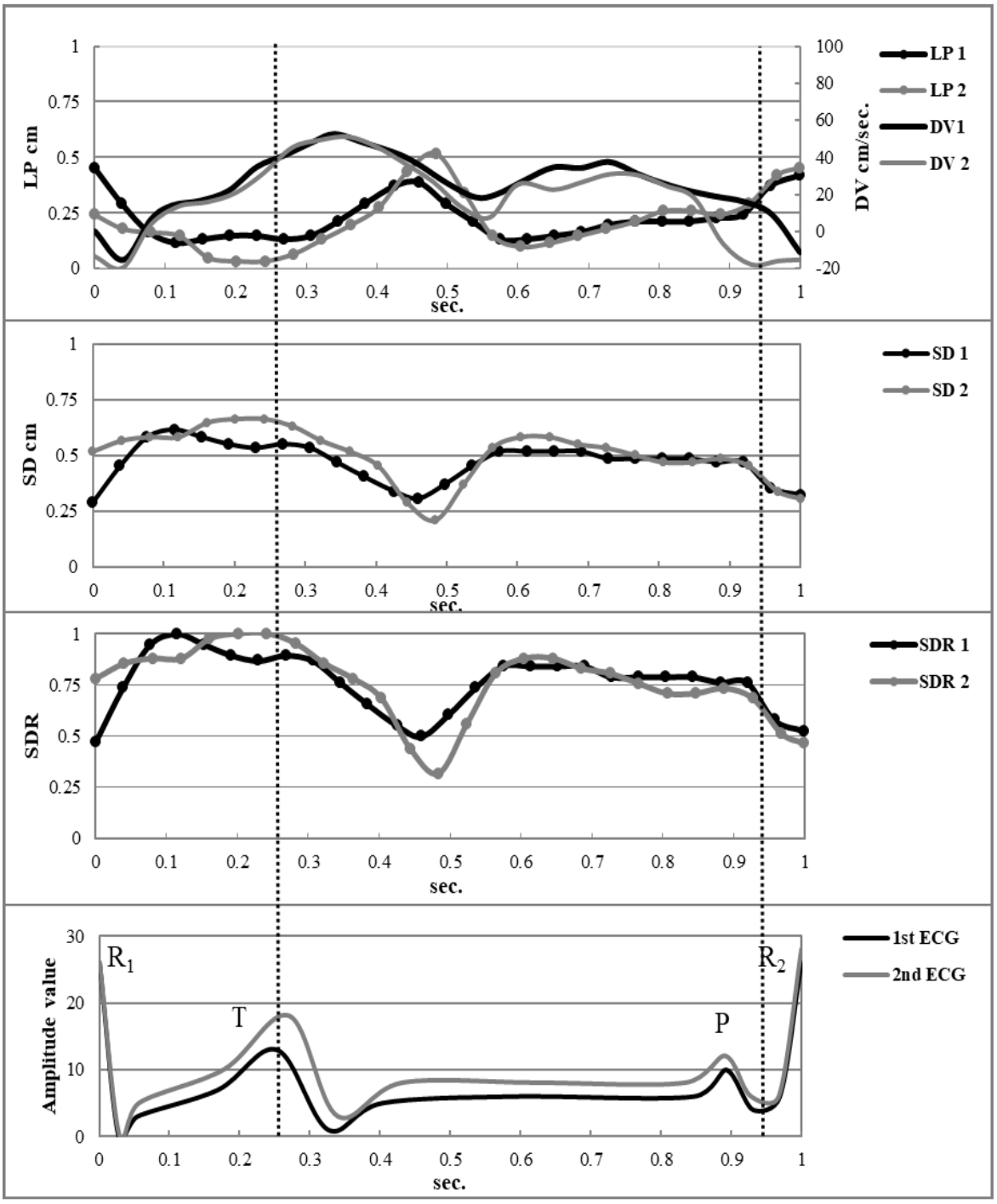

Fig.3-2: Sample2 survey of internal jugular vein valve with mono leaflet. Figures from top to bottom: A) The leaflets position LP is in phase with Doppler velocity DV synchronized with ECG recording. The leaflets open early at T wave and closed at end diastole after P wave. Doppler velocity has biphasic waves; (s) peak at end of T wave and (d) peak at end diastole with depressed velocity (v) at mid diastole. B) The separation distance (SD) between two leaflets. C) The separation distance ratio (SDR) between standards 1 and 0. D) ECG recording in first cardiac cycle, black colored trend, and second cardiac cycle of gray colored trend.

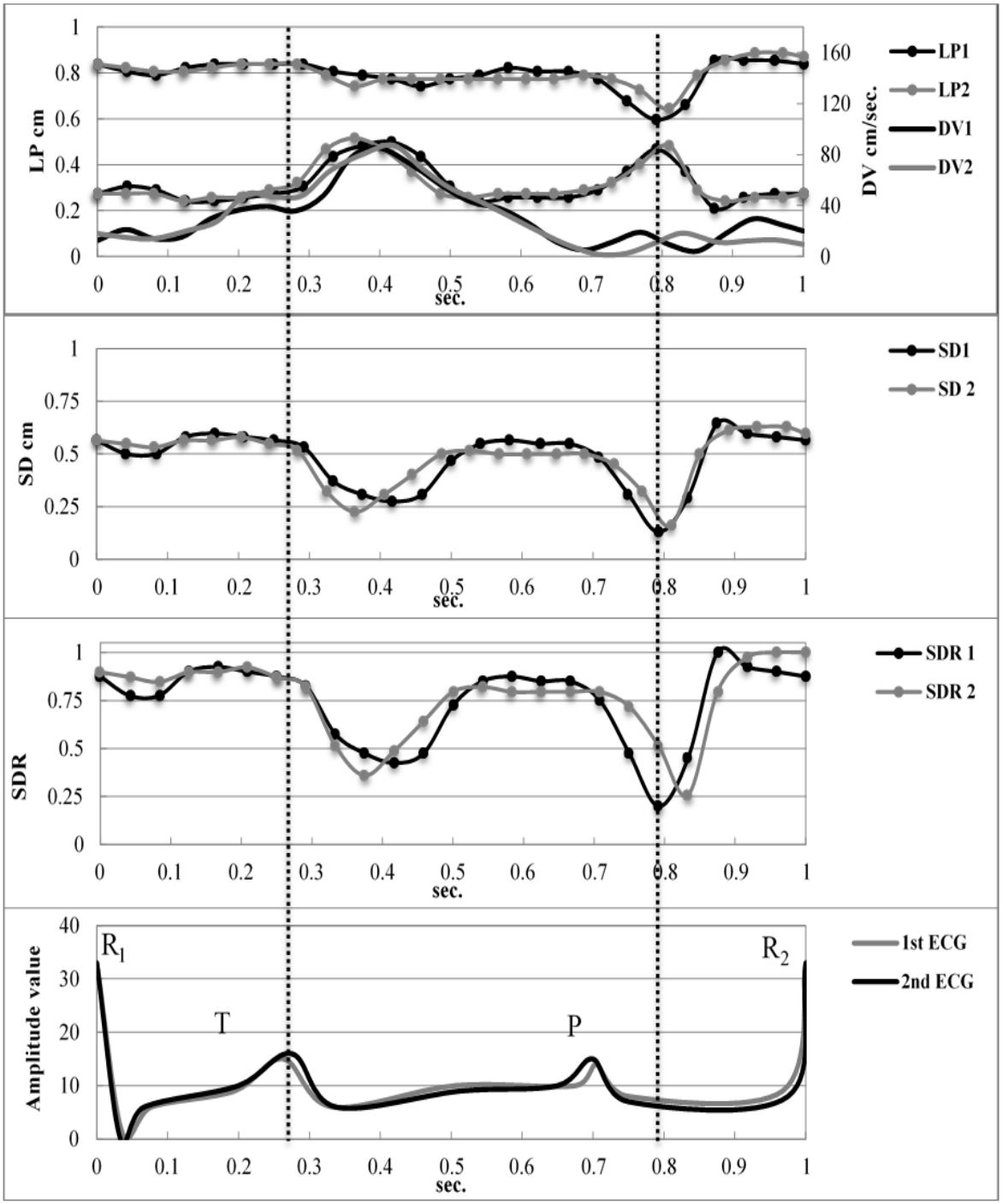

Fig. 3-3: Sample2 survey of internal jugular vein valve with two leaflets. Figures from top to bottom: A) The leaflets position LP is in phase with Doppler velocity DV synchronized with ECG recording. The leaflets open early at T wave and closed at end diastole after P wave. Doppler velocity has no biphasic waves; the peak velocity at end of T wave. B) The separation distance (SD) between two leaflets. C) The separation distance ratio (SDR) between the standards (1 and 0). D) ECG recording in first cardiac cycle, black colored trend, and second cardiac cycle of gray colored trend.

3.1.1. Leaflet separation distance SD:

Fig. 3-1 shows change in separation distance (SD) of the leaflets during entire cardiac cycle. It shows large SD through early valve opening; at mid systole (T wave). Followed by a small descending in SD next to T wave, then extended for the second time at mid diastole. Hence, SD declined to the lowest value, majority at end diastole after P wave. The SD in mono leaflet depicted a trend at the same manner of two leaflets as it shown in Fig. 3-2.

3.1.2. Separation distance ratio SDR:

The separation distance ratio SDR of the valve is changeful (mobile) between two standards, 1 and 0 during entire cardiac cycle, as it yields in Figs.3-1, 3-2, 3-3. The majority of large SDR occurs at T wave in total samples while the minimum ratio occurs at end of diastole. The trend of SD and SDR are in agreement with the leaflet position.

3.2. The trend patterns of open time concerning two methods:

In Fig. 3-4, it presents a stacked line chart including 24 subjects reveals the trend and pattern

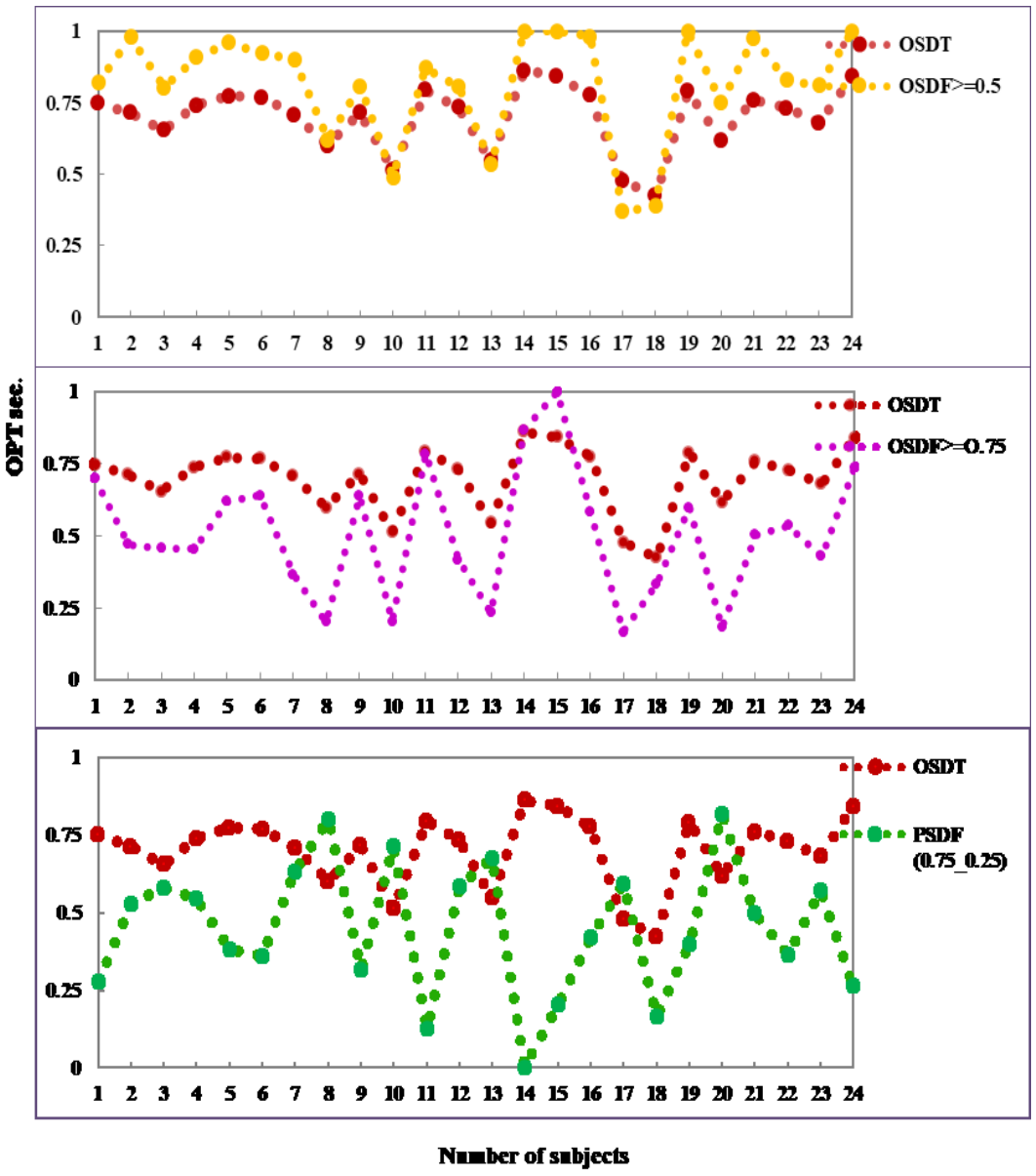

Fig. 3-4: stacked line chart to display the trend of normal open time regarding the two methods. Y axis presents the open time OPT, and x axis presents number of subjects. Open separation distance time OSDT in method1 is plotted as a reference to open fraction time OSDF of thresholds 0.5, 0.75 and (0.75-0.25).

of mean $OSDF_{\geq 0.5}$, $OSDF_{\geq 0.75}$ and $PSDF_{25\text{-}0.75}$ in regarding to OSDT through two normalized entire cardiac. The chart shows the strong compatible trend between OSDT and $OSDF_{\geq \mathbf{0.5}}$. While OSDT shows less compatible trend with $OSDF_{\geq 0.75.}$ The two stack lines, OSDT and partial separation distance reveals a high compatible inverted trends.

3.3. The distribution of open and closure time in cardiac valve cycle:

Fig. 3-5 shows the application of method2 in a normal sample survey. It reveals the open

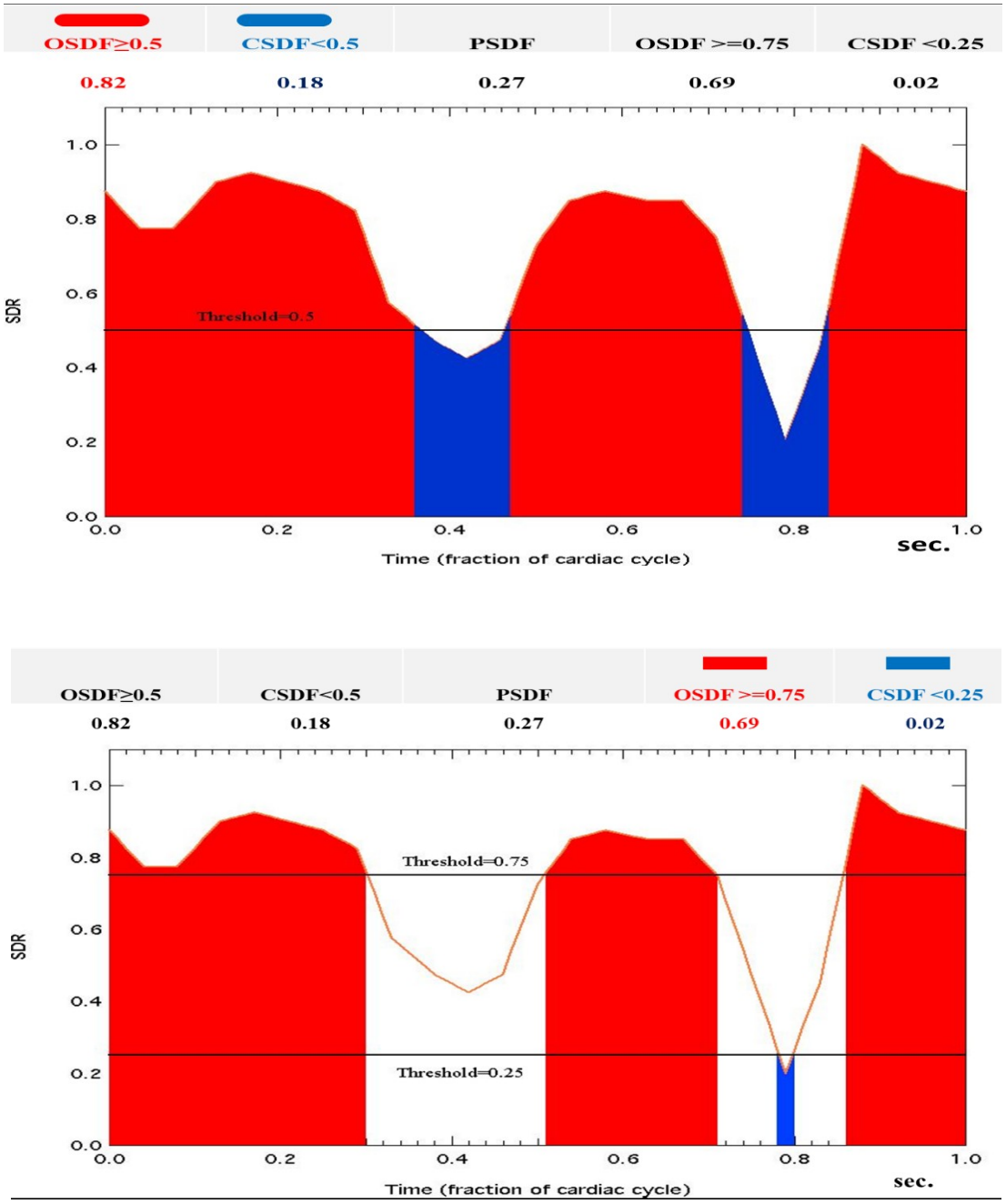

Fig.3-5: Application of method2 in a sample survey. The distribution of separation distance ratio SDR along thresholds 0.5, 0.75 and 0.25. The red area is of open time when the SDR is higher or equal to the thresholds 0.5 or 0.75. While the blue area is of closure time of valve when the SDR is lower than the threshold 0.5 and 0.25. The white area is the partial separation distance of the valve between the thresholds 0.75- 0.25.

and closure fraction time of first hypothesis, logic test of 0.5 threshold, distributing during entire cardiac cycle in a normal sample survey. The red area indicates the time when the valve opens while the blue area indicates the time when the valve is closing. As well as, the second part of the Fig 3-5 indicates the distributing of open and closure fraction time through the logic test of threshold 0.75 and 0.25. The red area which represents the open fraction time reveals smaller than the red area in logic test of threshold 0.5. And the blue area which represents closure valve, restricted in small area as compared with threshold 0.5. The remain area represents the partial opening /or closure time distributed in the white colored area.

3.4. IJV valve opening and closure time:

In Fig. 3-6: There is a significant positive relationship between the open separation distance time OSDT in method1 and open separation distance fraction ($OSDF_{\geq 0.5}$) in method2. The strength of correlation results is:

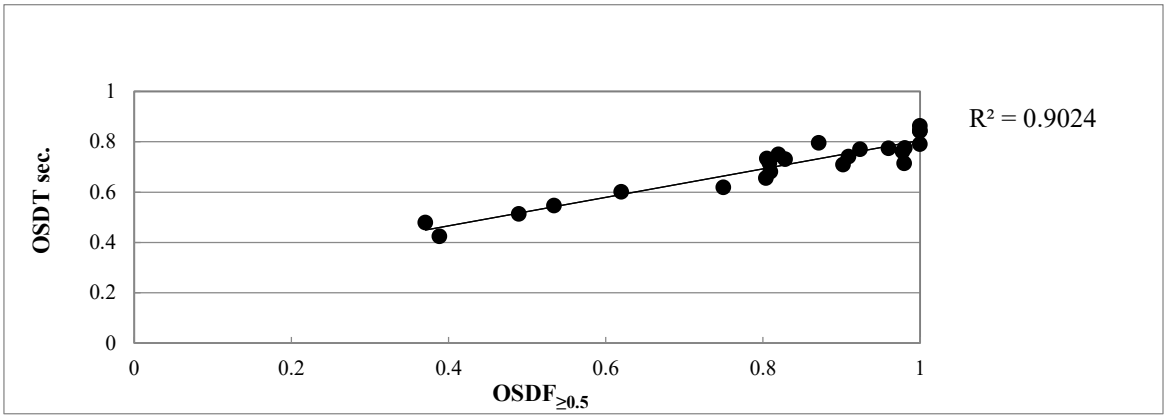

Fig. 3-6: The relationship between open time OSDT of method1 and $OSDF_{\geq 0.5}$ of method2.

degree of freedom equals to (df = 22), r (22) = 0.94, $R^2 = 0.9024$, ($P < 0.001$).

In Fig. (3-7), the closure time CSDT of first method1 reveals a significant positive relationship to the close separation distance fraction ($CSDF_{< 0.5}$) in method2. The strength of correlation results is: r (22) = 0.94, $R^2 = 0.9017$, ($P < 0.001$). The trend line is not with intercept to zero. In Fig. (3-8), a mediate significant positive relationship is found between the open separation distance time (OSDT) in method1 and open separation distance fraction ($OSDF_{\geq 0.75}$) in method2, the strength of correlation results is:

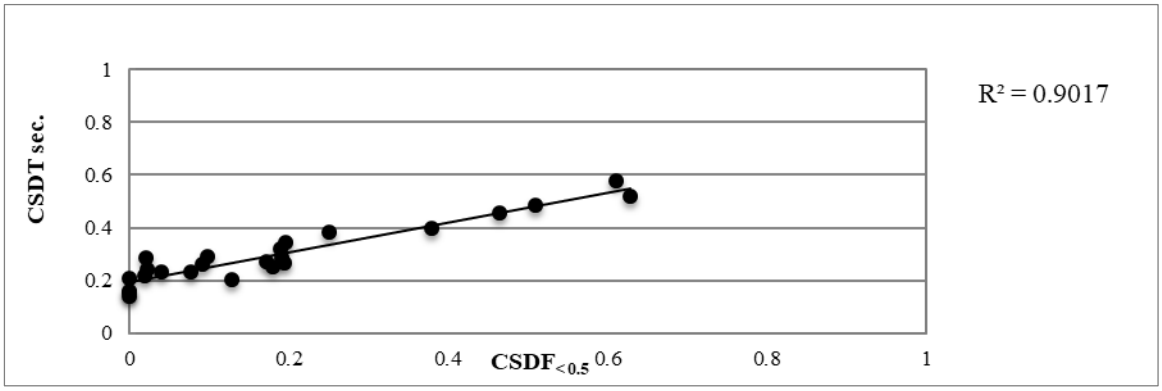

Fig.3-7: The relationship between closure time CSDT of method1 and $CSDF_{< 0.5}$ of method2.

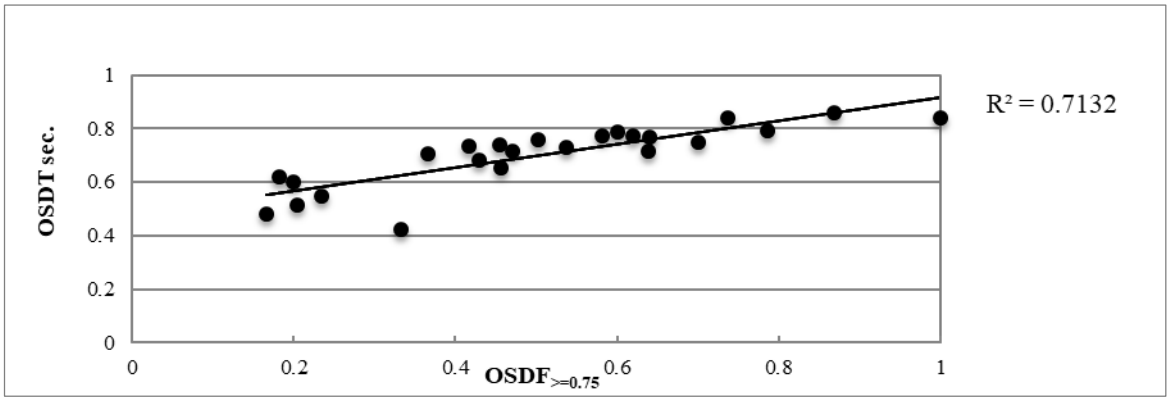

Fig.3-8: The relationship between open time OSDT of method1 and $OSDF_{\geq 0.75}$ of method2.

r (22) =0.84, $R^2 = 0.71$, ($P < 0.001$). The trend line is not with intercept to zero.

Consequently, in Fig. 3-9, it shows a mediate significant positive relationship between the closure separation distance time (CSDT) in method1 and close separation distance fraction ($CSDF_{< 0.25}$) in method2, the strength of correlation results is: r (22) = 0.72, $R^2 = 0.52$ ($P < 0.001$). The trend line is not zero intercept.

In Fig. 3-10, it shows a weak correlation $R^2 = 0.26$ of the inverse relationship between OSDT and partial separation distance fraction PSDF. As well, Fig. 3-11 reveals a low correlation, $R^2 = 0.26$ of positive relationship between CSDT and $PSDF_{0.25 - 0.75.}$

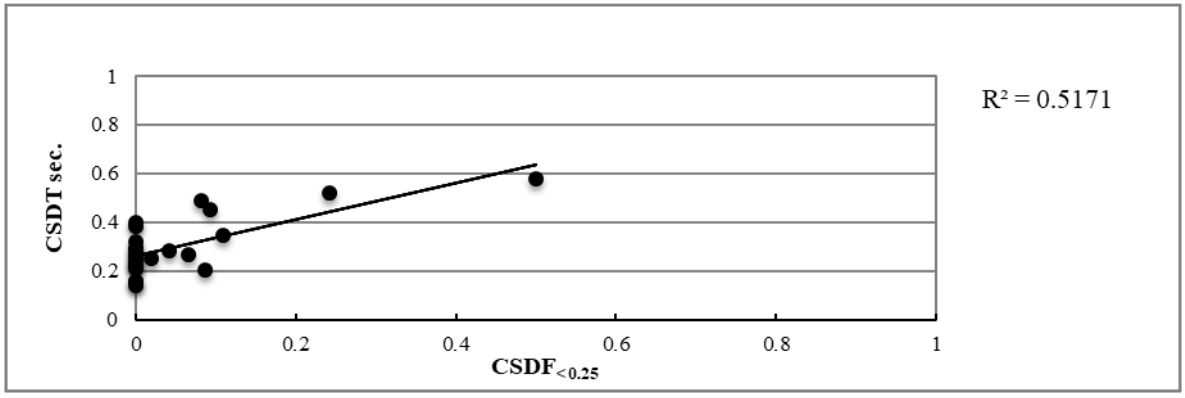

Fig.3-9: The relationship between closure time CSDT of method1 and $CSDF_{<0.25}$ of method2.

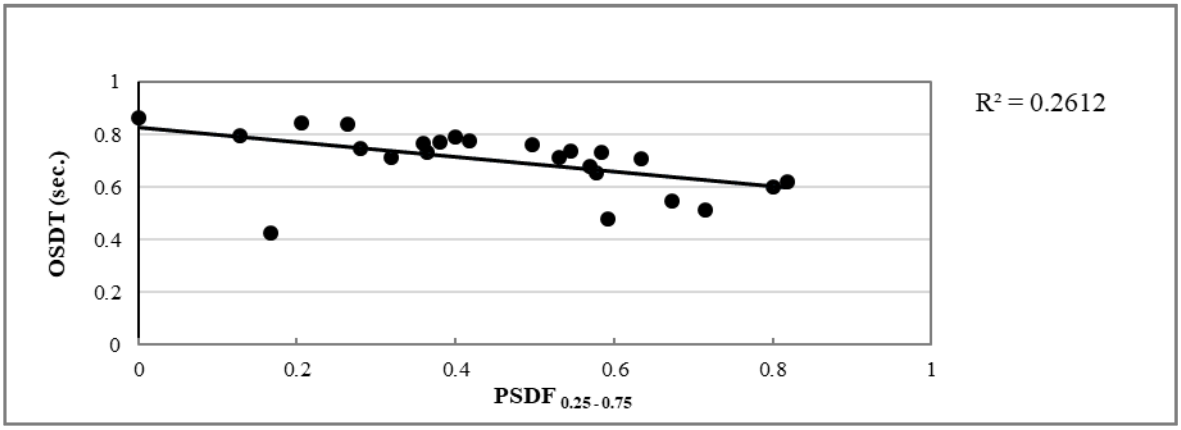

Fig.3-10: The relationship between open time OSDT of method1 and partial separation distance $PSDF_{0.25\ -\ -0.75}$ of method2.

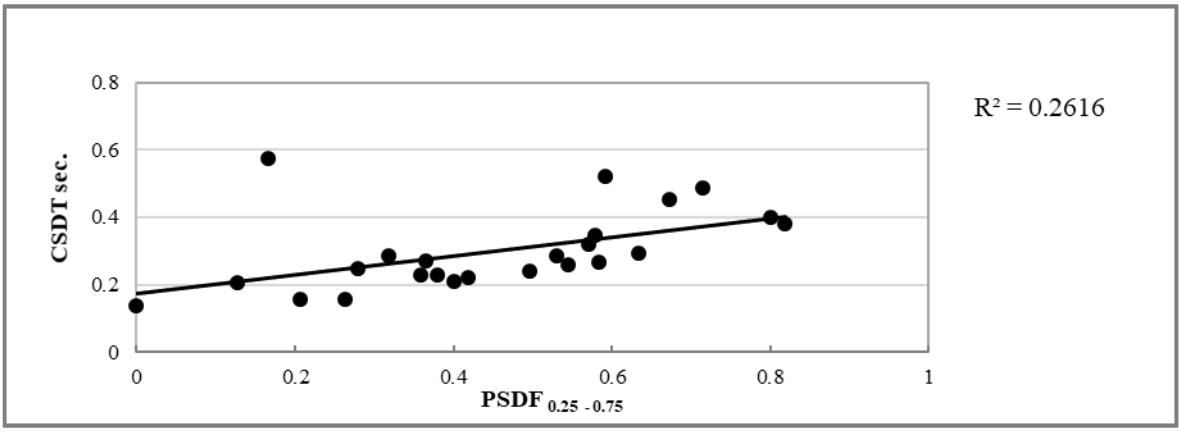

Fig.3-11: The relationship between closure time CSDT of method1 and partial separation distance $PSDF_{0.25-0.75}$ of method2.

3.5. Statistical analysis:

All data were presented as average values of two cycles. The values were expressed as mean ± standard deviation, Table 3-1.

The results yield that open separation distance time OSDT constitutes 70% of cardiac total time while the closure time CSDT is 30% of cardiac cycle.

In logic test method2, the $OSDF_{\geq 0.5}$ constitutes 81% of cardiac cycle while the CSDF constitutes 19% of cardiac cycle. For the threshold 0.75, the open time constitutes 51% of cardiac cycle while the percentage of closure time $CSDF_{<0.25}$ is 5% of cardiac cycle. The percentage of partial separation distance forms 45% of cardiac cycle.

Method1 Area under the curve SDR					
	OSDT sec.	**CSDT sec.**	**SD cm**	**Velocity cm/sec.**	
Mean	0.70	0.30	0.45	58.5	
± SD	0.12	0.12	0.20	34.97	
Method2: Logic test					
	$OSDF_{(\geq 0.5)}$	**$CSDF_{(<0.5)}$**	**$PSDF_{(0.25\text{-}0.75)}$**	**$OSDF_{\geq 0.75}$**	**$CSDF_{<0.25}$**
Mean	0.81	0.19	0.45	0.51	0.05
± SD	0.20	0.20	0.21	0.22	0.11

Table 3-1: Mean values and standard deviation (SD) of opening and closure time for two normalized cycles. method1 and method2. OSDT open separation distance time, CSDT closure time, OSDF open separation distance fraction, CSDF close separation distance fraction, PSDF partial separation distance fraction, SD separation distance.

The mean velocity resulted in this study is equal to 58.5 cm/sec. in segment J1 of IJV. And the mean separation distance of IJV valve in this study yield 0.45 cm.

3.6. Normality test of data:

All data including in method1 and in method2 were tested using four sorts of normality testing as it shown in Table 3-2.

Test	OSDT	CSDT	$OSDF_{\geq 0.5}$	$CSDF_{<0.5}$	$OSDF_{\geq 0.75}$	$CSDF_{<0.25}$
Shapiro-Wilk	0.0440	0.0502	0.0011	0.0011	0.6040	0
Jarque–Bera	0.1760	0.1838	0.0778	0.0778	0.7885	0
Anderson-Darling	0.0334	0.0405	0.0009	0.0009	0.8060	0
Cramer-von Mises	0.0266	0.0337	0.0017	0.0017	0.9079	0

Table 3-2: Testing normality of data using Shapiro-Wilk test (specific W) Jarque-Bera test (specific JB) Anderson-Darling test (A^2) Cramer von Mises test (CH).

Table 3-2 presents p-value for the corresponding test. Null hypothesis H0 – the data is considered normal distribution if P> 0.05. while the alternative hypothesis H1 is considered non normal distribution if P<0.05.

In Shapiro-Wilk test, the test of normality reveals non normal distribution for the all data except in $OSDF_{\geq 0.75}$ and CSDT which have a normal distribution (P>0.05). The Jarque–Bera test shows a normal distribution for all data (P>0.05). The four tests yield a common normality test distribution for the data of threshold 0.75, (P>0.05).

3.6.1 Q-Q plot normality test:

The Q-Q test shows non normal distribution for the data OSDT, CSDT, $OSDF_{\geq 0.5}$, and $CSDF_{<0.5}$ and it represents by the Fig. 3-12 and 3-13. The Q-Q plot shows a normal distribution for the data of threshold 0.75 (P>0.05), Fig. 3-12. This result is in agreement with the four normality test results.

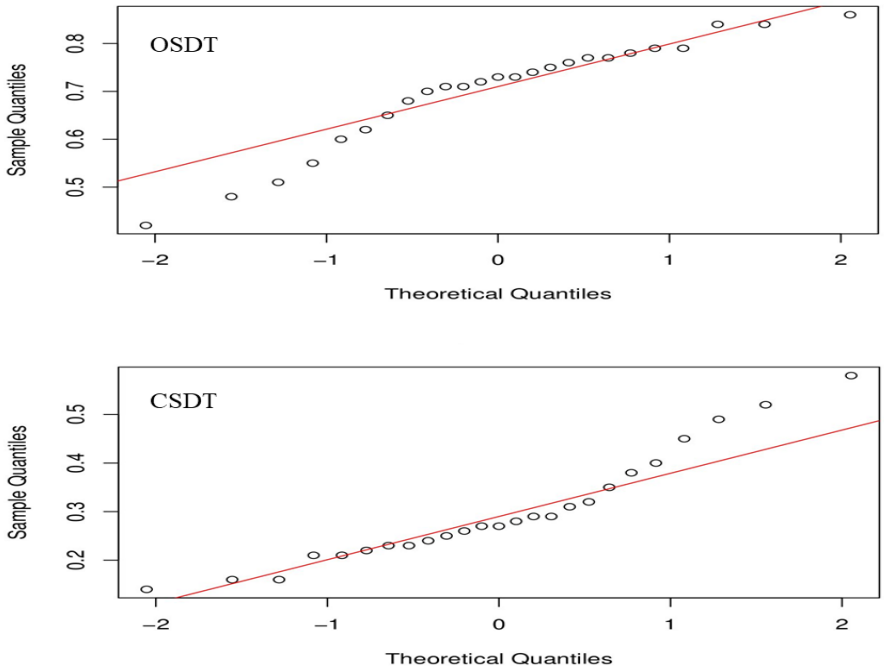

Fig. 3-12: Q-Q plot for normality distribution data test including OSDT and CSDT of first method1.

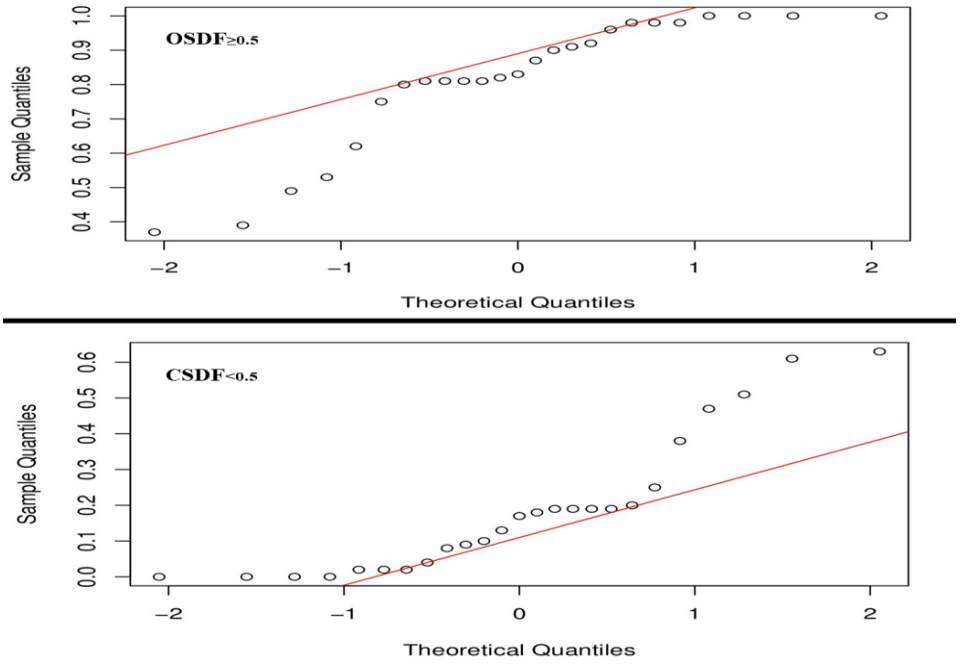

Fig. 3-13: Q-Q plot for normality distribution data test including $OSDF_{\geq 0.5}$ and $CSDF_{<0.5}$ of method2.

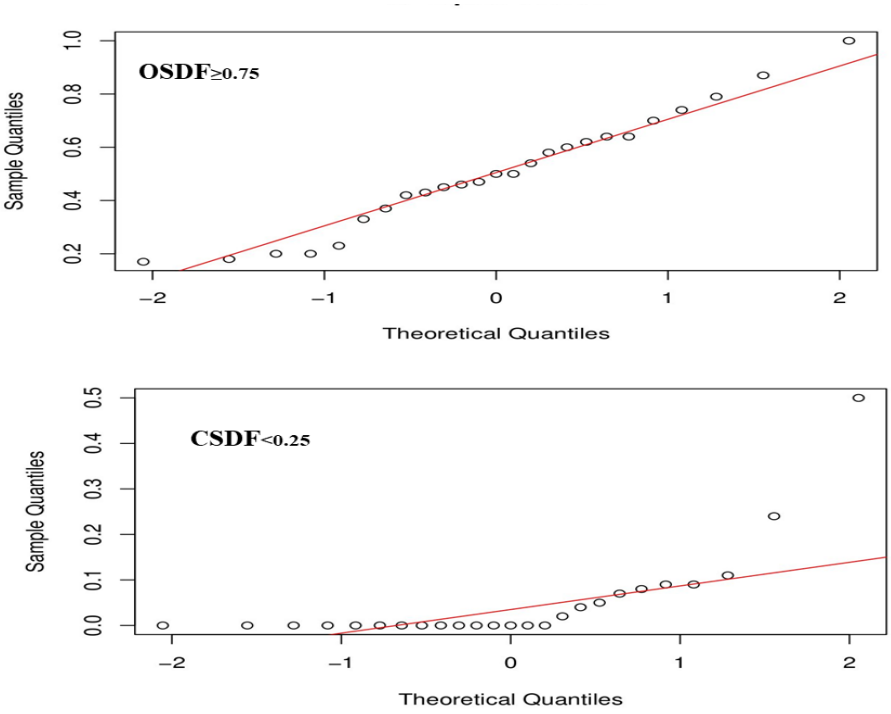

Fig. 3-14: Q-Q plot for normality distribution data test including $OSDF_{\geq 0.75}$ and $CSDF_{<0.25}$ of method2. Normal distribution is found for data in threshold (0.75).

Chapter 4

A model of mimicking blood loop to study the change in cerebral venous Outflow-Pressure waves modality upstream and downstream of Internal Jugular vein phantom.

4.1. Background:

The evaluation of the jugular venous pulse JVP provides valuable information about cardiac hemodynamics and cardiac filling pressures, which is defined as the heart preload at the end of diastole (Garg and Garg, 2000; Weyland and Grüne, 2009). Further, JVP gives information about the characteristic wave patterns pathologic of cardiac diseases (Chua Chiaco, Parikh and Fergusson, 2013), and an indirect estimate of the central venous pressure CVP which facilities the diagnosis and prognosis of many heart diseases (Drazner et al., 2001).

The JVP is defined as the expansion movement of IJV due to pressure change in right atrium RA. It reflects the alteration in RA pressure loading by cardiac cycle. The RA pressure can modify the negative pressure gradient which drives the blood from brain to RA (Reems and Aumann, 2012). Hence, it can modulate the IJV blood velocity (Sisini, 2016; Sisini *et al.*, 2016).

IJV is not known only as pulsatile vein but also it is a distensible (Guarracino *et al.*, 2014; Broilo, Meregalli and Friedman, 2015), and that highly flexible IJV adjust its shape to allow for transmission of the surrounding atmospheric pressure to the internal venous pressure of this collapsed vessel (Holmlund *et al.*, 2017). In ultrasound study US, it has been shown a strong relation between IJV cross section area CSA and the transmural pressure, which is the difference between internal venous pressure and atmospheric pressure. Therefore, the time diagram of the IJV cross section area obtained by ultrasound B mode facilities reflects on the JVP(Sisini *et al.*, 2015; Zamboni, 2016).

Abnormal jugular venous flow was classified into: markedly decreased flow velocity; pulsatile turbulent jugular venous flow and reversed flow. Possible causes of slow venous flow in the IJV include asymmetry of flow from the anatomical variations in cerebral venous drainage, incompetence of the jugular valve, increased central venous pressure JVP from congestive heart disease or tricuspid valve regurgitation, and increased intrathoracic pressure from pulmonary hypertension or obstructive pulmonary disease (Shinn-Kuang Lin1, 2009). Retrograde flow in the IJV with or without a Valsalva maneuver during sonographic study is considered as IJV valve incompetence. It is thought to be the major cause of venous flow retrograde (Furukawa, 2012) and therefore, theoretically the incompetence valve results in blood stasis occurs in IJV leading to local thrombus formation.

4.2. Aim of the study.

In this study, our goal is to add compatible experiment study to the cerebral drainage relative to flow-pressure wave form relationship upstream and downstream of IJV phantom. We hypothesized that a pulsatile propagation waves of both flow and pressure should be modulated when entering the collapsible IJV phantom.

Three phantoms are included in this experiment, two phantoms of similar elasticity material, the first one with bicuspid valve build up, the second one with no valve construction. The third phantom is with different elastic material but in similar construction of first phantom. We repeated the experiment by using each individual phantom.

There are three major issues to address: 1) The measurements of flow wave and pressure wave form obtained upstream and downstream of IJV phantom through a normal drainage out pathway (considered normal CVP, normal venous return). 2) The flow and pressure waves form measurements obtained upstream and downstream of IJV phantom through abnormal increased drainage load (increased CVP, impaired of venous return) (Barbeito and Mark, 2006; Reems and Aumann, 2012). 3) The effect of increased or decreased cerebral out flow in wave form patterns in normal and abnormal situations.

4.3. Protocol of cerebral drainage experimental model:

4.3.1. Basic concepts:

In this study, we developed a hydraulic experimental model in analogue to an electrical model based on Ohm's law and Kirchhoff's law concepts. In electrical circuits, voltage is the decrease in charge *q* from an electric source, such as a wall socket or battery to a ground value. Change in voltage or increase resistance across the circuit loop elements decrease the fluent current, I, according to Ohm's law ($R = \frac{V}{I}$), (Robbins, 2017). Kirchhoff's law states that the sum of all currents entering the junction must be equal to currents sum out of that junction. And all the sum of potential differences across all elements around the loop must equal to zero around any loop (Nilsson and Riedel, 1996).

We constructed a cerebral flow resistance and an increased loading resistance according to hydraulic resistance (R) related to vessel's diameter and blood rheological properties,

Poiseuille's law application represented by equation 4-1, (Paul Peter Urone, 2012; Kelly A. Young,Long Beach, 2013):

$$R = \frac{8\eta\ell}{\pi r^4} \qquad 4\text{-}1$$

Where $\boldsymbol{\eta}$ is the blood viscosity (Dyne. sec./cm^2), hydraulic resistance R of length, l in cm, and internal diameter, r in cm. The corresponding resistances in this study are represented

Hydraulic resistance	**CR-GG**	**LRA**
ID cm	0.32	0.32
Length cm	28.5	40
Hydraulic resistance mmHg/ml	28.18	32.37

Table 4-1: Characteristic of hydraulic resistances; cerebral resistance CR-GG and increased loading resistance LRA, internal diameter ID of resistance.

by CR-GG as a cerebral resistance to flow and increased loading resistance LRA can be connected in series or parallel in flow loop.

The characteristics of both resistances is shown in Table 4-1. The difference in pressure ΔP and Q is assumed as a standard linear relationship:

$$\Delta P = R\,Q \qquad 4\text{-}2$$

The developed hydraulic experimental model in analogue to the electric circuit is shown in Fig. 4-1. The model was proposed by the basic work of (Ursino and Lodi, 1997; Schollenberger, Figueroa and Pfaller, 2015).

The cardiac pump (voltage supply) pumps the blood as a constant cardiac output, stroke volume per min, creating an arterial pressure inside the loop. The total cerebral blood flow is the sum of the blood through the right and left carotid arteries and the basilar artery, all inflow Q_{in} is assumed to gather in single vessel entering the skull with systemic arterial pressure P_a.

The cerebral blood flow is totally lumped into two branches, the right branch includes 3 - element Windkessel model, in which the proximal resistance indicates CR-GG as cerebral resistance; the capacitance C_{IJV} in parallel to resistance R_{IJV} indicates the IJV equivalent resistance R_{eqIJV} connecting to the right terminal branch RTB of 2 – element Windkessel model (R_1 in parallel to C_1), represents by the equivalent resistance R_{RTB}. The right branch is in a counterpart of left branch representing by a proximal resistance equals to CR–GG connected to the left terminal branch LTB of 2 – element Windkessel model (R_2 in parallel to C_2), the equivalent resistance represents by R_{LTB}. This branch is considered as a remain compartments of cerebral flow drainage that are not include IJV. The two branches emerge into one terminal vessel trends to the pump input /or right heart (right atrial RA) with atrial filling pressure RAP.The Pa drop, indicates the voltage gradient, varies the currents across the resistances through the loop branches. (Magder, 2016), by applying equation 4-2 as analog to Ohm's law at each branch, we got:

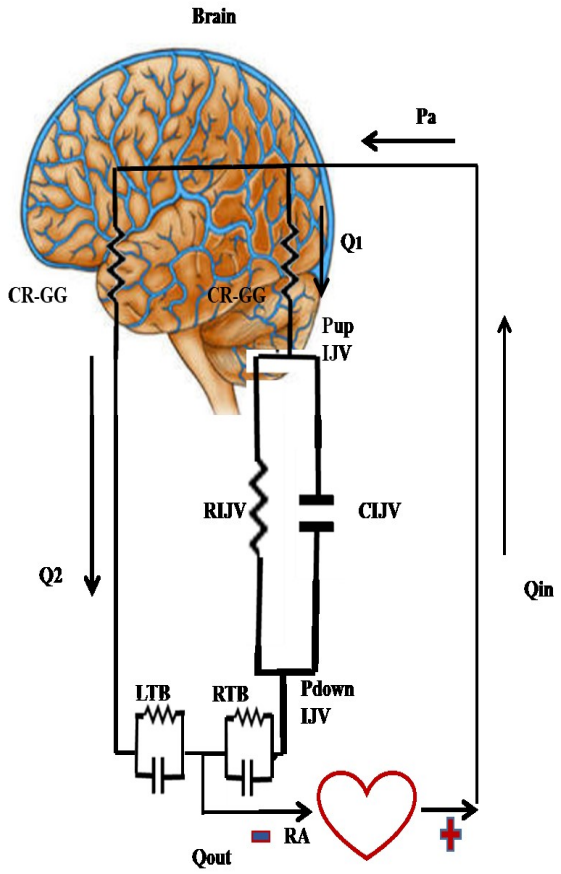

Figure 4-1: The electric circuit analog to cerebral out flow drainage; arterial pressure Pa entering brain, the pressure drops upstream and downstream of IJV, cerebral resistance CR-GG, capacitance in parallel to resistance indicate complainant vessels.

4-3 $$P_{right} = ((CR\text{-}GG) + R_{eq\ IJV} + R_{RTB})\ Q_1$$

4-4 $$P_{leftt} = ((CR\text{-}GG) + R_{LTB})\, Q_2$$

4-5 $$\Delta\left(P_{up} - P_{down}\right) = \mathrm{R}_{e\ qIJV}.Q_1$$

P_{left} and P_{right} represents the arterial pressure drops through the left and right branches. The equation 4-5 represents the driving pressure between upstream pressure P_{up} and downstream pressure P_{down} of IJV.

4.3.2 Analogy between electrical and cardiovascular behavior:

The quantities which characterize the fluid dynamics and their electrical analogues are displayed in Table 4-2, (Creigen, *et al.*, 2007; Kokalari, Karaja and Guerrisi, 2013)

Fluid dynamics	**Physiology variables**	**Electric analogue flow loop**
Mimicking blood flow Q (m^3/min.)	Blood flow (ml/sec.)	Current I (Volt/Ohm)
Pressure (Pa = (J/m^3)	Blood pressure ΔP (mmHg)	Voltage difference ΔV (Volt)
Viscosity Η Dyn.cm²/sec.	Blood resistance Poise = 10 Pas $\eta = \frac{R\pi r^4}{8I}$	Electrical resistance R
Poiseuille's law	$Q = \frac{\Delta P}{R} = \frac{\Delta P \pi r^4}{8\eta l}$	Ohm's law: $\Delta I = \frac{\Delta V}{R}$
Elastic coefficient	Vessel's wall compliance. $C = \frac{\Delta V}{\Delta P}$	Capacitor C
Compliant vessels	IJV phantom RTB LTB	Capacitor C connecting in parallel to resistance R
Hydraulic resistance	CR-GG LRA	Resistance connecting in series or parallel.

Table 4-2: The quantities which characterize the fluid dynamics and their electrical analogues

4.4. Materials and method:

4.4.1. Hydraulic fluid loop:

The project was completed in the Biomedical Ultrasound Research Laboratory in the Department of Physics &Astronomy, University of Western Ontario, London, Canada.

A programmable pump (Comp Flow 1000, Shelley Medical Imaging) had been used in this study. The pump is a volumetric displacement pump, it generates a waveform based on a programmed flow-rate wave form of specified peak, and corresponding mean flow volume rate (Holdsworth *et al.*, 1991).

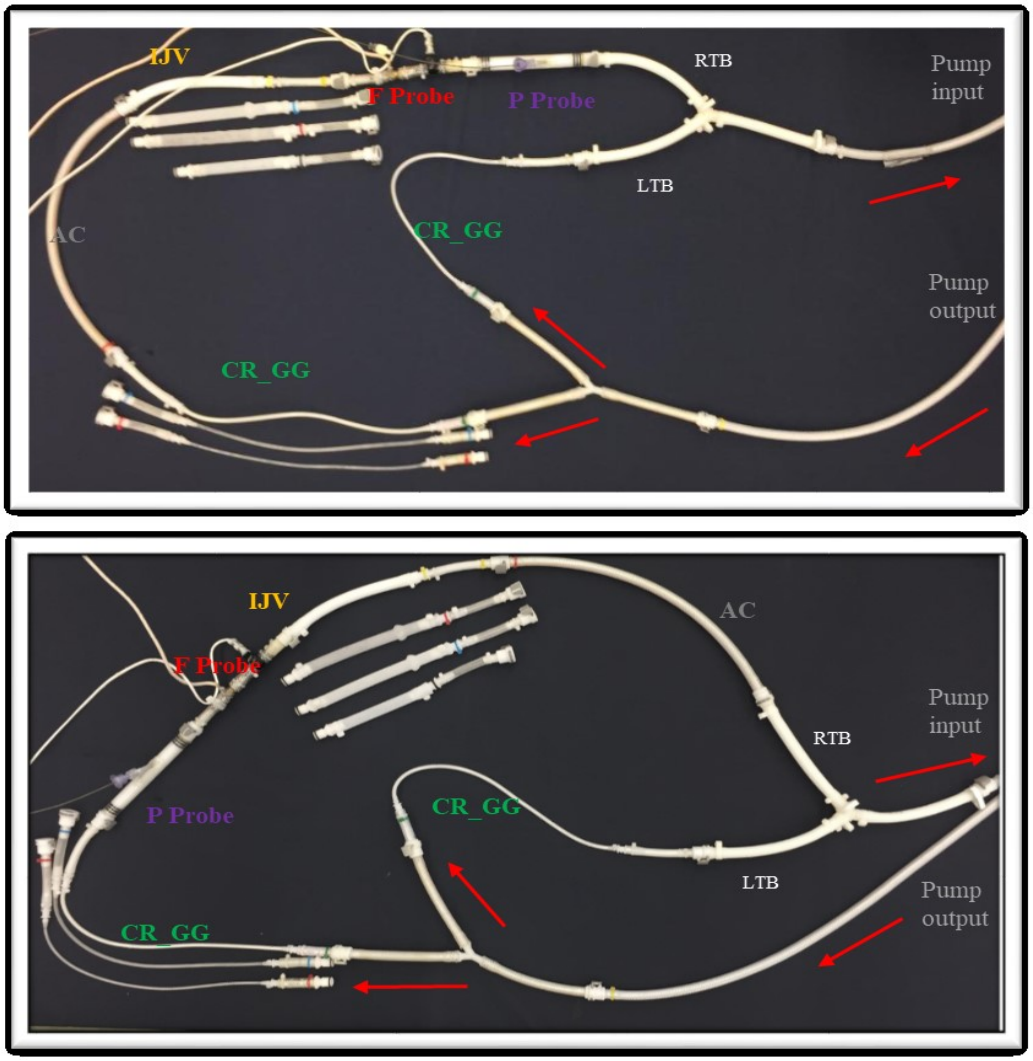

Figure. 4-2: Hydraulic loop model connected to Shelley pump. The first loop, the Pressure probe, P probe, and flow probe, F Probe connected downstream of internal Jugular vein IJV phantom, alternative connector AC, cerebral resistance CC-GG, right and left terminal branches RTB and LTB. The second loop, the F probe and pressure probe connected upstream of IJV phantom.

Simple pulsatile flow rate wave form was implemented (carotid2), which consisted of a single systolic increase (hump) in the waveform shape, as shown in Fig. 4-4. We set up the hydraulic mimicking fluid loop to represent cerebral flow drainage loop, as presented in Fig. 4-2. It starts with long rigid bifurcation connector connected to pump output. One branch, includes CR-GG connected in series with IJV phantom while the second branch consists only CR-GG to represent an alternative cerebral blood flow out pathway. The two ends of the branches are connected to the second Y- bifurcation spongy connector, the right terminal branch RTB and left terminal branch LTB relative to input pump, then the termination of Y bifurcation tube is connected to pump input as was depicted in Fig 4-2.

The flow and pressure waves were recorded by inserting an electric sensor pressure probe in line with an electromagnetic flow probe. Each probe is connected with a converted sensor to connect it later to a digital acquisition (powerlab) system in order to analyze the signals. To display the signals, the powerlab system was connected to a computer provided with LabChart software viewer, which displays signals as a continuous wave, Fig. 4-3. In order to retrospectively synchronize the flow and pressure waves we recording the ECG-type

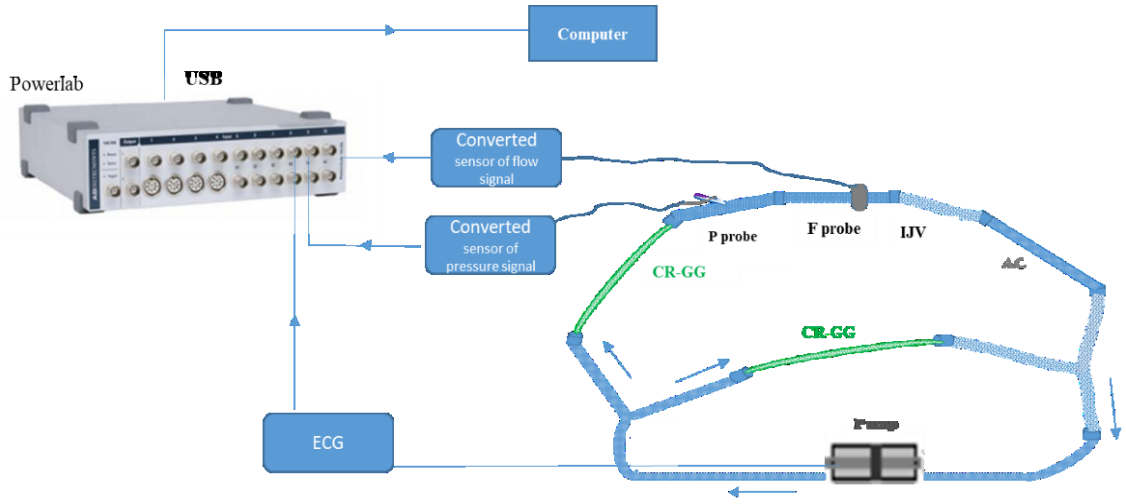

Fig. 4-3: Hydraulic analog schematic loop connection with flow meter, powerlab and computer provided with labchart software, Pressure probe, P probe, Flow probe F probe, internal Jugular vein IJV phantom, alternative connector AC, cerebral resistance GG-CR. ECG device connected between the pump and powerlab.

signal from the pump.

4.4.2. Edit carotid2 wave using Shelley pump software:

1. The cardiac cycle was chosen to start with small tail before the increased systolic wave (hump) and ending with long tail, Fig. 4-4. The start of the cardiac cycle was fixed by a green spot. This fixed green point indicates the cardiac cycle start corresponding to

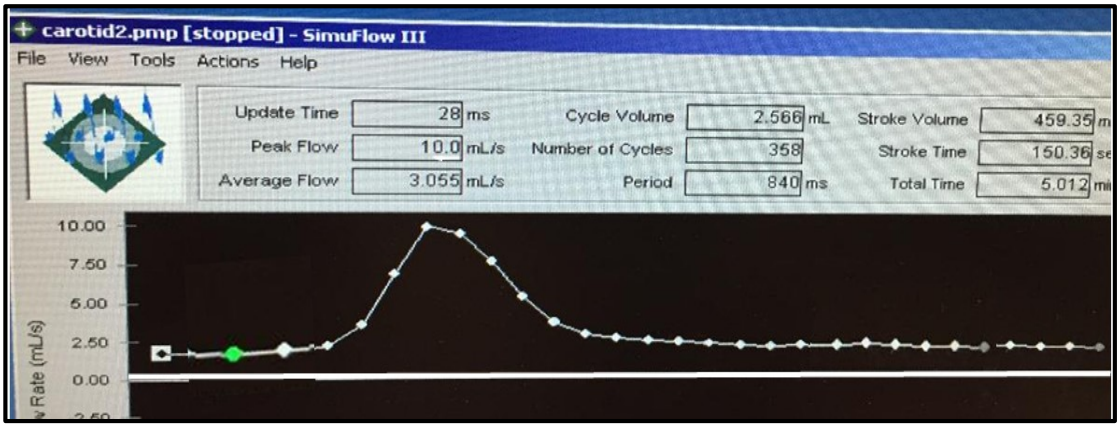

Fig.4-4: Carotid2 wave editing using Shelly pump software; Peak flow rat 10 ml/sec.

systolic component Q in an ECG recording. The interval of the cardiac cycle was 0.84 sec.

2. The pump outflow was implemented for three different peaks flow rates: (10, 20, and 30) ml/sec.

4.4.3. IJV phantoms characteristics:

The IJV phantoms with bicuspid valve build up IJVV are labeled once with blue as, IJVV-B and the second with labeled red, as IJVV-R. The IJV phantom with no valve build up is labeled with black IJV-B. The dimensions of the phantoms are presented in Table 4-2. The two phantoms with valve build up are equal in size but different in material. The two material used to model the phantoms were Dragon Skin silicones and Sorta clear silicon rubbers. Dragon Skin silicones rubbers are highly performance material, strong and stretchy.

It stretches many times its original size without tearing and will rebound to its original form without distortion. They are used in a variety of applications ranging from creating skin effects to modeling casting, Dragon Skin® 10 silicone is the material used to model the two

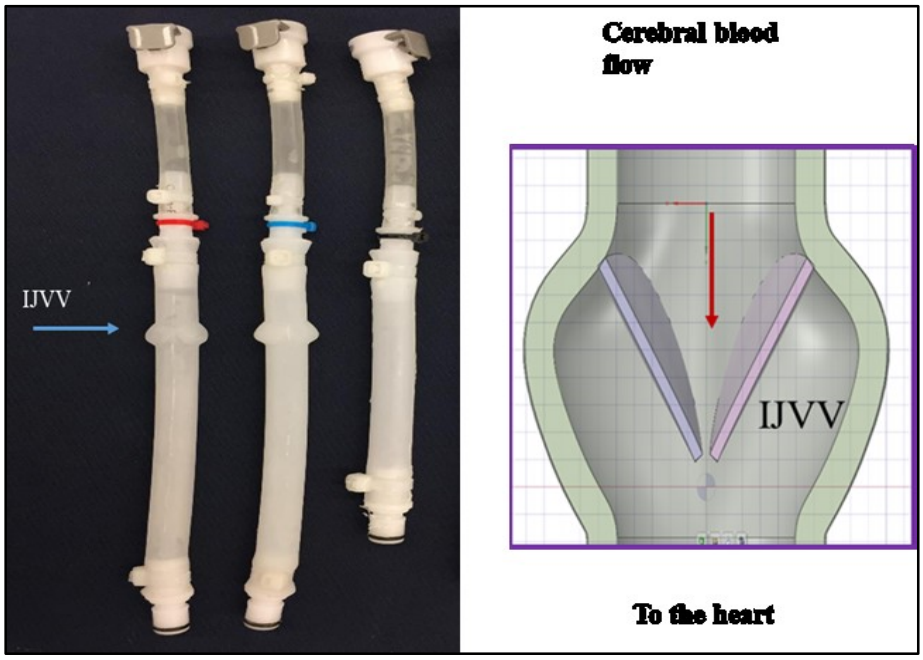

Fig. 4-5: Three phantoms models, two of them provided with valve IJVV (label blue and red), label black is one with no valve. The right side represents the valve with two leaflets build up.

phantoms, IJVV_B and IJV_B. Sorta clear® silicones are ideal for making prototype, jewelry or other molds of any configuration where model visibility is important (i.e. extracting a model from the mold via cutting). Sorta-clear silicon is the material used in modeling IJVV_R.

Phantoms	**IJVV_B**	**IJVV_R**	**IJV**
ID cm	1.1	1.1	1.1
Length cm	17.5	17.5	12.5

Table 4-2: Characteristics of Phantoms with valve build up IJVV and phantom with no valve IJV.

4.4.4. Valve basic modeling:

The phantom modelling based on preparing the valve geometry in CAD software, as shown in Fig. 4-5, and created a 3D model based on this geometry. The mold was 3D printed on fused-deposition 3D printer, and 2-part silicones were injected into the mold to create the final valve model. The source of final designing is provided by the company, Archetype Medical Inc. (www.archetypemedical.com).

4.4.5. Single branch of hydraulic resistance:

We measured the hydraulic resistance by disconnecting the left branch of the loop, in Fig, 2-2, using a valve of one direction, cut off the flow fluid in left branch, and insert the flow and pressure probes downstream of the hydraulic resistance in the right branch yielding a single loop (right branch only). Since we assumed a linear relation of pressure and resistance, we implemented our measurements by supplying the fluid loop with a constant flow volume from the pump and at three rates 5, 10, and 15 (ml/sec.). The measurements of flow and pressure were taken at each flow rate by collecting the data sets displayed in flowchart software viewer and exported as txt file to analyze in Excel, Fig. 4-6.

The data sets of flow and pressure were expressed as three mean values corresponding to the three flow rates. Using a linear fitting curve, we estimated the values of our resistances used in this research. The measurements include CR-GG and LRA resistances.

In the same manner, using single branch, we performed a calibration for the flow and pressure sensors at the beginning of each experiment to examine the function of the probes.

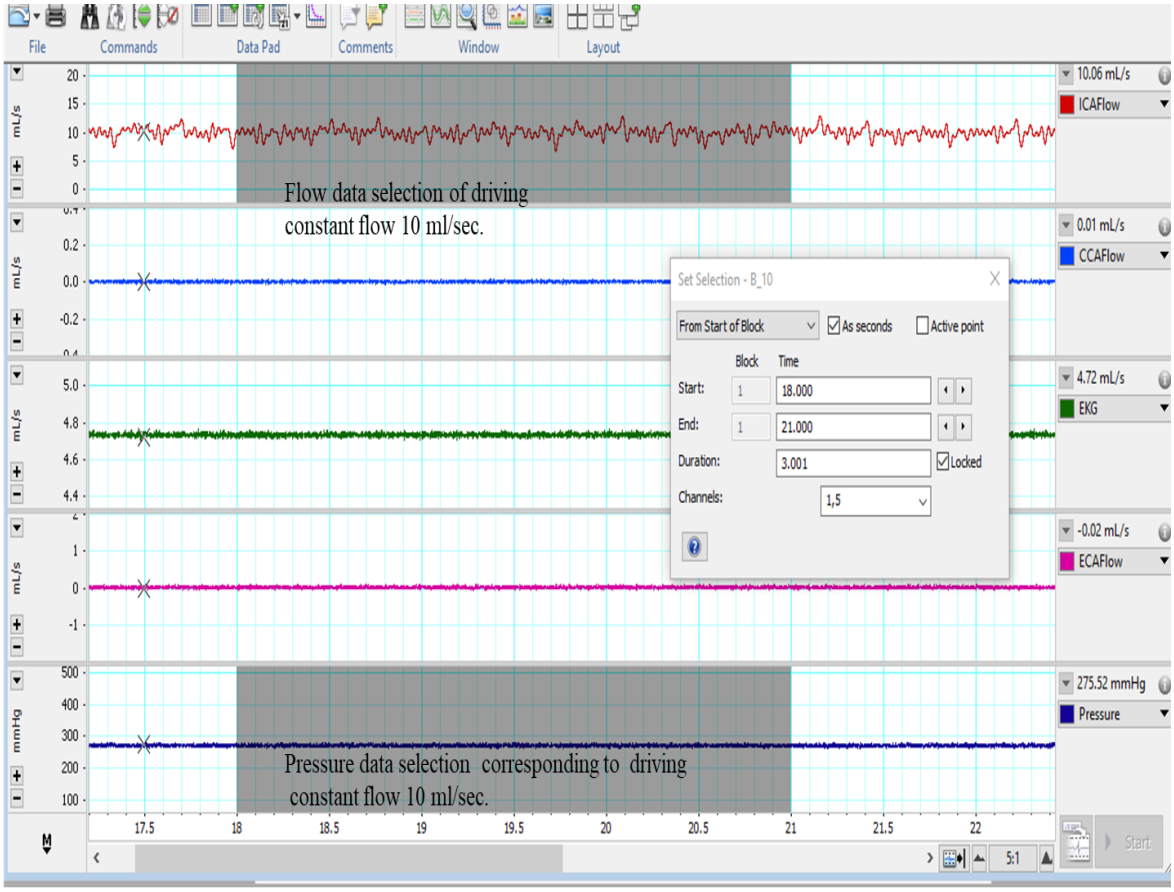

Fig. 4-6: Flow data acquired of peak flow rate 10 ml/sec. corresponding to pressure acquired data. The acquired data was saved as a txt file and exported to Excel to analyze.

4.4.6. Preparation mimicking fluid BMF:

To mimic the use of real blood with red blood cell suspensions, we prepared a blood-mimicking fluid (BMF) used for flow loop experiment. The described BMF is an ultrasound compatible fluid that mimics the bulk viscosity and the ultrasound properties of blood (Ramnarine *et al.*, 1998). The procedure involves the mixing of specific materials, Table 4-3. The mixed solution is later: filtered by using peristaltic pump and filter, degassed, viscosity tested by using viscometer and, if necessary, altered to refine the viscosity of the BMF, the procedure is discussed in detail in (Thorne *et al.*, 2008). The prepared BMF, is free of any possible contaminants. All the characteristic components of BMF and their percentage weight is displayed in Table 4-3. The normal human blood viscosity ranges between (3.5 – 4.5) mPa.s., the corresponding blood mimicking fluid BMF it should be 4.1 mPa.s., as we used in this experiment, (Ramnarine *et al.*, 1999)

Components		
	% weight	**per 1000 gm**
Distilled Water	83.86%	838.6g
Glycerol	10.06%	100.6 g
Dextran	3.36%	33.6 g
Orgasol 2001 UD NAT 1 (5um)	1.82%	18.2 g
Synperonic (orig)/Jet-Dry (TLP)	0.90%	9 g
Total	100%	1000g
CA24	0.3%	3g

Table 4-3: Mixing proportion of blood mimicking fluid for US (BMF-US)

4.5. Data acquisition:

The propagation waves of the flow and pressure inside the hydraulic BMF loop synchronized with a regular repetition of Q wave, systolic component in ECG recording are picked up by the flowmeter and electric digital pressure probes, in which basically, the sensors of each probe converts the flow and pressure signals into an analog electrical signals which is then converted to a digital signal in the PowerLab system. In this system the signal can be amplified (amplify small signals), filtered (remove unwanted frequencies or noise) and digitized (Aziz, Simonetta and Forrester, 2006).

The digitized data are then displayed on the computer as a waveform using Labchart software. The software displays data in real time with the system plotting the sampled and digitized data points and reconstructing the original waveform by drawing lines between the points. Our data acquisition displayed in three separate channels in Labchart software viewer, starting from flow waves signals, ECG wave and pressure signals, as it shown in Fig. 4-7. We acquired 10 cycles of flow and corresponding cycles of pressure, starting with Q wave as a reference point of the cardiac cycle. The data of cycles are saved and exported to analyze using matlab software. At each measurement, data acquisition was executed by opening a new file in labchart, followed by resetting pressure inside the loop to zero using zeroing bridge in labchart software, then the pump was started to generate the flow at a selected peak flow rate (10 ml/sec.).

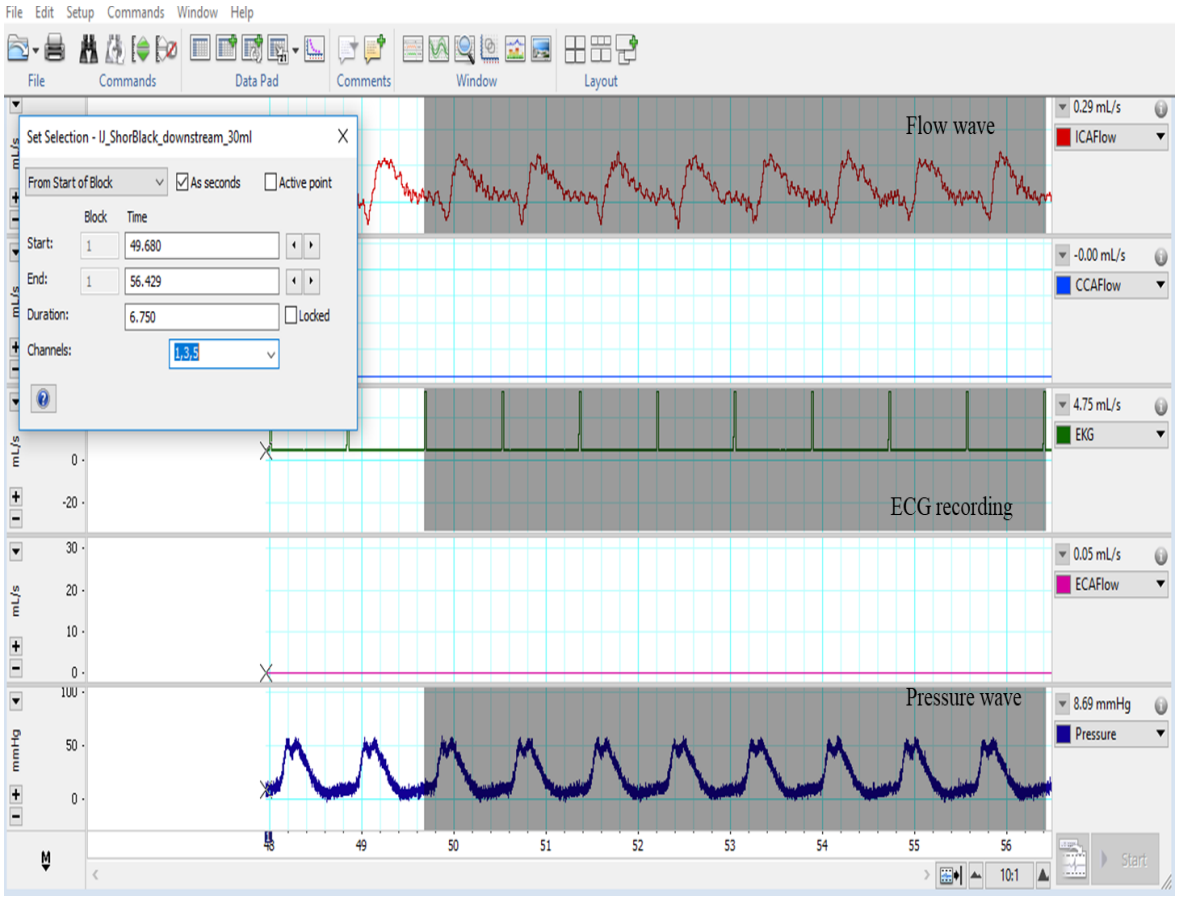

Fig. 4-7: Flow data signals and pressure data signals displayed continuously in time with ECG recording in between. The acquired data were for 10 cycles in sequence starting from Q component of ECG and ending with starting wave 11.

The data acquisitions regenerated in two circumstances:

1. The flow and pressure probes were inserted upstream and downstream of IJV phantom and the data acquisition represented a normal cerebral blood flow out pathway, as presented in Fig.4-2.

2. The measurements (upstream and downstream) were repeated by adding hydraulic resistance LRA at the flow terminal loop of pump input, as it presents in Fig. 4-8. This was considered as a pathological change downstream of IJV, increasing central venous pressure CVP. Each data acquisition was executed for three peak flow rates 10, 20, and 30 ml/sec.

In order to keep the acquired data at the same consistency, the alignment of both flow and pressure probes were not inverted through their connection upstream and downstream of IJV as it shown in Fig. 4-2.

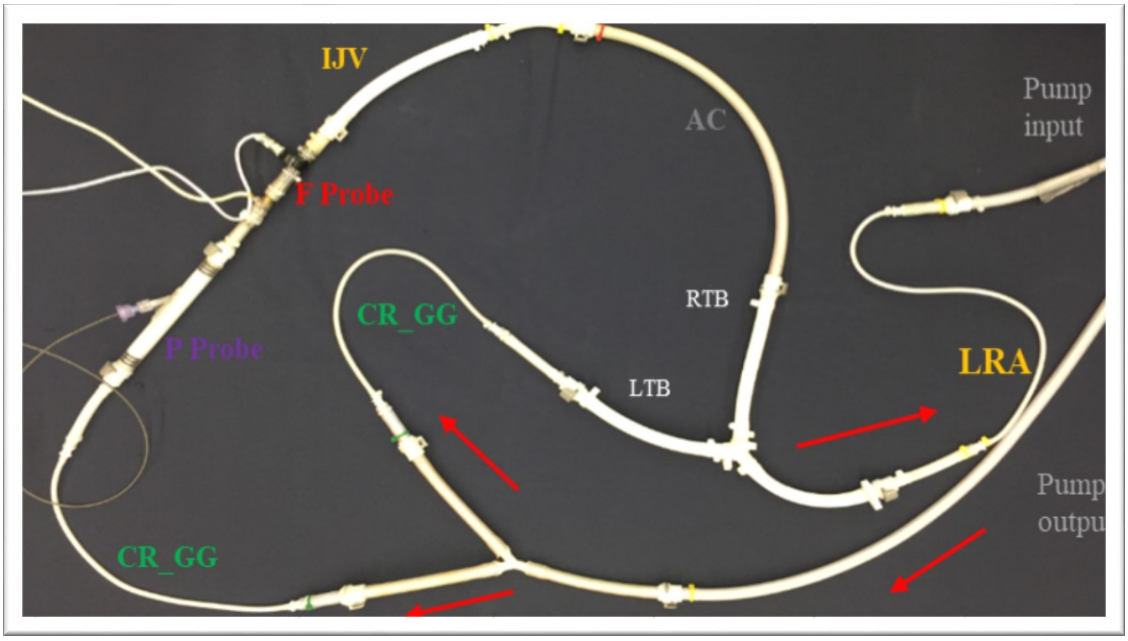

Fig. 4-8: Hydraulic loop model connected to pump. The first loop, the pressure probe, P probe, and flow probe, F Probe connected upstream of internal Jugular vein IJV phantom, alternative connector AC, cerebral resistance CC-GG, right and left terminal branches RTB and LTB, hydraulic resistance LRA as pathological changes downstream of IJV drainage.

Also we added a connector tube AC, considered as an alternative connector, to substitute the positions of the probes inside loop connections as shown in Fig. 4-2.

Chapter 5

Results

5.1. Internal jugular vein phantom IJV-B, no valve builds up.

5.1.1 Flow wave and Pressure wave samples.

Fig. 5-1, presents the scaled average flow measurement for three different flow peaks of driving pump 10, 20 and 30 (ml/sec.). Since the linear relationship of the pressure to the driving flow rate is equal to the total resistance of the fluid loop, which is equal to constant R, we scaled each flow wave sample to its pump peak flow. According to that, we scaled the pressure wave sample to its corresponding driving peak flow of the pump.

In Fig. 5-1A. the flow wave sample at positions upstream of IJV-B phantom starts with short damping tail followed by an increasing flow rate and then descends to lowest flow rate ending with longer tail. This flow wave modality is the majority for the three scaled flow samples at position upstream, in exception to the flow wave sample of 10 ml/sec. peak flow, in which, a short back flow occurs after the peak flow wave descending.

In downstream position of phantom, of Fig. 5-1B, the flow wave sample starts with short damping flow following by a back flow occurs at the beginning of the pulsatile peak wave. The peak flow wave shifts shortly from the flow wave peaks at positions upstream. The peak wave descends gradually to lowest flow rate except the flow wave of peak 10 ml/sec., which descends to constitute a low back flow. The peak flow of wave samples decreases slowly with increasing peak flow rate of the pump, Table 5-1.

On the left Fig. 5-1A, the correspond pressure wave sample for each flow wave sample was acquired at the position upstream, the majority modality in three scaled pressure waves start with the baseline and increased to the peak value during systole and descending gradually to lowest value of pressure near the pressure baseline axis, the wave pressure associated with driving peak flow 10 ml/sec. depicts higher depression in pressure during diastole.

At downstream position, Fig. 5-1B, there are two small crests at the top of the pressure wave separating with short period time, the first crest refers to the systole the second one refers to the starting diastole (decay in pressure). At the same manner, the pressure descended to the baseline pressure, and this is the majority of scaled pressure waves of 20, and 30 ml/sec., peak flow. The pressure wave of 10 ml/sec. peak flow depicts the same modality as at position upstream with a negative depressed pressure at diastole.

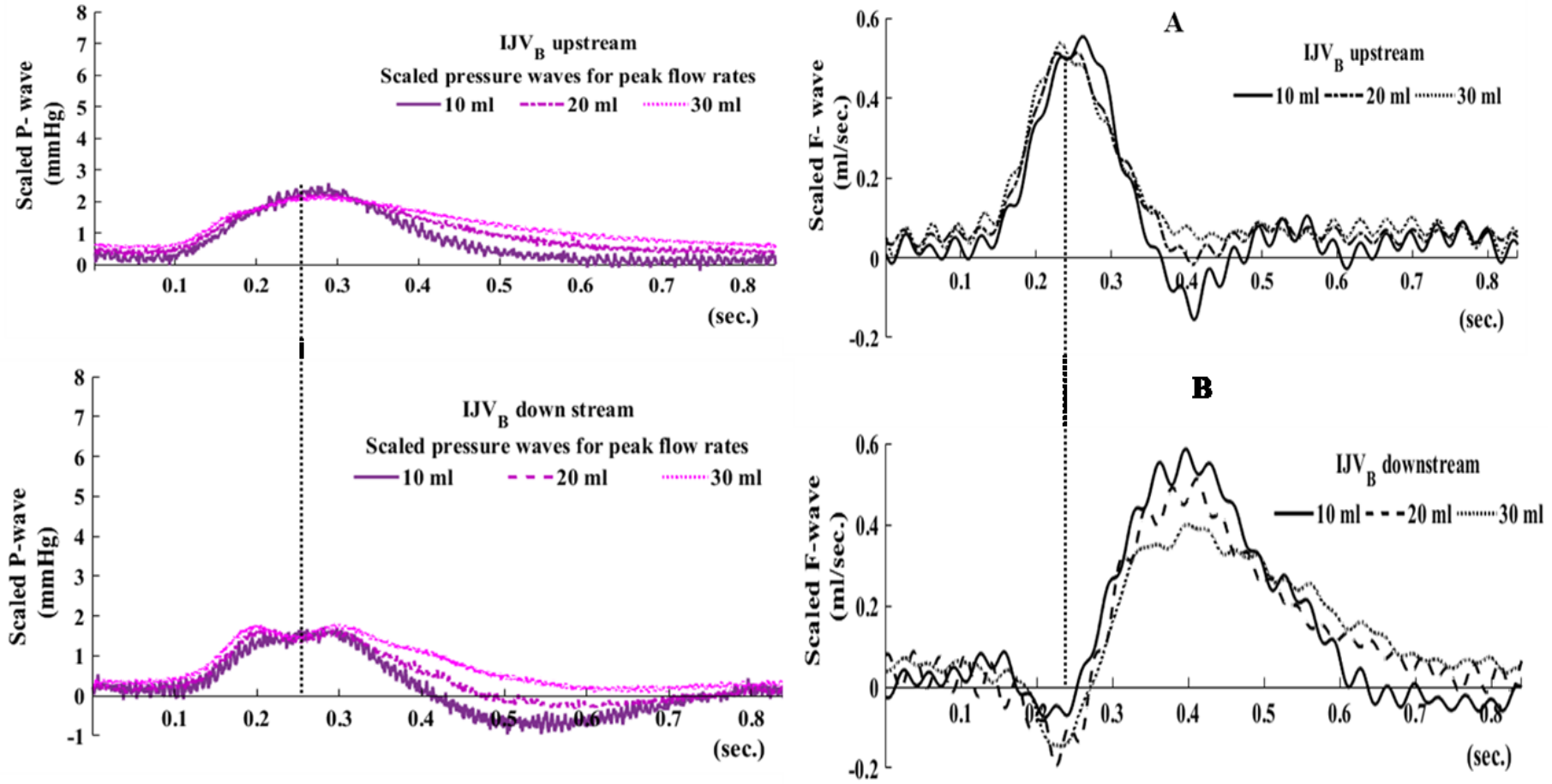

Figure 5-1: Modality of flow and pressure wave in internal jugular vein phantom IJV-B, with no valve builds up. The measurements at positions: upstream (A) and downstream (B) of the phantom. Each position has three waves of flow and pressure corresponding to driving pump peak flow rates 10,20 and 30 ml/sec. The average of flow and pressure waves is scaled to peak flow rate of driving pump. F-wave is average flow wave and P-wave is average pressure wave.

Fig. 5-2, presents the flow average and pressure average waves at recalling positions upstream and downstream with adding the load resistance LRA. To the right Fig. 5-2A, the modality of the average flow depicts the same modality of the wave at upstream in exception the flow wave of peak 10 reveals a very short back flow as compared with other flow waves forms.

In downstream–LRA, the flow wave yields a continuous elevated flow interrupted with the back flow. The sample wave modality at the position loses the pulsatile wave modality, of the implemented carotid2 wave of the pump.

At position upstream-LRA, Fig. 5-2A, the pressure wave of 10 peak flow predicts same modality of the previous position with an elevated start of pressure and slow depressed pressure above the bassline. The other two pressure waves possess small crest and slower depressed pressure during diastole.

At position downstream-LRA, Fig. 2-5B, the wave pressure of 10 peak flow depicts the same modality of upstream-LRA position, while the two other pressure waves possess a small two separated crests and slower depressed pressure elevated up to the baseline.

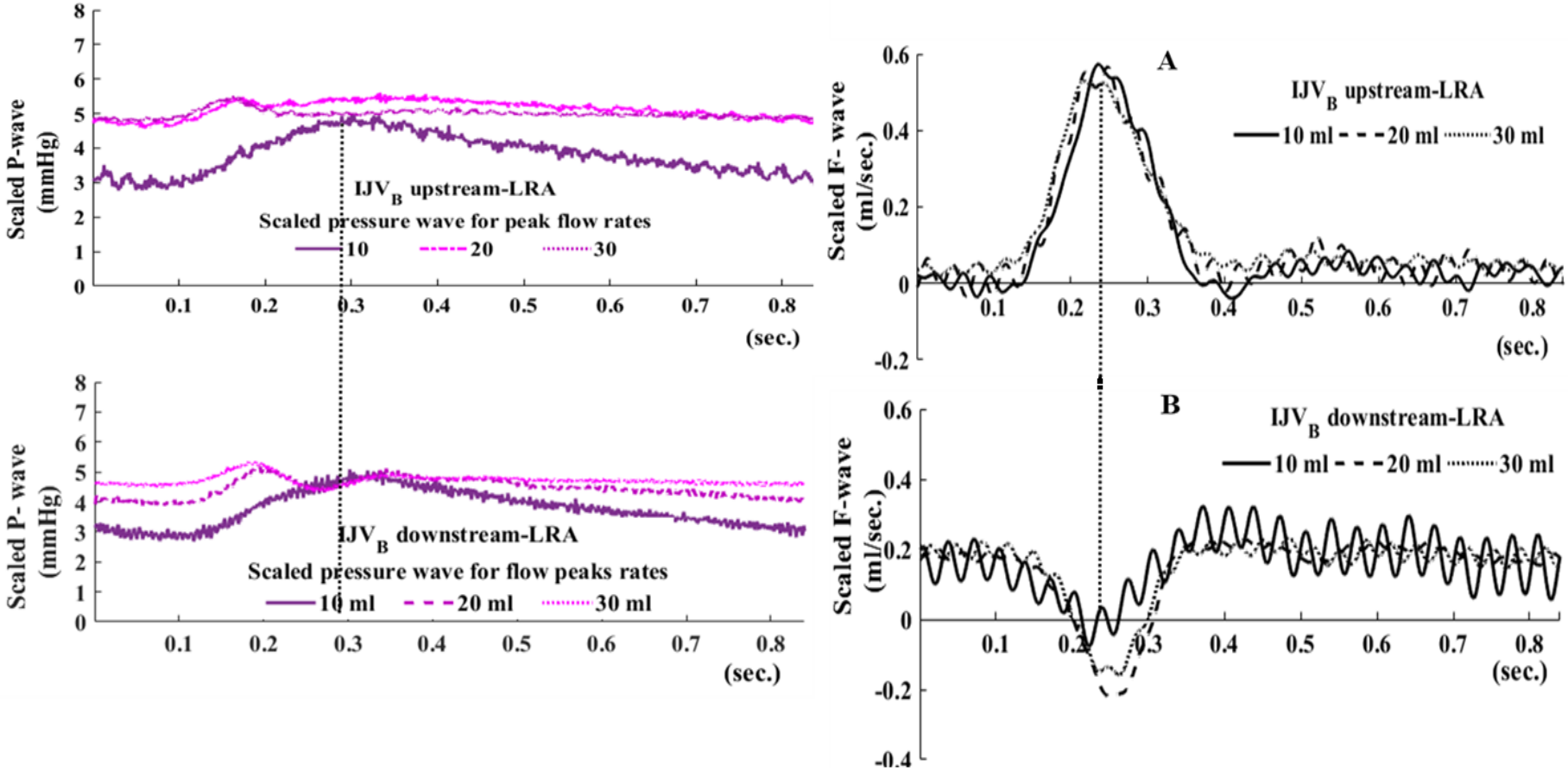

Figure 5-2: Modality of flow and pressure wave in internal jugular vein phantom IJV-B, with no valve build up. The measurements at positions: upstream (A) and downstream (B) of the phantom with adding the load resistance LRA. Each position has three waves of flow and pressure corresponding to driving pump peak flow rates 10,20 and 30 ml/sec. The average of flow and pressure waves is scaled to peak flow rate of driving pump. F-wave is average flow wave and P-wave is average pressure wave.

5.1.2. Mean values of data acquisition in IJV-B:

In table 5-1, the mean value of average pressure wave increases as flow peak rate increases and this is majority for all reading in upstream and downstream positions of phantom IJV-B. However, the pressure mean values yield a lower value at downstream positions in comparing with pressure mean values upstream positions. The slope of mean flow values and pressure mean values represents the change in resistance to flow in the two positions of our measurements, ($R = \frac{\Delta P}{Q}$).

Pressure mmHg	***Mean values***					
Peak flow rates ml/sec.	**IJV_B upstream**			**IJV_B upstream-LRA**		
Pump Peak	**Peak**	**Flow**	**Pressure**	**Peak**	**Flow**	**Pressure**
10	5.54	0.93	7.51	6.40	0.84	38.11
20	10.3	2.39	20.23	10.91	2.32	99.04
30	16.12	3.87	35.99	17.00	3.84	149.73
Slope		9.7			37.3	

Pressure mmHg	***Mean values***					
Peak flow rates ml/sec.	**IJV_B downstream**			**IJV_B downstream-LRA**		
Pump Peak	**Peak**	**Flow**	**Pressure**	**Peak**	**Flow**	**Pressure**
10	5.9	1.30	2.11	3.20	1.60	37.61
20	10.3	2.50	8.48	4.50	2.80	89.01
30	12	4.10	21.35	7.00	4.50	141.64
Slope		6.9			36.2	

Table 5-1: The mean values of flow wave and pressure wave measurements obtained in IJV-B, at positions upstream and downstream without and with LRA corresponding to the measured mean peak flow and driving peak flow rates of the pump.

The slope downstream position of acquisition data changes 28.8% less than the slope upstream position. While the slope at downstream-LRA changes 3% less than the slope at upstream-LRA.

In Table 5-2, The values represent the mean differences between the average pressure upstream and downstream of the phantom without and with LRA corresponding to the mean values of the measured average flow waves. The pressure difference reveals a decrease change in majority at positions with LRA. The reduction percentage relative to pressure difference at positions with LRA as it follows; 90% decrease change at peak 10, 14% decrease change at peak 20, and 44.7% reduction at peak 30.

Difference Pressure ΔP mmHg	***Upstream downstream***		***Upstream-LRA Downstream-LRA***	
Peak flow ml/sec.	**ΔP**	**Q**	**ΔP**	**Q_{LRA}**
10	5.4	1.11	0.50	1.22
20	11.73	2.50	10.03	2.56
30	14.64	3.98	8.09	4.14

Table 5-2: The mean difference of pressure upstream and downstream obtained in IJV-B, without and with LRA corresponding to mean values of average flow wave, Q.

5.2. Internal jugular vein phantom IJVV-B, with valve builds up.

5.2.1. Flow wave and Pressure wave samples in IJVV-B.

In Fig. 5-3A, the average flow and pressure waves in IJVV-B phantom depict the same modality of average flow and pressure waves in IJV-B phantom at position upstream, Fig 5-1A.

In Fig. 5-3B at position downstream, the average flow wave reveals back flow before pulsatile peak wave. This is the majority for the average flow waves at this position, including the wave of peak 10.

The pressure wave modality corresponding to the flow measurement in IJVV-B is compatible to the pressure wave modality at downstream in IJV-B, Fig. 5-1B.

In Fig.5-4A, at position upstream-LRA, along similar lines the average flow modality reveals the same modality of average flow wave using IJV-B phantom, Fig. 5-2A, in exception to: the marked back flow with average flow wave of peak 10, and a notable second small crest before the damping flow.

Fig. 5-4B, shows an elevated starting of flow followed by a back flow of amplitude (0.35 ml/sec.) occurs before pulsatile peak wave. The flow wave is not damping to the flow baseline at end of the cycle.

The pressure wave at upstream and downstream with the load resistance LRA, reveals an elevated pressure at the beginning of the wave which keeps constant to the end. This finding is majority for the pressure measurements with existence of the LRA.

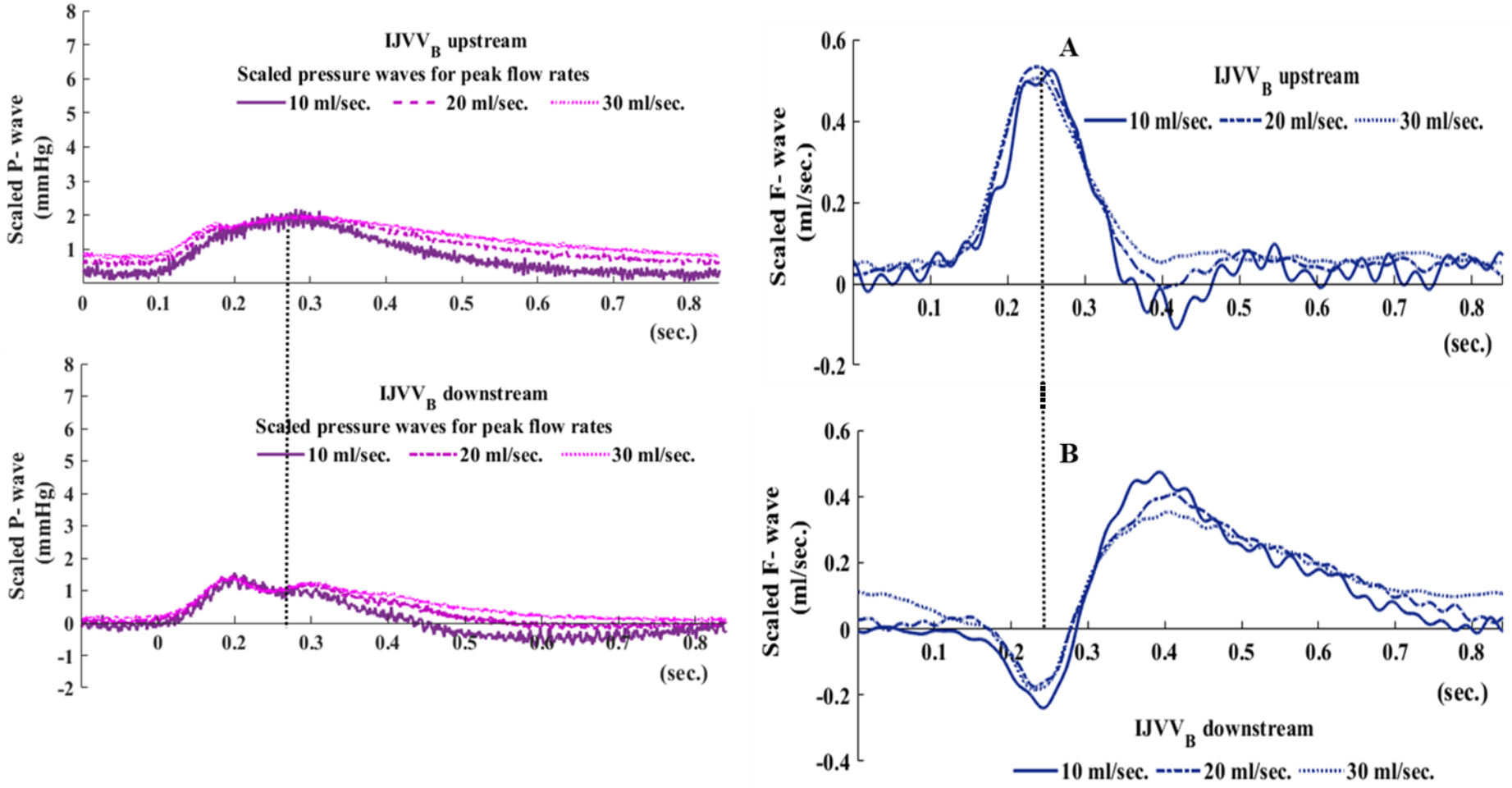

Figure 5-3: Modality of flow and pressure wave in internal jugular vein phantom IJVV-B with valve builds up. The measurements at positions: upstream (A) and downstream (B) of the phantom. Each position has three waves of flow and pressure corresponding to driving pump peak flow rates 10,20 and 30 ml/sec. The average of flow and pressure waves is scaled to peak flow rate of driving pump. F-wave is average flow wave and P-wave is average pressure wave.

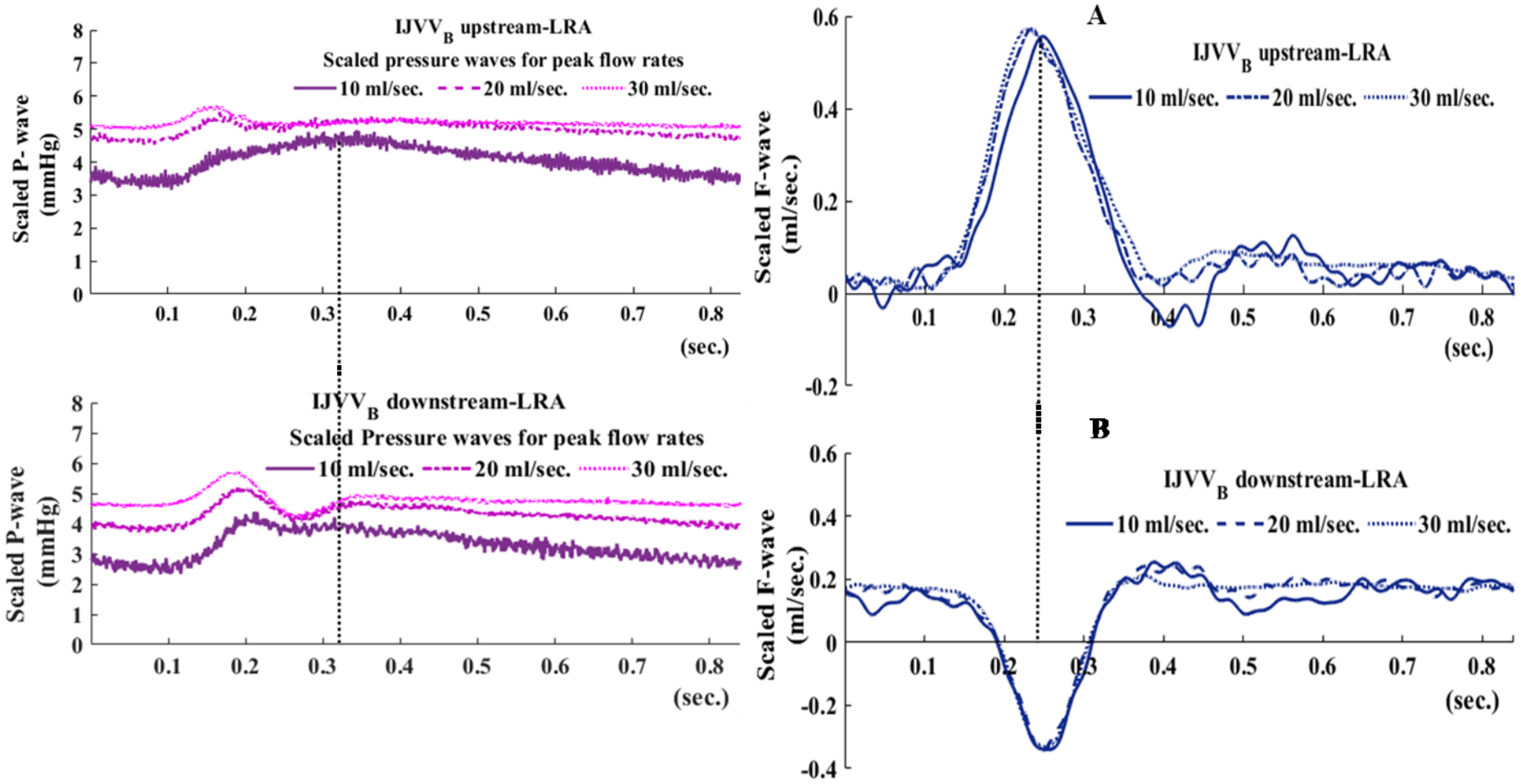

Figure 5-4: Modality of flow and pressure wave in internal jugular vein phantom IJVV-B, with valve builds up. The measurements at positions: upstream (A) and downstream (B) of the phantom with adding the load resistance LRA. Each position has three waves of flow and pressure corresponding to driving pump peak flow rates 10,20 and 30 ml/sec. The average of flow and pressure waves is scaled to peak flow rate of driving pump. F-wave is average flow wave and P-wave is average pressure wave.

5.2.2. Mean values of data acquisition in IJVV-B:

The mean values of average flow and pressure waves are presented in Table 5-3. The change in resistance to flow (R) is identified by the slope of mean flow values and pressure mean values at positions upstream and downstream without and with load resistance, LRA. The slope at position downstream declines 55% of the slope at upstream position. While the slope at downstream-LRA is higher by 8.2% than the slope at position upstream-LRA.

Pressure mmHg	**Mean values**					
Peak flow rates ml/sec.	**IJVV-B upstream**			**IJVV-B upstream-LRA**		
Pump Peak	**Peak**	**Flow**	**Pressure**	**Peak**	**Flow**	**Pressure**
10	5.25	0.89	8.16	5.56	1.10	40.40
20	10.66	2.24	22.88	11.46	2.33	99.92
30	15.15	3.80	39.21	17.14	3.97	155.56
Slope		10.7			39.8	

Pressure mmHg	**Mean values**					
Peak flow rates ml/sec.	**IJVV-B downstream**			**IJVV-B downstream-LRA**		
Pump Peak	**Peak**	**Flow**	**Pressure**	**Peak**	**Flow**	**Pressure**
10	4.70	1.05	0.95	2.50	1.00	32.66
20	8.10	2.50	7.26	4.87	2.40	85.80
30	10.6	4.10	15.49	6.35	3.55	143.02
Slope		4.8			43.1	

Table 5-3: The mean values of flow wave and pressure wave measurements obtained in IJVV-B, phantom with valve, at positions upstream and downstream without and with LRA. The measurements correspond to measured mean peak flow and driving peak flow of the pump.

In Table 5-4, The values represent the mean differences between the average pressure upstream and downstream of the IJVV-B without LRA and with LRA corresponding to the mean values of the measured average flow waves. The pressure difference reveals mostly a decrease change at positions with LRA. The change percentage relative to pressure difference at positions with LRA as it follows; 9.6% decrease change at peak 20, 47.1% decrease change at peak30, and 7.3% increased at peak10.

IJVV-B ***Difference Pressure ΔP mmHg***	***Upstream downstream***		***Upstream-LRA Downstream-LRA***	
Peak flow ml/sec.	**ΔP**	**Q**	**ΔP**	**Q_{LRA}**
10	7.21	0.97	7.74	1.05
20	15.62	2.37	14.12	2.365
30	23.72	3.95	12.54	3.76

Table 5-4: The mean difference of pressure upstream and downstream obtained in IJVV-B, without and with LRA corresponding to mean values of flow wave, Q.

The (ΔP-Q) curve in Fig. 5-5, shows the impact of the driving pressure, (pressure difference) between the upstream and downstream of the phantoms with the corresponding mean flow Q. The driving pressure is increased mostly in IJVV-B phantom as compared with IJV-B.

In Fig. 5-6, shows the (ΔP-Q) curve with adding LRA downstream at the terminal loop. The IJVV-B shows higher pressure difference and mostly the pressure difference is decrease with increasing Q.

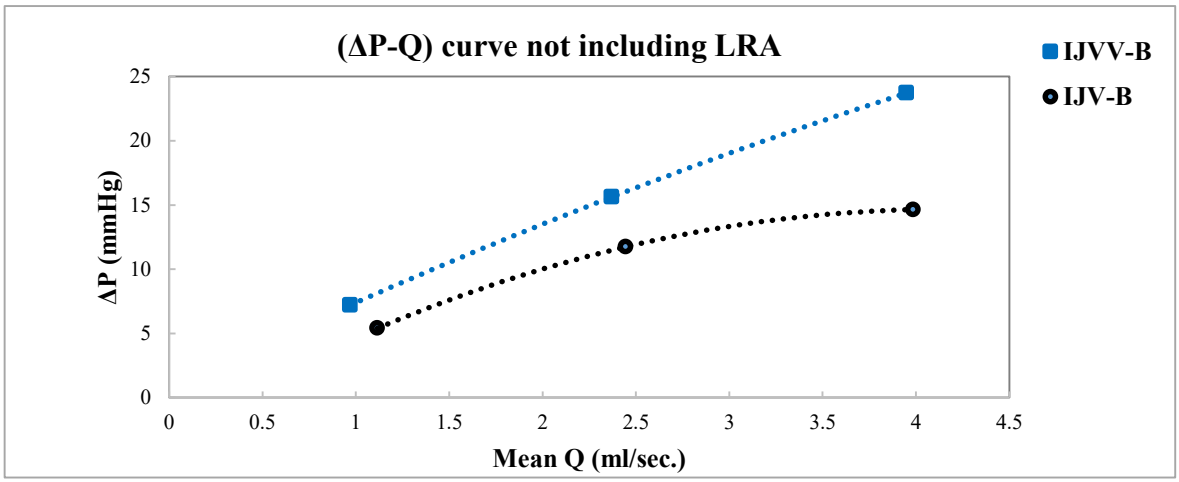

Fig. 5-5: The driving pressure in IJV-B and IJVV-B. (difference pressure ΔP between upstream and downstream positions) corresponding to the mean value of flow rate Q. The measurements not including LRA downstream of the loop.

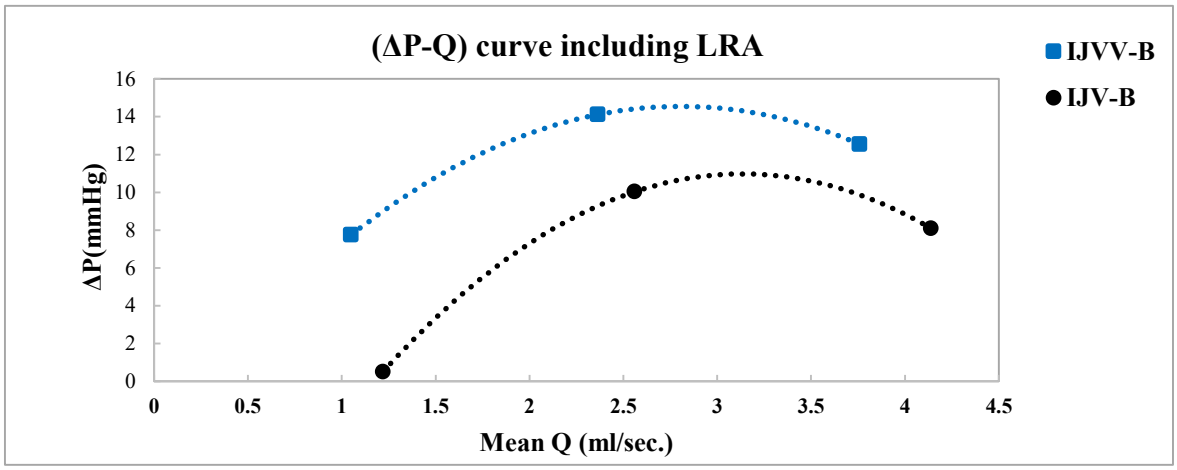

Fig. 5-6: The driving pressure in IJV-B and IJVV-B. (difference pressure ΔP between upstream and downstream positions) corresponding to the mean value of flow rate Q. The measurements including LRA downstream of the loop.

5.3. Internal Jugular vein phantom IJVV-R, with valve builds up:

The measurements were acquired using the phantom IJVV-R, which has the same design of phantom IJVV-B, but built with different material. In this study, the question under debate if whether the different material can change the modality of the flow and pressure wave.

The available evidence seems to suggest that the two materials used in phantoms build yield mostly a similar modality for both the flow and pressure wave. According to that, the curves regarding the modalities of flow and pressure waves obtained in IJVV-R is attached in the Appendix for predication.

Chapter 6

Discussion and Conclusions

6.1. Leaflets motion and Doppler velocity in phasing:

To enhance the evaluation of IJV valve competence or incompetence, limited studies involved IJV valve M mode trace to investigate the behavior trend of the leaflets, the opening and closing cycles (Brownlow and McKinney, 1985; Menegatti *et al.*, 2014; Menegatti *et al.*, 2017).

In this study and for the first time, we interpolated the Doppler velocity in section J1, Where the valve located, to the leaflet time motion in M mode by constructed a new velocity data in same range of an original data. We demonstrated a concurrent ultrasound imaging traces between IJV valve M mode motion and Doppler velocity in phase to the ECG recording.

The results yield a consensus in view that the valve leaflet is mobile and it is heart cycle dependent. Which is in agree with previous studies (Hu and Chung, 2008; Stolz, 2012). We explain this feature as it follows: The valve exhibits four dynamic phases regarding jugular vein pulse JPV wave; the early opening, leaflets diverge parallel to close wall, occurs at T wave of ECG. This phase can be linked with x' descent of jugular pulsed pressure JVP wave, which reflects the descent in right atria pressure during final phase of ventricular systole. This phase associated with early s' wave of IJV Doppler velocity trace taking place at end of T wave.

The second phase includes the partial closure of the valve in respond to the ascending v' wave of JVP next to T wave, caused by the passive increase in pressure and volume of the right atrium as it fills in late systole and early diastole.

The third phase considers the partial opening valve at mid diastole associating with the descending y' wave, when the tricuspid valve open and starting the filling passive of right ventricle. The forth dynamic valve phase presents the valve closure caused by atrial contraction, an ascending a' wave in JVP. The last phase associates with a second smaller peak d' of Doppler velocity. In 70% of our samples we noticed back flow in Doppler velocity at end of P wave as a result of atrial contraction. Our finding is matching the old interesting study by (Kalmanson *et al.*, 1972). In which, it had been interpreted the Doppler velocity pattern in relation to the change in JVP and ECG recording.

6.2. Open time and closure time of IJV valve (OSDT):

We demonstrated a mathematical analysis method to estimate the total open time of IJV valve. This method depends upon the change in area under the separation distance ratio SDR curve as it is shown in Figs. 3-1,3-2, 3-3. The open time includes all dynamic valve cycles constituting in cardiac cycle. The **OSDT** formed 70% of cardiac cycle while the closure time **CSDT** formed 30% in normal young subjects. The results are associating with mean separation distance of the valve equals to 45% of total leaflet separation. In this study, the mean Doppler velocity at J1 equals to 58.5 cm/sec.

6.3. Logical test of 0.5 threshold:

This method based on collecting data where the data $\mathbf{OSDF_{\geq 0.5}}$ positioned at threshold 0.5 or over is considered open time of valve, else is considered closure time. On the evidence currently available, logical test 0.5 threshold supports the hypothesis of method1 to deducing the total open time **OSDT** through a strong correlation we got in this part of study. Hence, we got the same supporting from the logical test of closure data $\mathbf{OCSDF}_{<0.5}$ as a result of a strong correlation with **CSDT** of method1. In sequence, we got a very good compatible trends of **OSDT** and $\mathbf{OSDF_{\geq 0.5}}$.

As we present this conclusion in Fig. 3-5, it could be argued that the separation fraction of the leaflet data, between a maximum separation threshold (equal 1) to lowest threshold (equal 0), distributes most frequently around threshold 0.5 in its opening and closing cycles. This finding leads to encourage the debate on leaflet mobile movement in normal Jugular valve.

6.4. Logical test of 0.75 and 0.25 thresholds:

The hypothesis of threshold 0.75 concerning open fraction time $\mathbf{OSDF_{\geq 0.75}}$ shows a mediate correlation with **OSDT**, Fig. 3-8. This can be interpreted as; the probability of leaflet separation fraction is less distributed in threshold 0.75 as compared with threshold 0.5 and it forms 51% of total data, this can be seen in Fig. 3-5. It seems the data in threshold 0.75, is the only data has a normal distribution in normal young subjects, with no normality finding in other data.

In threshold 0.25 concerning a closure cycle phase, the data **CSDF$_{<0.25}$** constitute 5% of total separation distance data. Since, the 0.25 threshold hypothesis including a distributed data between (less than 0.25 and 0), it gets a normal finding by the mediate positive correlation with **CSDT**.

The **CSDF$_{<0.25}$** findings settle at end of diastole as we present that in sample survey of Fig. 3-5. This finding support to the claim that the Jugular valve normally closed at end of diastole after P wave.

Concerning the results including partial opening (or partial closure) between the thresholds 0.75 and 0.25, the thresholds included, yield a weak correlation with method1, Fig. 3-10, and 4-11.

However, we got a good inverted compatible trends between OSDT and $PSDF_{0.75-0.25}$ as it presents in Fig. 3-4. This can be interpreted according to Fig. 3-5; it is evidence that the distribution data between thresholds 0.75 and 0.25, the white colored area, decreased if the total area under the curve increased, increases open time.

6.5. The experimental flow wave modality of IJV.

It was known previously, that the pulsatile wave varied due to the nature of arterial and venous flow. The modality of volumetric flow can be changes between two locations with the same total volumetric flow, the conservation of mass. Since the IJV is a much flexible and plasticity vein, the larger influence of the cerebral outflow is related to change in flow pattern between the upstream and downstream positions of the internal jugular veins. Hence, the venous flow in the upstream position is more typical during the cardiac cycle compared with the downstream position, Figs. 5-1A and 5-1B.

In this experimental model the position at upstream of IJV phantom should represent the cerebral out flow at skull base to minimize the influences of the compliance and collapsibility of the vein. Our finding is in agree with the findings by (Tain, Ertl-Wagner and Alperin, 2009).

At downstream position of IJV-B, Fig 5-B1, the back flow takes place at the beginning of the pulsatile flow wave, named jugular vein reflux JVR. This could be interpreted as follows:

The rule of IJV compliance is that the elastic recoil force created by stretching the walls of IJV creates a potential force that can drive flow when the downstream pressure is lower, in another word, the walls of vessels must be able to stretch in order to transiently take up the volume. The pressure created by the stretch of vascular walls moves the volume on to the next vascular segment with a lower pressure, Fig. 6-1, (Anwar *et al.*, 2012; Magder, 2016).

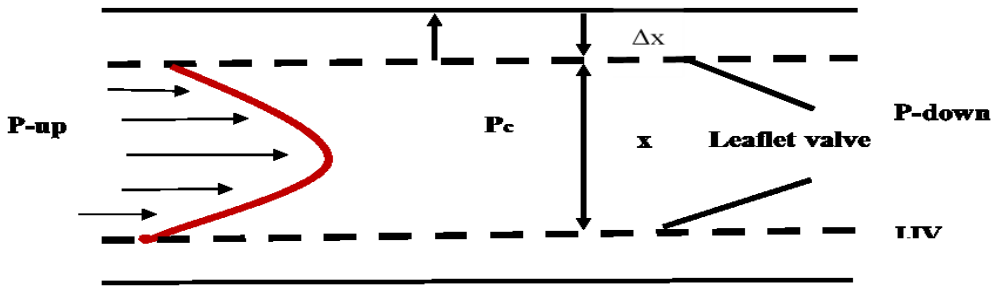

Fig. 6-1: The flow stretches the wall vessel to Δx during systole and elastic recall force acting on wall during diastole. The driving flow is proportional to pressure difference up and down affecting on a point Pc located inside the vein.

The back flow occurs once the blood enters the vessel with its relative velocity resulting an increase shift pressure towards upstream according to Venturi equation, increased velocity depresses the pressure. However, in venous segments without existing venous valve (e.g. the distal IJV and intracerebral veins), just a reversed pressure gradient could produce venous reflux. Therefore, the existence of an incompetent venous valve is not always necessary for venous reflux (JVR), (Hu and Chung, 2008).

In Doppler US study, it had demonstrated that the JVR occurs even in competent valves, a Valsalva maneuver leads to a short reflux during valve closure. This physiological reflux, with a duration corresponding to the valve closing time, has to be differentiated from an ongoing back flow component in insufficient valves (Nedelmann, Eicke and Dieterich, 2005; Stolz, 2012).

In this study we added the load resistance at the terminal loop to represent a pathologic state close to right heart such as increased intrathoracic pressure or brachiocephalic vein obstruction (Yan and Seow, 2009).

12345

The JVR at downstream position with no LRA reveals no significant difference as we compare the average flow wave between IJV-B and IJVV-B.

At position downstream-RLA, using IJV-B, the JVR is 4% less than the JVR using IJVV-B. Thus this could be explained when there is an increased shift pressure towards up of JV, the valve keeps close until the shift pressure changes towards the downstream.

6.6. The Pressure – Flow relationship of upstream and downstream in IJV.

In analog to Ohm's law, the current (I) equals the voltage difference (ΔV) divided by resistance (R). In relating Ohm's Law to fluid flow, the voltage difference is the pressure difference (ΔP or driving pressure, or pressure gradient), the resistance is the resistance to flow (R) offered by the blood vessel and its interactions with the flowing blood. Hence, the driving pressure ΔP between upstream and downstream of IJV and at the same time the transmural pressure on the IJV wall can both affected on the cerebral flow out pathway (Low and Chew, 1991).

We demonstrated the relationship between the driving pressure ΔP and mean flow rate Q, Fig.5-5. To explain the results, we should recall that the change in flow rates within three driving flow peaks, can change the pressure around all the loop. In sequence we can explain the variation in driving pressure at some point in IJV such as P_c between our two positions of measurements, $P_{up} > P_c > P_{down}$, Fig. 6-1.

The data appears to suggest that, the driving pressure, is low when the Q is low, this indicates also that the transmural pressure is low, (P_c is close to atmospheric pressure P_e). When Q is increased, the ΔP increases also and the transmural pressure is positive. At higher Q, the ΔP depresses indicating high positive transmural pressure. This results is in agree with the finding by (Katz, Chen and Moreno, 1969). The curve of IJVV-B yields a higher driving pressure than IJV-B with no valve builds up.

In Fig. 5-6, the ΔP-Q curve shows an increases in ΔP, since the existence of LRA increases the pressure inside the IJV. In this study we found that the driving pressure drops across the collapsible tube with higher flow rate.

Because the driving pressure depends not only on the resistance of the collapsing tube itself but also on the flow through it (Katz, Chen and Moreno, 1969).

6.7. The pressure wave at upstream and downstream with LRA.

The heart pumps the blood volume to arterial compartment and creates an arterial pressure Pa which is depending upon total vascular resistance. In analog, the pump shifts the BMF through the loop with a specific pressure.

In this study we found an elevated pressure which kept mostly constant during the whole cycle. This finding is associated with LRA. We can explain the elevation in pressure by the application of Ohm's law. The total resistance of our loop, Fig. 4-1, can be calculated as follows:

$$P_a - P_{RA} = Q_T \ \frac{(R1.R2)}{R1+R2}$$

Where R_1 the equivalent resistance of the right branch including IJV, while R_2 is the left branch resistance (CR-GG). Pa is the pressure provided by the pump, the end point of our loop presents the right atrial P_{RA} (entering the pump).

Then we can express the Pa with the next equation by assuming P_{RA} is low:

$$Pa = (Q_T \frac{R1.R2}{R1+R2}) \qquad 1\ldots\ldots\ldots\ldots\ldots$$

Where Q_T is total flow and it is equal to flow in and flow out (conservation of mass):

$$QT = Q_{in} = Q_{out}$$

When we added the load resistance LRA, the calculations for the pressure drop will be as follow:

$$P^l{}_a - P^l{}_{RA} = Q_T \frac{(R1.R2)}{R1+R2} + Q_T.\ LRA$$

Where $P^l{}_a$ is the pressure provided by the pump and $P^l{}_{RA}$ is the right heart pressure, with adding LRA.

Then the P^{l}_{a} will be equal to:

$$P^{l}_{a} = Q_T \frac{(R1.R2)}{R1+R2} + Q_{T.}\, LRA + P^{l}_{RA}$$

By sequence P^{l}_{a} can be write as:

$$P^{l}_{a} = (Pa - P_{RA}) + Q_{T.}\, LRA + P^{l}_{RA}$$

Since $P_{RA} = P^{l}_{RA}$

2…… $P^{l}_{a} = Pa + Q_{T.}\, LRA$

These results provide us with confirmatory evidence that the elevated pressure wave at positions with LRA, is a result of the pressure equals to (Q_T. LRA) added to the main pressure of the pump *Pa.*

6.8. Conclusions and recommendations:

1. Put the leaflets position in phase with Doppler velocity trace synchronized with ECG shared an important premise in diagnostic for both valve leaflet motion associated with IJV velocity prior to the valve. Since there is a growing in arguments concentrated on valve leaflet motion rather than its competent, being this aspect complex and various, and probably the real index of valve function (Morimoto *et al.*, 2009; Valecchi *et al.*, 2010; Simka *et al.*, 2013).
2. The mobile valve is one of the most important feature in normal mechanism valve, otherwise the immobile valve mechanisms causing a significant delay of jugular flow in course of chronic cerebrospinal venous insufficiency (CCSVI) as it showed by (Zamboni *et al.*, 2015).
3. The lack in physiologic knowledge regarding the mechanism of valve opening and closing as well the normal open time, can be overcome in this study by post imaging analysis as a premise for further studies in the field of neurodegeneration.
4. Further progress related to this work, is to examine the methods on old subjects or subjects with impaired cerebral out flow.

5. A compatible study between JVP and IJV valve motion is suggested to put forward a new physiologic concept to the valve mechanical motion.
6. The hydraulic experimental model leads to a basic understand for the flow out pathway through IJV. Our finding reveals that the back flow is a normal finding at downstream position of IJV. It is associated with or without the existence of the valve.
7. The flow affects the driving pressure between two points of measurements along the vein. Our study shows an increase driving pressure in IJVV-B phantom more than IJV-B. This puts forward the view that the valve can adjust the driving pressure through its dynamic cycle.

Acknowledgment

The success and final outcome of this project required a lot of guidance and assistance from many people and I am extremely privileged to have got this all along the completion of my project. All that I have done is only due to such supervision and assistance and I would not forget to thank them.

I would first like to thank my advisor, Prof. Mauro Gambaccini who guided me in selecting the final theme for this research. His recommendations and instructions have enabled me to assemble and finish the dissertation effectively.

I extremely respect and thank my co-advisor Prof. Tamie Poepping for providing me an opportunity to do the project work in [Western University] and giving me all support and guidance which made me complete the experiment work duly.

I owe my deep gratitude to our coordinator Prof. Vincenzo Guidi, for his guidance and recommendation within the period time of study.

I am thankful to Dr. Giovanni Di Domenico and Dr. Francesco Sisini for providing me with a scientific analysis guidance.

With a special mention to my colleague Dr. Adriano Contillo for his feedback, cooperation and of course friendship.

I have had the pleasure to work with Prof. Zamboni group in Cona hospital/Ferrara, for the providing me the opportunity to work and got my data.

I would like to thank my close friends for accepting nothing less than excellence from me. Last but not the least, I would like to thank my family: my mother, brother Faisal and sisters Asmaa and Bushra for supporting me spiritually throughout writing this thesis and my life in general, God bless them all.

Appendix:

The appendix includes the modalities curves obtained in IJVV-R phantom. Fig. 1, presents the modality of flow and pressure waves in IJVV-R at upstream and downstream positions.

Fig. 2, presents the modality of flow and pressure at upstream and downstream positions with adding the load resistance LRA.

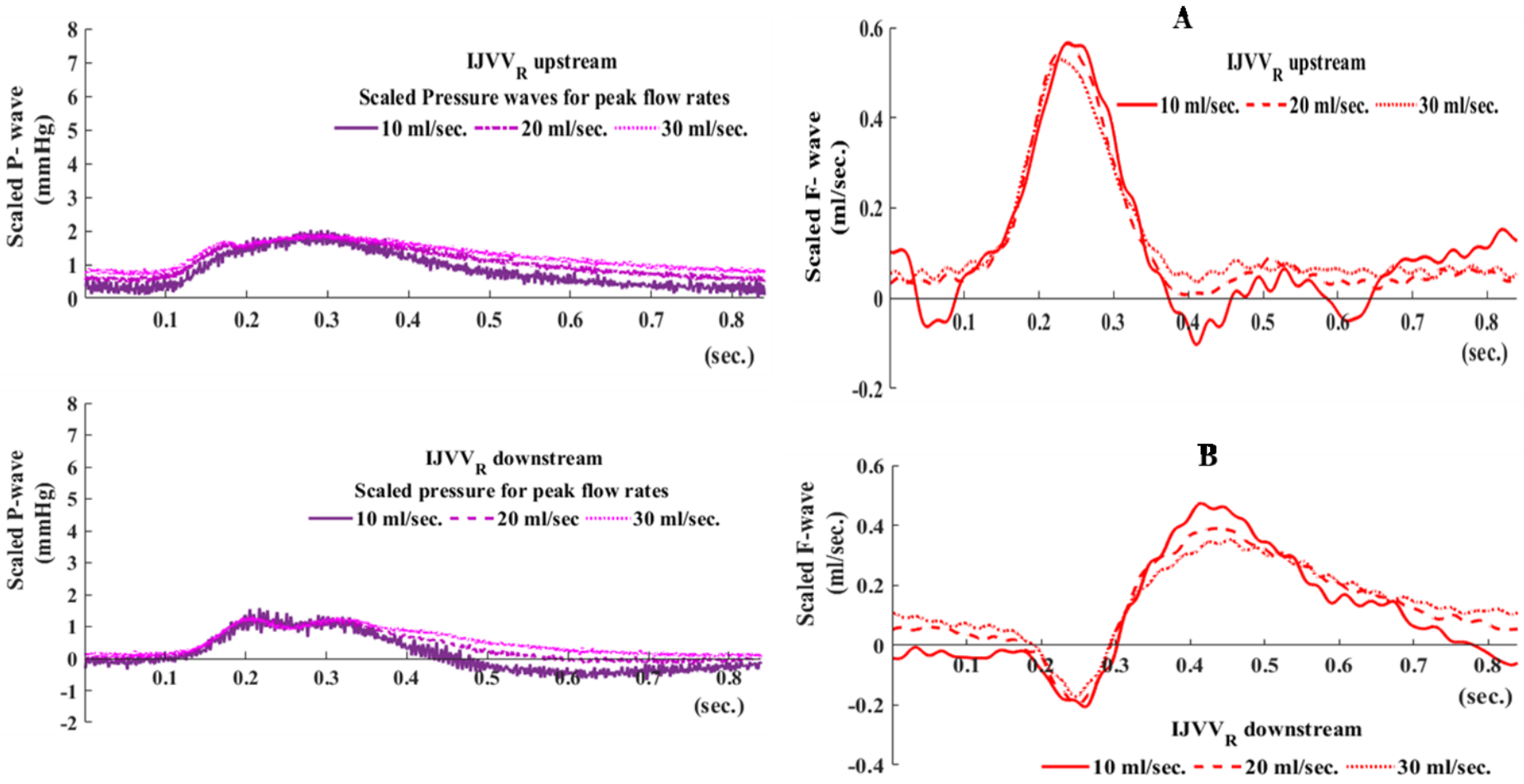

Fig.1: Modality of flow and pressure wave in internal jugular vein phantom IJVV-R with valve builds up. The measurements at positions: upstream (A) and downstream (B) of the phantom. Each position has three waves of flow and pressure corresponding to driving pump peak flow rates 10,20 and 30 ml/sec. The average of flow and pressure waves is scaled to peak flow rate of driving pump. F-wave is average flow wave and P-wave is average pressure wave.

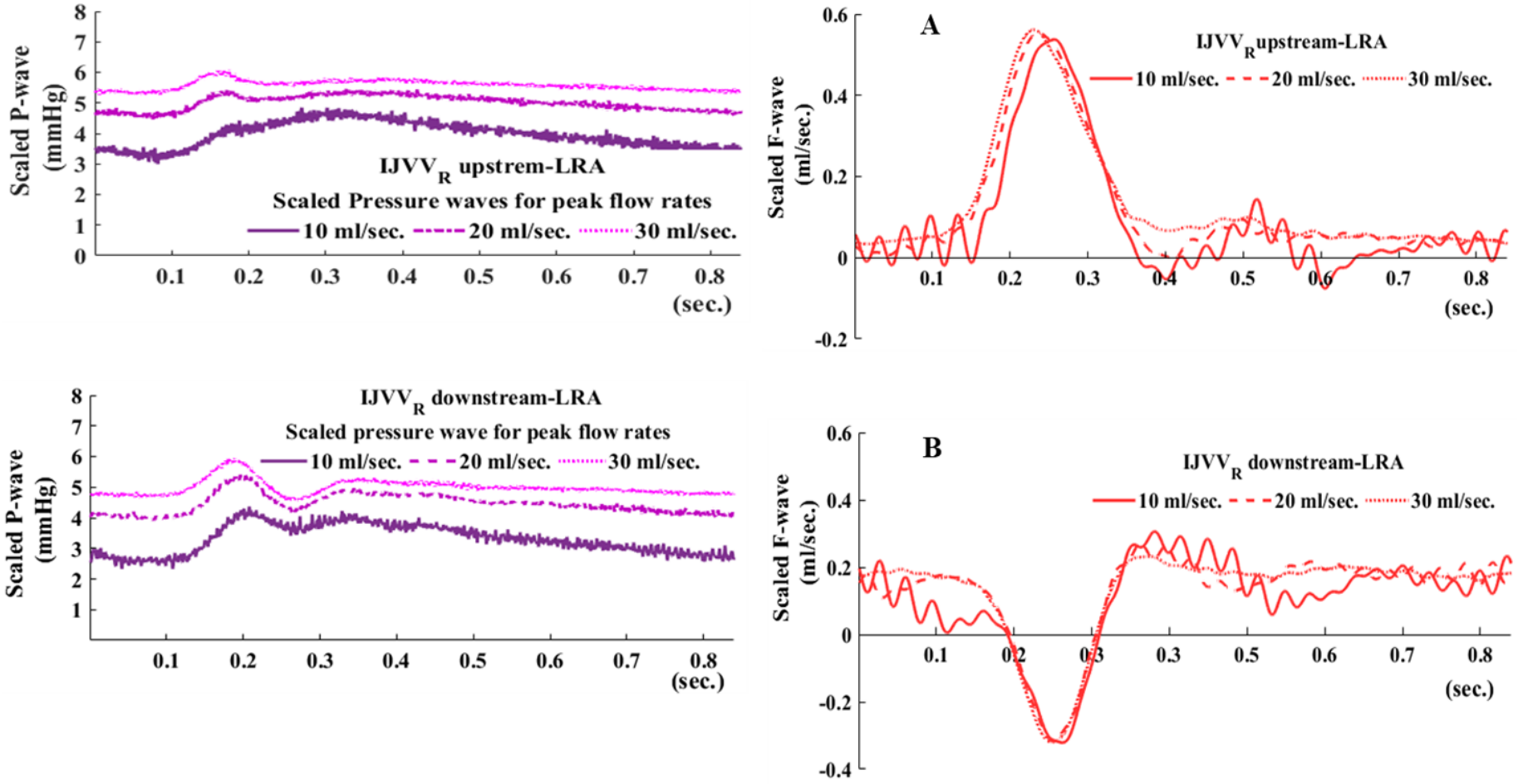

Fig. 2: Modality of flow and pressure wave in internal jugular vein phantom IJVV-R with valve builds up. The measurements at positions: upstream (A) and downstream (B) of the phantom with adding load resistance LRA. Each position has three waves of flow and pressure corresponding to driving pump peak flow rates 10,20 and 30 ml/sec. The average of flow and pressure waves is scaled to peak flow rate of driving pump. F-wave is average flow wave and P-wave is average pressure wave.

References:

1) Aayeesha Ali (2012) *TeachMePhysiology:Venous Return - Central Venous Pressure - TeachMePhysiology*.
2) Aleksandr Rovner (2015) *The principle of ultrasound - Physics of ultrasound as it relates to echocardiography*.
3) Ankur Gupta (2015) *Jugular venous pressure*.
4) Anwar, M. A., Shalhoub, J., Lim, C. S., Gohel, M. S. and Davies, A. H. (2012) 'The effect of pressure-induced mechanical stretch on vascular wall differential gene expression.', *Journal of vascular research*. Karger Publishers, 49(6), pp. 463–78.
5) Applefeld, M. M. (1990) *The Jugular Venous Pressure and Pulse Contour*, *Clinical Methods: The History, Physical, and Laboratory Examinations*. Butterworths.
6) Aziz, N., Simonetta, G. and Forrester, K. (2006) 'Recent Developments In Data Recording System For Physiology', *Pak J Physiol*, 2(1).
7) Barbeito, A. and Mark, J. B. (2006) 'Arterial and central venous pressure monitoring.', *Anesthesiology clinics*, 24(4), pp. 717–35.
8) BestanJacob (2012) *Radiography:Basic Ultrasound Physics*.
9) Boote, E. J. (2003) 'AAPM/RSNA Physics Tutorial for Residents: Topics in US', *RadioGraphics*. Radiological Society of North America, 23(5), pp. 1315–1327.
10) Broilo, F., Meregalli, A. and Friedman, G. (2015) 'Right internal jugular vein distensibility appears to be a surrogate marker for inferior vena cava vein distensibility for evaluating fluid responsiveness.', *Revista Brasileira de terapia intensiva*. Associação de Medicina Intensiva Brasileira, 27(3), pp. 205–11.
11) Brownlow, R. L. and McKinney, W. M. (1985) 'Ultrasonic evaluation of jugular venous valve competence.', *Journal of Ultrasound in Medicine*, 4(4), pp. 169–172.
12) Carerj, S., Micari, A., Trono, A., Giordano, G., Cerrito, M., Zito, C., Luzza, F., Coglitore, S., Arrigo, F. and Oreto, G. (2003) 'Anatomical M-Mode: An Old-New Technique', *Echocardiography*. Blackwell Science Inc, 20(4), pp. 357–361.
13) Catanho, M., Sinha, M., Vijayan, V. and Sinha, V. (2012) 'Mathematical Methods in Bioengineering Model of Aortic Blood Flow Using the Windkessel Effect'.
14) Christian Wolff (2008) *Radar Basics - PRF and PRT*. Available at: http://www.radartutorial.eu/01.basics/Pulse Repetition Frequency %28PRF%29.en.html.

15) Chua Chiaco, J. M. S., Parikh, N. I. and Fergusson, D. J. (2013) 'The jugular venous pressure revisited.', *Cleveland Clinic journal of medicine*. NIH Public Access, 80(10), pp. 638–44.
16) Cipolla, M. J. (2009) 'Regulation of Cerebrovascular Tone'. Morgan & Claypool Life Sciences.
17) Ciuti, G., Righi, D., Forzoni, L., Fabbri, A. and Pignone, A. M. (2013) 'Differences between Internal Jugular Vein and Vertebral Vein Flow Examined in Real Time with the Use of Multigate Ultrasound Color Doppler', *American Journal of Neuroradiology*, 34(10), pp. 2000–2004.
18) Colin Deane, Kypros Nicolaides, Giuseppe Rizzo, K. H. and R. X. (2002) *Doppler in Obstetrics: Doppler ultrasound: principles and practice*.
19) Craig Sisson, MD and Arun Nagdev, M. (2007) *Focus On: Ultrasound-Guided Central Venous Access of the Internal Jugular Vein // ACEP*.
20) Creigen, V., Ferracina, L., Hlod, A., van Mourik, S. (2007) *Modeling a heart pump*.
21) D. Lepori1, P. Capasso1, D. Fournier1, C.Y. Genton2 and P. Schnyder1 (1999) 'High-resolution ultrasound evaluation of internal jugular venous valves', *Eur. Radiol.*, 9, pp. 1222–1226.
22) Deepak, C. A., Sarvadnya, J. J. and Sabitha, K. S. (2015) 'Variant anatomy of internal jugular vein branching.', *Annals of maxillofacial surgery*. Wolters Kluwer -- Medknow Publications, 5(2), pp. 284–6.
23) Doepp, F., Schreiber, S. J., von Münster, T., Rademacher, J., Klingebiel, R. and Valdueza, J. M. (2004) 'How does the blood leave the brain? A systematic ultrasound analysis of cerebral venous drainage patterns', *Neuroradiology*. Springer-Verlag, 46(7), pp. 565–570.
24) Doepp, F., Valdueza, J. and Schreiber, S. (2008) 'Incompetence of internal jugular valve in patients with primary exertional headache: a risk factor?', *Cephalalgia*, 28(2).
25) Drazner et al. (2001) 'Prognostic Importance of Elevated Jugular Venous Pressure and a Third Heart Sound in Patients with Heart Fauilar', *New England Journal of Medicine*, 345(26), pp. 1912–1913.
26) Dresser, L. P. and McKinney, W. M. (1987) 'Anatomic and pathophysiologic studies of the human internal jugular valve', *The American Journal of Surgery*. Elsevier, 154(2), pp. 220–224.
27) Feigenbaum, H. (2010) 'Role of M-mode technique in today's echocardiography.', *Journal of the American Society of Echocardiography : official publication of the*

American Society of Echocardiography. Elsevier, 23(3), pp. 240-57–7.

28) Frank Padberg, Carman, T. (2016) *Chapter1 Normal venous circulation*. doi: Provided by the American Venous Forum: veinforum.org.

29) Fukazawa, K., Aguina, L. and Pretto, E. A. (2010) 'Internal Jugular Valve and Central Catheter Placement', *Anesthesiology*. The American Society of Anesthesiologists, 112(4), p. 979.

30) Furukawa (2012) 'Morphological Variations of the Internal Jugular Venous Valve', *Anat Physiol*, 2(4).

31) G. Saddik (2015) 'Ultrasound imaging system', *USLA*.

32) Garg, N. and Garg, N. (2000) 'Jugular Venous Pulse : An Appraisal', *Indian Academy of Clinical Medicine*, 1(3).

33) Giuliodori, M. J., Lujan, H. L., Briggs, W. S., Palani, G. and Dicarlo, S. E. (2009) 'How We Teach Hooke's law: applications of a recurring principle', *Adv Physiol Educ*, 33, pp. 293–296.

34) Gramiak, by R., St Louis, W. R. and Mosby, C. V (1978) 'Transcutaneous Doppler Jugular Venous Flow Velocity Recording Clinical and Thermodynamic Correlates', *Circulation*, 57(5).

35) Gray (2015) *The Veins of the Neck - Human Anatomy*. Available at: https://theodora.com/anatomy/the_veins_of_the_neck.html.

36) Guarracino, F., Ferro, B., Forfori, F., Bertini, P., Magliacano, L. and Pinsky, M. R. (2014) 'Jugular vein distensibility predicts fluid responsiveness in septic patients', *Critical Care*. BioMed Central, 18(6), p. 647.

37) Harmon, J. V and Edwards, W. D. (1987) 'Venous valves in subclavian and internal jugular veins. Frequency, position, and structure in 100 autopsy cases.', *The American journal of cardiovascular pathology*, 1(1), pp. 51–4.

38) Hofmann, F. (2003) 'Fundamental principles of Electromagnetic Flow Measurement 3rd Edition'.

39) Hofmann, F. (2011) 'Principles of Electromagnetic Flow Measurement'.

40) Holdsworth, D. W., Rickey, D. W., Drangova, M., Miller, D. J. M. and Fenster, A. (1991) 'Computer-controlled positive displacement pump for physiological flow simulation', *Medical & Biological Engineering & Computing*. Kluwer Academic Publishers, 29(6), pp. 565–570.

41) Hollinshead, W. H. (William H. (1982) *The Head and neck*. Harper & Row.

42) Holmlund, P., Johansson, E., Qvarlander, S., Wåhlin, A., Ambarki, K., Koskinen, L. D., Malm, J. and Eklund, A. (2017) 'Human jugular vein collapse in the upright

posture: implications for postural intracranial pressure regulation', *Fluids and Barriers of the CNS*, 14.

43) Hoskins, P., Martin, K. and Thrush, A. (2010) *Diagnostic ultrasound : physics and equipment*. Cambridge University Press.

44) Hu, H.-H. and Chung, C.-P. (2008) 'Jugular Venous Reflux Cerebral Venous System (CVS)', *Journal of Medical Ultrasound*, 16(33), pp. 210–222.

45) Imai, M., Hanaoka, Y. and Kemmotsu, O. (1994) 'Valve injury: a new complication of internal jugular vein cannulation.', *Anesthesia and analgesia*, 78(6), pp. 1041–6.

46) J.C. Lacefield (2014) 'A Handbook for Teachers and Students:Chapter 13: Ultrasound Imaging:Diagnostic Radiology Physics':, (IAEA).

47) Jeff McLaughlin (2016) *Anatomy and physiology: 20.2 Blood Flow, Blood Pressure, and Resistance | Anatomy and Physiology*.

48) John (2011) *Electrical Pressure Transducers-Types,Working,Construction,Sensors*.

49) Kalmanson, D., Veyrat, C., Derai, C., Savier, C. H., Berkman, M. and Chiche, P. (1972) 'Non-invasive technique for diagnosing atrial septal defect and assessing shunt volume using directional Doppler ultrasound. Correlations with phasic flow velocity patterns of the shunt.', *British heart journal*. BMJ Publishing Group, 34(10), pp. 981–91.

50) Katz, A. I., Chen, Y. and Moreno, A. H. (1969) 'FLOW THROUGH A COLLAPSIBLE TUBE EXPERIMENTAL ANALYSIS AND MATHEMATICAL MODEL', *Biophysical Journal*, 9, pp. 1261–1279.

51) Kelly A. Young,Long Beach, D. H. K. (2013) *Blood Flow, Blood Pressure, and Resistance | Anatomy and Physiology II*. Available at: https://courses.lumenlearning.com/ap2/chapter/blood-flow-blood-pressure-and-resistance-no-content/.

52) Kemp, C. D. and Conte, J. V. (2012) 'The pathophysiology of heart failure', *Cardiovascular Pathology*. Elsevier, 21(5), pp. 365–371.

53) Kishore Pichamuthu (2009) *Tutorial 2 - Modes of Ultrasound | ICU Sonography*.

54) Kokalari, I., Karaja, T. and Guerrisi, M. (2013) 'Review on lumped parameter method for modeling the blood flow in systemic arteries', *J. Biomedical Science and Engineering*, 6, pp. 92–99.

55) Laganà, M. M., Pelizzari, L., Scaccianoce, E., Dipasquale, O., Ricci, C., Baglio, F., Cecconi, P. and Baselli, G. (2016) 'Assessment of Internal Jugular Vein Size in Healthy Subjects with Magnetic Resonance and Semiautomatic Processing', *Behavioural Neurology*, 2016, pp. 1–7.

56) Lorchirachoonkul, T., Ti Prof., L. K., Manohara, S., Lye, S. T., Tan, S. A., Shen, L. and Kang, D. S. C. (2012) 'Anatomical variations of the internal jugular vein: Implications for successful cannulation and risk of carotid artery puncture', *Singapore Medical Journal*, 53(5), pp. 325–328.

57) Low, H. T. and Chew, Y. T. (1991) 'Pressure/flow relationships in collapsible tubes: effects of upstream pressure fluctuations', *Medical & Biological Engineering & Computing*. Kluwer Academic Publishers, 29(2), pp. 217–221.

58) Magder, S. (2016) 'Volume and its relationship to cardiac output and venous return', *Critical Care*. BioMed Central, 20(1), p. 271.

59) Mahan, A. F., McEvoy, M. D. and Gravenstein, N. (2016) 'Long-axis view for ultrasound-guided central venous catheter placement via the internal jugular vein.', *Romanian journal of anaesthesia and intensive care*. Romanian Society of Anaesthesia and Intensive Care, 23(1), pp. 27–31.

60) Malferrari, G., Prati, P. and Zedde, M. (2014) 'Neurosonological evaluation of cerebral venous outflow : an ultrasound atlas:Ultrasound Anatomy and How to do the Examination', p. 138.

61) Maria Helguera (2008) *An Introduction to Ultrasound*.

62) Mark Hammer (2014) *US Physics: Pulsed-Wave Doppler Simulation - XRayPhysics*.

63) Menegatti, E., Tessari, M., Gianesini, S., Vannini, M. E., Sisini, F. and Zamboni, P. (2014) 'Human internal jugular valve M-mode ultrasound characterization.', *Current neurovascular research*. Bentham Science Publishers, 11(2), pp. 149–55.

64) Menegatti, E., Tessari, M., Vannini, M. E., Gianesini, S., Malagoni, A. M., Ciorba, A., Mazzoli, M., Sisini, F., Salvi, F., Pelucchi, S. and Zamboni, P. (2017) 'High Resolution M-Mode Evaluation of Jugular Vein Valves in Patients with Neurological and Neurosensory Disorders.', *Curr Neurovasc Res*, 14(4), pp. 316–322.

65) Miki, I., Murata, S., Nakazawa, K., Onozawa, S., Mine, T., Ueda, T., Yamaguchi, H., Yasui, D., Takeda, M. and Kumita, S. (2014) 'Anatomical relationship between the common carotid artery and the internal jugular vein during head rotation.', *Ultrasound (Leeds, England)*. SAGE Publications, 22(2), pp. 99–103.

66) Miryam M.Reems, DVM, DACVECC Marcel Aumann, Med.Vet., DACVECC, D. (2012) 'Central Venous Pressure: Principles, Measurement, and Interpretation', *compendium*, 34,1.

67) Mitchell, D. G. (1990) 'Color Doppler imaging: principles, limitations, and artifacts.', *Radiology*, 177(1), pp. 1–10.

68) Moorthy, R. S. (2002) 'DOPPLER ULTRASOUND.', *Medical journal, Armed*

Forces India. Elsevier, 58(1), pp. 1–2.

69) Morimoto, A., Takase, I., Shimizu, Y. and Nishi, K. (2009) 'Assessment of cervical venous blood flow and the craniocervical venus valve using ultrasound sonography', *Legal Medicine*. Elsevier, 11(1), pp. 10–17.

70) Moss, R. L. and Fitzsimons, D. P. (2002) 'Frank-Starling Relationship', *Circulation Research*, 90(1).

71) Narouze, S. N. (2011) 'Atlas of ultrasound-guided procedures in interventional pain management', *Atlas of Ultrasound-Guided Procedures in Interventional Pain Management*, pp. 1–372.

72) Nedelmann, M., Eicke, B. M. and Dieterich, M. (2005) 'Functional and Morphological Criteria of Internal Jugular Valve Insufficiency as Assessed by Ultrasound', *Journal of Neuroimaging*. Blackwell Publishing Ltd, 15(1), pp. 70–75.

73) Nilsson, J. W. and Riedel, S. A. (1996) *Electric circuits.* Addison-Wesley.

74) Oliver Jones (2017) *Venous Drainage of the Head and Neck - Dural Sinuses - TeachMeAnatomy*, *Revisions: 38*.

75) Oyama, M. A. (2015) 'Mechanisms of Heart Failure', in *Small Animal Critical Care Medicine*. Elsevier, pp. 205–209.

76) Paul Peter Urone, R. H. (2012) *Viscosity and Laminar Flow; Poiseuille's Law · Physics*.

77) Quick, C. M., Berger, D. S. and Noordergraaf, A. (1998) 'modeling in physiology Apparent arterial compliance'.

78) Ramnarine, K. V, Hoskins, P. R., Routh, H. F. and Davidson, F. (1999) 'Doppler backscatter properties of a blood-mimicking fluid for Doppler performance assessment', *Ultrasound in Medicine & Biology*. Elsevier, 25(1), pp. 105–110.

79) Ramnarine, K. V, Nassiri, D. K., Hoskins, P. R. and Lubbers, J. (1998) 'Validation of a New Blood-Mimicking Fluid for Use in Doppler Flow Test Objects', *Ultrasound in Medicine & Biology*. Elsevier, 24(3), pp. 451–459.

80) Ratanakorn, D., Tesh, P. E. and Tegeler, C. H. (1999) 'A New Dynamic Method for Detection of Internal Jugular Valve Incompetence Using Air Contrast Ultrasonography', *Journal of Neuroimaging*, 9(1), pp. 10–14.

81) Reems, M. M. and Aumann, M. (2012) 'Central venous pressure: principles, measurement, and interpretation.', *Compendium (Yardley, PA)*, 34(1), pp. E1–E10.

82) Richard E. Klabunde (2012) *CV Physiology | Factors Promoting Venous Return*.

83) Richard E. Klabunde, P. (2013) *CV Physiology | Venous Return - Hemodynamics*.

84) Robbins, M. F. (2017) *Resistance and Ohm's Law - "Ultimate*

Electronics" Book - CircuitLab.

85) Roger, ©prof and Mark, G. (2004) 'CARDIOVASCULAR MECHANICS I, II, III:. Models of the Peripheral Circulation', pp. 101–115.

86) Sanchez-Hanke, M., Püschel, K. and Leuwer, R. (2000) 'On the anatomy of the venous valves of the internal jugular vein', *Laryngo-Rhino-Otologie*, 79(6), pp. 332–336.

87) Schollenberger, J., Figueroa, A. C. and Pfaller, M. (2015) *A lumped parameter model of cerebral blood flow regulation: Applications to simulation of carotid endarterectomy*.

88) Shinn-Kuang Lin1 (2009) 'Hemodynamics of the Internal Jugular Vein: An Ultrasonographic Study', *Tzu Chi Medical Journal*, 21.

89) Simka, M. (2014) 'Chronic cerebrospinal venous insufficiency: current perspectives', *Journal of Vascular Diagnostics*. Dove Press, 2, p. 1.

90) Simka, M., Ludyga, T., Latacz, P. and Kazibudzki, M. (2013) 'Diagnostic accuracy of current sonographic criteria for the detection of outflow abnormalities in the internal jugular veins', *Phlebology: The Journal of Venous Disease*. SAGE PublicationsSage UK: London, England, 28(6), pp. 285–292.

91) Sisini, F. (2016) 'Physical description of the blood flow from the internal jugular vein to the right atrium of the heart: new ultrasound application perspectives'.

92) Sisini, F., Tessari, M., Menegatti, E., Vannini, M. E., Gianesini, S., Tavoni, V., Gadda, G., Gambaccini, M., Taibi, A. and Zamboni, P. (2016) 'Clinical Applicability of Assessment of Jugular Flow over the Individual Cardiac Cycle Compared with Current Ultrasound Methodology', *Ultrasound in Medicine & Biology*. Elsevier, 42(8), pp. 1750–1763.

93) Sisini, F., Toro, E., Gambaccini, M. and Zamboni, P. (2015) 'The Oscillating Component of the Internal Jugular Vein Flow: The Overlooked Element of Cerebral Circulation', *Behavioural Neurology*, 2015, pp. 1–9.

94) Stolz, E. (2012) 'Ultrasound examination techniques of extra- and intracranial veins', *Perspectives in Medicine*. Elsevier, 1(1–12), pp. 366–370.

95) Tain, R.-W., Ertl-Wagner, B. and Alperin, N. (2009) 'Influence of the compliance of the neck arteries and veins on the measurement of intracranial volume change by phase-contrast MRI.', *Journal of magnetic resonance imaging : JMRI*, 30(4), pp. 878–83.

96) Thorne, M. L., Poepping, T. L., Rankin, R. N., Steinman, D. A. and Holdsworth, D. W. (2008) 'Use of an Ultrasound Blood-Mimicking Fluid for Doppler Investigations

of Turbulence In Vitro', *Ultrasound in Medicine & Biology*, 34(7), pp. 1163–1173.

97) Ursino, M. and Lodi, C. A. (1997) 'A simple mathematical model of the interaction between intracranial pressure and cerebral hemodynamics', *J. Appl. Physiol.* , 82, pp. 1256–1269.

98) Valecchi, D., Bacci, D., Gulisano, M., Sgambati, E., Sibilio, M., Lipomas, M. and Macchi, C. (2010) 'Internal jugular vein valves: an assessment of prevalence, morphology and competence by color Doppler echography in 240 healthy subjects.', *Italian journal of anatomy and embryology = Archivio italiano di anatomia ed embriologia*, 115(3), pp. 185–9.

99) Westerhof, N., Lankhaar, J.-W. and Westerhof, B. E. (2009) 'The arterial Windkessel', *Medical & Biological Engineering & Computing*. Springer-Verlag, 47(2), pp. 131–141.

100) Weyland, A. and Grüne, F. (2009) 'Cardiac preload and central venous pressure', *Der Anaesthesist*, 58(5), pp. 506–512.

101) Wilhjelm, J. E., Illum, A., Kristensson, M. and Andersen, O. T. (2016) 'Medical diagnostic ultrasound -physical principles and imaging'.

102) Yan, W. and Seow, S. (2009) 'Reversed internal jugular vein flow as a sign of brachiocephalic vein obstruction.', *Australasian journal of ultrasound in medicine*. Australasian Society for Ultrasound in Medicine, 12(2), pp. 39–41.

103) Zamboni, P. (2016) 'Why Current Doppler Ultrasound Methodology Is Inaccurate in Assessing Cerebral Venous Return: The Alternative of the Ultrasonic Jugular Venous Pulse', *Behavioural Neurology*, 2016, pp. 1–7.

104) Zamboni, P., Morovic, S., Menegatti, E., Viselner, G. and Nicolaides, A. N. (2011) 'Screening for chronic cerebrospinal venous insufficiency (CCSVI) using ultrasound--recommendations for a protocol.', *International angiology : a journal of the International Union of Angiology*, 30(6), pp. 571–97.

105) Zamboni, P., Tisato, V., Menegatti, E., Mascoli, F., Gianesini, S., Salvi, F. and Secchiero, P. (2015) 'Ultrastructure of internal jugular vein defective valves.', *Phlebology*. SAGE Publications, 30(9), pp. 644–7.

106) Zavoreo, I., Bašić-Kes, V., Zadro-Matovina, L., Lisak, M., Ćorić, L., Cvjetičanin, T., Ciliga, D. and Bobić, T. T. (2013) 'Cerebral venous circulatory system evaluation by ultrasonography', *Acta Clinica Croatica*, 52(2), pp. 203–211.